DISSERTATION

submitted to the

Combined Faculties for the Natural Sciences and for Mathematics

of the Ruperto-Carola University of Heidelberg, Germany,

for the degree of

Doctor of Natural Sciences

Put forward by

Diplom-Physikerin Isabelle Steinke

born in Düsseldorf

Oral examination: 4.12.2013

Ice nucleation properties of mineral dusts

Referees: Prof. Dr. Thomas Leisner

Prof. Dr. Ulrich Platt

Zusammenfassung

Die Eisbildung in Wolken hat einen großen Einfluss auf den Wasserkreislauf und das globale Strahlungsbudget. In der AIDA-Wolkenkammer wurden die Eisnukleationseigenschaften verschiedener, atmosphärisch relevanter Mineralstäube sowohl für den Immersions- als auch den Depositionsnukleationsmodus untersucht. Experimente mit einem standardisierten Staub (Arizona Test Dust) dienten als Grundlage für eine sättigungs- und temperaturabhängige Parametrisierung zur Beschreibung der Depositionsnukleation bei Temperaturen oberhalb von 220 K. Dieser Ansatz wurde auch zur Beschreibung der Depositionsnukleationseigenschaften weiterer Mineralstäube verwendet. Die beobachtete Zeitabhängigkeit der Eisbildung war nur bei sehr kleinen Kühlraten relevant.

Experimente mit atmosphärisch relevanten Stäuben ergaben große Unterschiede in den beobachteten Eisbildungseffizienzen. Vulkanaschepartikel vom Eyjafjallajökull waren weniger eisaktiv als Wüstenstaubpartikel. Hingegen waren fossile Diatome und Bodenproben von landwirtschaftlich genutzten Flächen sehr viel effizientere Eisnukleatoren als Stäube aus Wüstenregionen. Die hohe Eisnukleationseffizienz, die bei den agrarisch geprägten Stäuben beobachtet wurde, ist vermutlich auf organische Komponenten zurückzuführen, jedoch nicht primär auf lebende Organismen wie Pilze oder Bakterien.

Der Einfluss von Beschichtungen auf die Eisnukleationseigenschaften von Mineralstäuben wurde für sekundär-organische Substanzen und Schwefelsäure untersucht. Sekundär-organische Komponenten führten zu einer Unterdrückung der Eisbildung, während für Schwefelsäure dieser Effekt nur im Depositionsnukleationsmodus beobachtet wurde.

Das Immersionsgefrieren von Wassertropfen auf definierten Oberflächen wurde für Silizium und Muskovit als Mineralstaubsubstitut untersucht. Muskovit initiierte das Gefrieren von Wassertropfen bereits bei Temperaturen um 250 K, war jedoch ein wesentlich ineffizienterer Eisnukleator als natürliche Wüstenstäube. Tropfen, die auf einer Siliziumoberfläche platziert worden waren, gefroren im Bereich der Temperaturschwelle des homogenen Gefrierens von Wolkentropfen. Durch das Erzeugen künstlicher Strukturen auf Siliziumoberflächen ließen sich die Gefriereigenschaften dieses Materials signifikant verändern, so dass die Oberflächenmorphologie als ein Faktor identifiziert werden konnte, der die Eisnukleationseffizienz von Aerosolpartikeln beeinflusst.

Abstract

Ice nucleation in clouds has a significant impact on the global hydrological cycle as well as on the radiative budget of the Earth. The AIDA cloud chamber was used to investigate the ice nucleation efficiency of various atmospherically relevant mineral dusts.

From experiments with Arizona Test Dust (ATD) a humidity and temperature dependent ice nucleation active surface site density parameterization was developed to describe deposition nucleation at temperatures above 220 K. Based on these results, a parameterization for deposition nucleation initiated by desert dusts and clay minerals is proposed. The time dependence observed during the deposition nucleation experiments with ATD seems to be relevant only at very small cooling rates. Experiments with atmospherically relevant dust samples revealed large differences in the ice nucleation efficiencies among the different dusts. Volcanic ash emitted during the Eyjafjallajökull eruption in 2010 proved to be slightly less ice-active than mineral dust particles from desert areas. In contrast, soil dust particles rich in organic matter and fossile diatomite were very ice-active particles. For the soil dust particles, the soil organic matter is probably the reason for the enhanced ice nucleation efficiency compared to desert dusts which is, however, most likely not directly determined by viable organisms such as fungi or bacteria.

Coatings with secondary organic compounds led to a significant deterioration of the ice nucleation efficiency observed for fossile diatomite in the immersion freezing and the deposition nucleation mode. Deposition mode nucleation initiated by mineral dust particles was suppressed by coatings with sulfuric acid whereas there was no effect on the immersion freezing properties.

The immersion freezing properties of several substrates used as ice nuclei substitutes were investigated with a cold stage setup. Muscovite initiated heterogeneous ice nucleation at approximately 250 K but was much less ice-active than mineral dusts. Droplets placed on silicon wafers froze only close to the homogeneous freezing threshold. The freezing properties of these silicon wafers could be changed significantly by modifying the wafer surface through adding regular structures such as trenches which suggests that the surface morphology may have an influence on the ice nucleation efficiencies of atmospheric particles.

Contents

Chapter 1

Introduction

Aerosol particles such as sea salt or mineral dust are suspended in the layers of the lower and upper troposphere and have a significant influence on atmospheric processes, and thus on global climate (Pruppacher and Klett, 1997). Furthermore, they also influence biogeochemical processes in the ocean and interact with the biosphere (Pöschl, 2005; Seinfeld and Pandis, 2006; Mahowald et al., 2011).
Aerosol induced climate effects are mitigated through the interaction between aerosol particles and the incoming solar radiation as well as through aerosols influencing clouds. During the last decades, aerosol-cloud-interaction processes and different sources of atmospheric aerosols have received increasing interest from the atmospheric sciences community. The importance of gaining a better understanding of how aerosol particles may impact global climate was especially highlighted by the 4th assessment report of the IPCC issued in 2007 (Forster et al., 2007).

In the next section, sources of the most abundant aerosols are described, followed by a brief discussion of the pathways of interaction between aerosols and clouds with a focus on the ice nucleation in clouds initiated by mineral dust particles and clay minerals. The last part of this chapter is dedicated to an outline of the goals that were pursued within this thesis project.

1.1 Atmospheric aerosol

Different sources contribute to the atmospheric aerosol loading which consists of liquid and solid particles. Solid aerosol particles are emitted from land sources as well as from the oceans (Pöschl, 2005; Seinfeld and Pandis, 2006; Mahowald et al., 2011). Aerosol emissions are characterized by a considerably high spatial and temporal variability. Model simulations suggest than mineral dust and soot particles are the most numerous aerosol species in the atmosphere (Hoose et al., 2010). In terms of mass, natural aerosols such as mineral dust and sea salt make up most of the aerosol population. Sulfates are also very prevalent in the atmosphere and often interact with other chemical precursors or solid aerosol particles.

Among the natural aerosols there are several groups which can be distinguished:

- **Sea spray**: Droplets that are released from the ocean surface by production of jets, film drops and spume (Grini et al., 2002) contain mainly sodium chloride and various bromines. Upon drying, these droplets form solid aerosol particles consisting of complex mixtures between organic and inorganic compounds. Sea spray particles can also contain remnants from oceanic biological activity such as marine diatoms. Emissions estimates for the fine fraction of sea salt (particles with diameters smaller than 0.5 µm) range from 24 to 471 Tg yr^{-1}, whereas the emissions of coarse particles are estimated as 1916 – 12210 Tg yr^{-1} (Tsigaridis et al., 2013). Note that the estimated source emissions are highly uncertain due to the varying contributions of different sea spray production mechanisms and the heterogeneity of the source regions (de Leeuw et al., 2011).

- **Mineral dust**: Another very important source for atmospheric aerosol particles are arid regions such as the Sahara Desert where dry conditions meet exposed soil surfaces. Above certain wind speed thresholds, saltation processes initiated by large soil particles can induce a substantial vertical flow of particles smaller than 10 µm. Main desert dust source areas are located in Africa and Asia, whereas the contribution to atmospheric mineral dust from Northern American arid regions

and the Southern Hemisphere is assumed to be almost negligible on the global scale (Ginoux et al., 2012). Mineral dust particles emitted from dry regions mainly consist of a variety of minerals such as illite or quartz (Broadley et al., 2012). In contrast, soil dust particles emitted from agricultural areas may contain various components of organic origin (Conen et al., 2011). Other sources of mineral dust particles are volcanoes which sporadically release volcanic silicate particles into the atmosphere (Durant et al., 2010). The emission flux estimates for mineral dusts range from 500 to 4300 Tg yr^{-1} (Tegen and Schepanski, 2009; Huneeus et al., 2011).

- **Biological particles**: Aerosol emissions from biological sources are not very well characterized because of the vast number of species which can contribute to the emission flux, such as bacteria, pollen, lichen, fungi and plant debris. Additionally, the complex interactions within the biosphere itself as well as with the other compartments, i.e. the hydrosphere and the atmosphere, lead to a high uncertainty of estimated emission fluxes. Estimates for the emission flux from biological sources are highly variable and deliver values from less than 10 to 1000 Tg yr^{-1} (Després et al., 2012).

In contrast to primary aerosol particles, secondary aerosol particles can form from nucleation or condensation of gaseous precursors such as sulfuric acid vapor or terpenes (Pöschl, 2005).
It should be noted, however, that the total atmospheric aerosol burden not only on the emission strengths of the individual sources but also on the meteorological conditions.

1.2 Influence of aerosols on global climate: direct and indirect effect

Aerosols have a significant influence on the global climate in several ways. First, aerosols directly and indirectly influence the radiation budget of the Earth and the hydrological cycle. Secondly, aerosol particles also influence chemical processes in the atmosphere. The chemical processes are in turn intertwined with physical processes such as the water

uptake by aerosols or the freezing properties of atmospheric particles. In the following paragraphs, direct and indirect aerosol effects are discussed in greater detail.

Through scattering and absorption of incoming sun light and terrestrial radiation, aerosols can influence the radiation budget (direct effect) (Forster et al., 2007). The radiative properties with regard to scattering and absorption are largely controlled by the particle size, the aerosol composition and the particle shape (Seinfeld and Pandis, 2006). Note that during atmospheric transport, aerosol particles undergo changes in size, structure and composition which also impact their radiative properties (Pöschl, 2005).

Additionally, aerosol particles may impact global climate by influencing cloud characteristics (indirect effect) (Lohmann and Feichter, 2005). Mid-tropospheric clouds alone cover more than 25% of the Earth's surface and therefore act as a determinant of global climate (Sassen and Wang, 2012). Aerosol particles influence the structure and dynamics of liquid water, mixed-phase and cirrus clouds because they can act as cloud condensation nuclei (CCN) or as ice nuclei (IN) (Pruppacher and Klett, 1997).
Depending on their chemical composition and surface morphology, aerosols can take up water and activate to cloud droplets. The CCN concentration also influences the cloud droplet sizes because within highly polluted clouds, droplets are more numerous and hence smaller for a fixed liquid water content (Bréon et al., 2002). Smaller droplets experience gravitational sedimentation to a lesser degree than large droplets which causes collisions and coalescence between droplets to become less frequent. Consequently, the number of precipitation sized droplets is decreased and thus precipitation itself is suppressed. If this effect is significant, cloud lifetime is prolonged (Albrecht, 1989).
In mixed-phase clouds, the ice phase can be a very important driver of precipitation. Ice formation in mixed-phase clouds also influences cloud lifetime because ice crystals grow at the expense of supercooled droplets (Bergeron-Findeisen process) (Pruppacher and Klett, 1997). The release of latent heat during freezing can also change the convective structure of a cloud (Lohmann and Feichter, 2005). Generally, pure water droplets in clouds freeze by homogeneous nucleation only at temperatures below 235 K (Pruppacher and Klett, 1997). Homogeneous ice nucleation above this temperature threshold is prohibited by an

energy barrier separating the metastable liquid phase from the more stable crystalline ice phase.
An insoluble aerosol particle can act as ice nucleus (IN) reducing the energy needed for forming a critical ice cluster which can then grow into an ice crystal (heterogeneous ice nucleation) (Vali, 1985). Ice formation is assumed to occur at "active sites" which possess characteristics differentiating them from the rest of the particle surface (Fletcher, 1969; Pruppacher and Klett, 1997).

There are several different ice nucleation pathways, namely immersion/condensation freezing, deposition nucleation and contact freezing (Vali, 1985). Immersion freezing requires that an aerosol particle is enclosed within a droplet before the freezing event occurs, whereas for condensation freezing water condenses on the aerosol particle's surface before freezing then occurs at the same temperature. For deposition nucleation, water vapor is directly transformed into ice at the particle's surface. Contact freezing requires the presence of supercooled droplets and dry aerosol particles which collide with the droplets to initiate freezing.
The ice nucleation properties of different aerosol species depend on their physico-chemical surface properties and the particle size.

1.3 Ice nucleation properties of dust particles

Field measurements revealed that many ice crystals contain dust particles or clay minerals, in some cases mixed with biological components (Kumai, 1961; DeMott et al., 2003; Pratt et al., 2009). Atmospheric mineral dust mainly consists of clay minerals, quartz and feldspar minerals with illite being the most abundant mineral component in the atmosphere (Broadley et al., 2012; Murray et al., 2012). The impact of mineral dust particles on cloud microphysical processes such as droplet activation and ice nucleation largely depends on the origin of the dust (i.e. the chemical composition) and the ageing that dust particles may experience during atmospheric transport (Pruppacher and Klett, 1997; Pöschl, 2005). For example, dust particles from the Sahara Desert and close to this particular source region are less probable to activate to cloud droplets than dust particles

transported through polluted areas (Smoydzin et al., 2012).

Modelling studies show that mineral dust particles have an especially large impact on clouds whenever the meteorological conditions are favorable for heterogeneous ice nucleation and dust may dominate ice formation in mixed-phase clouds (Hoose et al., 2010). Dust particles may initiate ice formation already at temperatures below 263 K according to satellite observations (Zhang et al., 2012). Ice crystals in turn influence the radiative properties of clouds and thus - under certain meteorological conditions - dust induced freezing in mixed-phase clouds can be associated with cooling at the Earth's surface (e.g., Bangert et al. (2012)). However, there are still many open questions regarding the mechanisms of atmospheric ice formation and the ice nucleation properties of different mineral dusts and clay minerals.

The ice nucleation properties of natural mineral dusts and clay minerals such as illite have been investigated with laboratory studies since several decades (see references in the review by Hoose and Möhler (2012)). Arizona Test Dust (ATD) which is a commercially available dust has been used as a standard dust to be compared with natural dust samples and as a reference for intercomparisons between different experimental setups (e.g., Koehler et al. (2010)).
For some experimental studies, the ice nucleation properties of mineral dusts were characterized by the temperature threshold at which freezing was first observed. Several mineral dust samples were observed to initiate freezing at temperatures between 242 and 267 K, depending on the particle sizes (not characterized) and their geological origin which is strongly related to their physico-chemical characteristics (Isono and Ikebe (1960) and references therein; Vali (2008)). Note that these samples were collected from various sources, such as volcanic eruptions, soils or glaciers. Fossil diatoms which, like mineral dust particles, mainly consist of alumina silicates were observed to initiate ice nucleation at 260 K (Pruppacher and Sänger, 1955).

Freezing thresholds, however, were recognized to strongly depend on particle size and thus the sample preparation in different experimental studies (Hoose and Möhler, 2012).

Therefore, the relation between aerosol surface area and observed ice fractions is now often used to express ice nucleation efficiencies of different aerosol types by the so-called ice nucleation active surface site (INAS) density which will be explained in more detail in the next chapter. For deriving the INAS densities, the observed ice crystal concentrations are normalized by the total aerosol surface area. Using the INAS density as a measure for the observed ice nucleation efficiency allows for comparisons among different aerosol types and also between different experimental setups.

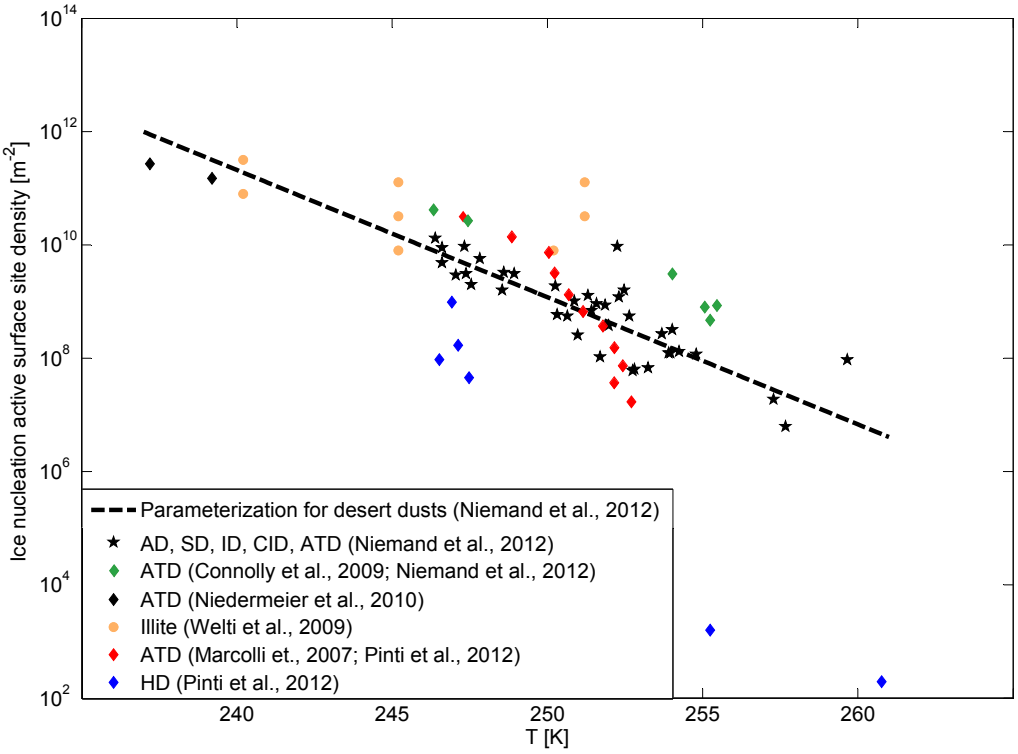

Figure 1.1: *Ice nucleation active surface site densities for immersion freezing initiated by various desert dusts (SD: Saharan Dust, ID: Israel Dust, CID: Canary Island Dust, AD: Asian Dust, HD: Hoggar Dust) and illite*

For immersion freezing, extensive investigations of the ice nucleation efficiencies of mineral dusts and clay minerals have been conducted. The INAS densities for selected ice nucleation experiments with desert dusts and one clay mineral (illite) are depicted in Fig. 1.1. Note that these values are derived from different ice nucleation counters which

might partly contribute to differences between the observed ice nucleation efficiencies.

The ice nucleation efficiencies of various desert dusts as derived from AIDA cloud chamber experiments are remarkably similar and can therefore be parameterized by an exponential function (Niemand et al., 2012). This parameterization includes AIDA cloud chamber (Karlsruhe, Germany) experiments with natural dusts from source regions such as Israel, the Canaries, Asia and Northern Africa. Despite differences in the mineralogy and the associated physico-chemical properties these dusts vary only by one order of magnitude with regard to their INAS density.

The INAS densities for ATD derived from AIDA cloud chamber measurements agree well within the measurement uncertainties (Connolly et al., 2009; Niemand et al., 2012). On average, ATD is slightly more ice-active than natural desert dusts. For comparison, the INAS densities measured by the ice nucleation counter LACIS (Leipzig, Germany) for ATD are depicted (Niedermeier et al., 2010). These values are slightly lower than INAS densities derived from AIDA cloud chamber experiments which might be explained by differences in the INAS densities averaged over a polydisperse aerosol population and the ice nucleation efficiency observed for size selected particles as used in the LACIS experiments. Marcolli et al. (2007) investigated the immersion freezing properties of ATD suspensions. Note that suspending dust in water might lead to a re-distribution of soluble material on the dust particles and thus to a change in the ice nucleation efficiency. For temperatures below 250 K, a good agreement with the AIDA cloud chamber experiments can be observed whereas at higher temperatures the INAS densities for ATD are lower (Marcolli et al., 2007; Pinti et al., 2012).

The large variation in ice nucleation efficiencies observed for the Hoggar Dust sample is interpreted as at least two different types of ice nucleating sites of which the most active sites are, however, very rare (Pinti et al., 2012). Freezing at 260 K initiated by Hoggar dust is observed for experiments with large droplets (in the millimeter size range) with a large number of potentially ice nucleating particles whereas freezing of small (micrometer sized) droplets only occured at temperatures below 247 K (Pinti et al., 2012). The freezing events observed at 260 K can be interpreted as a freezing threshold.

Note that the measurements presented in Pinti et al. (2012) are not directly comparable to the results from cloud chamber experiments because the aerosol surface within the

droplets was determined from BET measurements.
Complementing the ice nucleation experiments with desert dusts which consist of several different minerals, the ice nucleation active surface site densities for illite are shown in Fig. 1.1. The temperature dependence of the ice nucleation efficiency measured for illite is not as strong as for the desert dusts, but in general illite is similarly efficient than the natural dusts (Welti et al., 2009).

From the measurements described in the previous paragraphs it can be concluded that the immersion freezing efficiency observed for dusts and clay minerals is relatively well quantified even though there are still unexplained differences between dust and mineral species. Note that different methods are used to quantify the surface area of ice nucleating particles which leads to INAS densities which cannot be directly compared to each other (Murray et al., 2012). Furthermore, data are sparse above 250 K and additional experiments should be conducted in order to better characterize the ice nucleation efficiencies of mineral dusts and clay minerals (Hoose and Möhler, 2012). This is especially important with regard to estimating the influence of mineral dust particles on mixed-phase clouds at small supercoolings for which biological particles might act concomitantly as very efficient ice nuclei (Möhler et al., 2008b).

For deposition nucleation, there are only a few studies which express the observed ice nucleation efficiencies by ice nucleation active surface site density values (e.g, Wheeler and Bertram (2012)). Also, a suitable metric for quantifying the ice nucleation efficiency in relation to the change in thermodynamic conditions is difficult to construct because deposition nucleation is driven both by supercooling and relative humidity over ice (Pruppacher and Klett, 1997). So far, most experiments investigating the deposition nucleation properties of mineral dusts only considered the humidity dependence but neglected supercooling (e.g., Wheeler and Bertram (2012)). However, with neglecting the temperature dependence, the ice nucleation active surface site densities observed for mineral dusts differ by up to four orders of magnitude (Hoose and Möhler, 2012). Thus, for deposition nucleation more experiments which deliver temperature and humidity dependent ice fractions as well as the aerosol surface area are needed to develop a parameterization

analogous to the immersion freezing parameterization derived by Niemand et al. (2012).

Besides finding suitable measures for quantifying the ice nucleation efficiencies of the various aerosol species, another challenge is presented by the fact that the basic microphysical processes which determine atmospheric ice formation are still not completely understood. However, experiments as well as molecular dynamics simulations try to gain a better understanding of the processes involved in the formation of ice crystals in the presence of aerosol particles (e.g, Cox et al. (2013)).

1.4 Objectives of this thesis

This thesis focusses on investigating the ice nucleation properties of different mineral dusts ranging from pure fossile diatoms to soil dusts with potentially ice-active organic components. Results from ice nucleation experiments conducted at the AIDA (Aerosol Interaction and Dynamics in the Atmosphere) cloud chamber facility are presented. Mixed-phase and cirrus clouds were simulated to learn more about immersion freezing and deposition nucleation initiated by different mineral dusts. Additionally, for some dust samples atmospheric ageing was simulated by letting secondary organic substances or sulfuric acid vapor condense onto the aerosol particles. The impact of atmospheric ageing on the ice nucleation properties of mineral dusts was investigated for diatoms, Saharan dust and Arizona Test Dust.

The contribution of time dependent ice nucleation to the observed ice nucleation efficiencies is discussed using cloud chamber experiments with Arizona Test Dust during which the effect of varying cooling rates and aerosol concentrations was investigated. These experimental studies were used as a basis for model calculations with the Aerosol Cloud and Precipitation Interactions Model (ACPIM, University of Manchester). Also, a parameterization for deposition nucleation initiated by desert dusts is proposed.

The cloud chamber studies are complemented by experimental results from droplet freezing studies with a cold stage setup. With desert dusts exhibiting very complex morpholog-

ical and chemical characteristics, immersion freezing was investigated for monocrystalline materials (silicon, copper and graphite) and muscovite. First results are also presented for droplet freezing experiments investigating silicon wafers with engineered structures mimicking the influence of particle morphology on ice nucleation and suspensions containing feldspar particles.

Chapter 2

Theory

Global circulation models (GCMs) are used to estimate the aerosol-induced radiative forcing which is generated by direct and indirect effects. However, the reliability of these estimates depends on how well the cloud microphysical processes are implemented in the models. Generally, aerosol-cloud-interaction processes such as heterogeneous ice nucleation are described not explicitly but by simplifying model parameterizations because cloud microphysical processes are very complex and depend on many variables. Heterogeneous ice nucleation is a particularly difficult case because the basic microphysical processes which govern the interaction between aerosol particles and water molecule clusters are still not completely unravelled. As a consequence of this lack of fundamental understanding, several ways to quantify the ice nucleation efficiencies of different aerosol species have been explored and tested in the past decades.

The first extensive ice nucleation studies quantified the ice nucleation efficiencies of certain aerosols for each experimental run by the temperature threshold at which the first few aerosol particles initiated the formation of ice, e.g. one particle in twenty-thousands in the study by Isono et al. (1959a). These temperature values are then taken as the ice nucleation thresholds. Ice nucleation thresholds, however, are not only strongly influenced by the chemical composition of the aerosol particles, but also depend on various factors such as the aerosol size distribution. Furthermore, ice nucleation thresholds also depend on the definition of the thermodynamic threshold conditions. Thus, efforts were made

to find more general definitions for the ice nucleation efficiencies which can be applied in other contexts than the one that was prescribed by the individual experimental setup. Several approaches which can be used to describe the ice nucleation efficiencies of complex aerosol populations will be sketched in this section, such as

- nucleation rate formulations based on classical nucleation theory
- the ice nucleation active surface site (INAS) density approach
- parameterizations combining stochastic and singular aspects of ice nucleation, and
- parameterizations derived from field measurements

At the end of this chapter, a short overview of model studies implementing different ice nucleation parameterizations will be presented (e.g., Yun and Penner (2012); Spichtinger and Gierens (2009); Spichtinger and Cziczo (2010); Barahona (2012); Sassen and Benson (2000)). Note that only immersion freezing and deposition nucleation are discussed explicitly because these are the most relevant freezing modes with regard to the experimental results that are presented in this work.

2.1 Classical nucleation theory

Ice nucleation is a process that starts with the clustering of water molecules at temperatures below the triple point temperature of water (Pruppacher and Klett, 1997). The cluster sizes fluctuate stochastically as clusters form and decompose again. The Gibbs free energy controls the average size distribution of the clusters. Only clusters reaching a critical size will not disintegrate but grow into ice crystals.

The Gibbs free energy ΔG is determined by two contributions: first, a term related to energy difference between the configurations of a water molecule in the ice phase and the original phase and, secondly, a term which quantifies the energetic effort that is needed to build an interface between water and ice phase (Pruppacher and Klett, 1997). The energy ΔG^* is then evaluated for a cluster of critical size. Together with the rate of water molecules colliding with and adhering to the critical cluster, ΔG^* defines the nucleation rate which in turn describes the emergence of stable ice crystals. The heterogeneous ice

nucleation rate J_{het} is given by

$$J_{het} = A \cdot \exp\left(-\frac{\Delta G^*_{mod}}{kT}\right) \tag{2.1}$$

where A is a pre-factor depending on the ice nucleation mode, k is the Boltzmann constant and T the temperature in [K]. J_{het} is given in [$m^{-2}s^{-1}$].
Conceptually, the Gibbs free energy ΔG^*_{mod} is defined similarly for immersion freezing and deposition nucleation (Chen et al., 2008)

$$\Delta G^*_{mod} = f(\theta) \cdot \Delta G^* = f(\theta) \cdot \frac{16\pi v_w^2 \sigma_{mod}^3}{3\,(kT \cdot ln(S_{mod}))^2} \ \text{[J]} \tag{2.2}$$

with

- $f(\theta)$ being a form factor with $f(\theta) = 0.25 \cdot (2 + \cos\theta)(1 - \cos\theta)^2$ depending on θ which is formally the contact angle between ice embryo and particle surface which is flat compared to the emerging ice clusters,
- v_w is the volume of a water molecule in the ice phase configuration [m^3],
- σ_{mod} refers to the surface tension $\sigma_{i,w}$ at the liquid water/ice interface for immersion freezing and to the surface tension $\sigma_{i,v}$ at the water vapor/ice interface for deposition nucleation given in [J/m^2] (parameterizations decribed in Pruppacher and Klett (1997)),
- and S_{mod} denotes the ratio between the saturation pressures over water and over ice for immersion freezing, whereas for deposition nucleation S_{mod} refers to the saturation ratio with respect to ice (parameterizations given in Murphy and Koop (2005)).

The prefactor A in eq. 2.1 is given by

$$A = A^*_{mod} \cdot n_{1,mod} \cdot Z_{mod} \tag{2.3}$$

where A^*_{mod} [s^{-1}] is the rate at which the ice cluster grow by adsorption of water molecules, $n_{1,mod}$ [m^{-2}] is the number of molecules in contact with the aerosol particle's surface and Z_{mod} is the dimensionless Zeldovich factor representing the disintegration of critical clusters. The factors A^*_{mod}, $n_{1,mod}$ and Z_{mod} are specific to each ice nucleation mode.

They are defined following the approach by Chen et al. (2008).

For immersion freezing, the following relations (Chen et al., 2008) are relevant

$$\begin{aligned} A^*_{imm} &= \frac{kT}{h}\exp\left(-\frac{\Delta G_a}{kT}\right) \\ n_{1,imm} &= 10^{19}\mathrm{m}^{-2} \\ Z_{imm} &= \frac{1}{n_{g,imm}}\cdot\sqrt{\frac{\Delta G^*_{imm}}{3\pi kT}} \end{aligned} \tag{2.4}$$

with ΔG_a being the energy which is necessary to transfer a water molecule from the liquid water phase to its configuration within the newly emerging ice phase and $n_{g,imm}$ the number of water molecules forming an ice germ. The factors mentioned above are defined analogously for deposition nucleation (Chen et al., 2008) with

$$\begin{aligned} A^*_{dep} &= 4\pi r_g^2 \frac{e}{\sqrt{2\pi m_w kT}} \\ n_{1,dep} &= \frac{e}{\nu\sqrt{2\pi m_w kT}}\exp\left(-\frac{\Delta G_d}{kT}\right) \\ Z_{dep} &= \frac{1}{n_{g,dep}}\cdot\sqrt{\frac{\Delta G^*_{dep}}{3\pi kT}} \end{aligned} \tag{2.5}$$

where r_g denotes the size of an ice germ, m_w is the mass of a single water molecule, ΔG_d is the energy needed for desorption of water molecules from the particle's surface, and $n_{g,dep}$ is again the number of water molecules which form a critical cluster. Note that all variables refer to bulk properties of water which are not necessarily equal to the properties of water at the microscopic scale.

For classical nucleation theory, the contact angle θ can be taken as a measure of the ice nucleation efficiency because the form factor $f(\theta)$ represents the aerosol-specific reduction of the energy barrier inhibiting the formation of stable ice germs (Pruppacher and Klett, 1997). From recent experimental studies it was concluded that typically a single contact angle is not sufficient to describe the ice nucleation behaviour of a complex, polydisperse aerosol population (Marcolli et al. (2007); Wheeler and Bertram (2012) and others). Thus, it is generally assumed that a distribution of contact angles is more suitable for representing variations in the ice nucleation efficiencies among particles or even with regard to the surface of a single particle. Commonly, the contact angles are assumed to be lognormally distributed according to their probability of occurence (Lüönd

et al., 2010):

$$p(\theta) = \frac{1}{\sigma_\theta \sqrt{2\pi} \cdot \theta} \exp\left(-\frac{(ln(\theta) - ln(\mu_\theta))^2}{2\sigma_\theta^2}\right) \tag{2.6}$$

with μ_θ being the median contact angle and σ_θ the logarithmic width of the contact angle distribution. Note that using a normal distribution might lead to problems with the normalization as negative contact angles must be excluded.

For each time step Δt with only small changes in temperature T and relative humidity over ice (RH_{ice}), the fraction of aerosol particles having initiated the formation of ice crystals can be calculated with

$$\frac{n_{ice}}{n_0} = 1 - \int_0^\infty \int_0^\pi \exp\left[-4\pi r_N^2 \cdot J_{het} \Delta t\right] \cdot p(\theta) \cdot f(r_N) \, \mathrm{d}\theta \, \mathrm{d}r_N \tag{2.7}$$

where n_{ice} is the number of ice crystals formed during the time period Δt and n_0 being the number of aerosol particles available at the beginning of the time step. $f(r_N)$ refers to the aerosol size distribution.

Application of classical nucleation theory for immersion freezing

In order to illustrate how contact angle distributions are related to observed ice fractions, classical nucleation theory as described in Chen et al. (2008) was applied to contact angle distributions with different median contact angles μ_θ and contact angle distribution widths σ_θ. Figure 2.1 depicts exemplary contact angle distributions with each distribution representing the average ice nucleation properties of a particle population and the corresponding ice fractions predicted from classical nucleation theory.
Different contact angle distributions (eq. 2.6) are intended to represent "very good" ice nuclei (μ_{theta} = 35°, σ_{theta} = 0.10 or σ_{theta} = 0.23))), "good" ice nuclei (μ_{theta} = 40°, σ_{theta} = 0.23) and "dust" ice nuclei (μ_{theta} = 76°, σ_{theta} = 0.23)). The median contact angle of the "dust" ice nuclei corresponds to μ_{theta} = 76° found by Marcolli et al. (2007) for immersion freezing initiated by Arizona Test Dust particles.

The ice fractions were calculated for a monodisperse aerosol population with a particle diameter d = 0.25 µm and a cooling rate r = 2.6 K/min.
The ice fractions are calculated for immersion freezing and rely on the classical nucleation

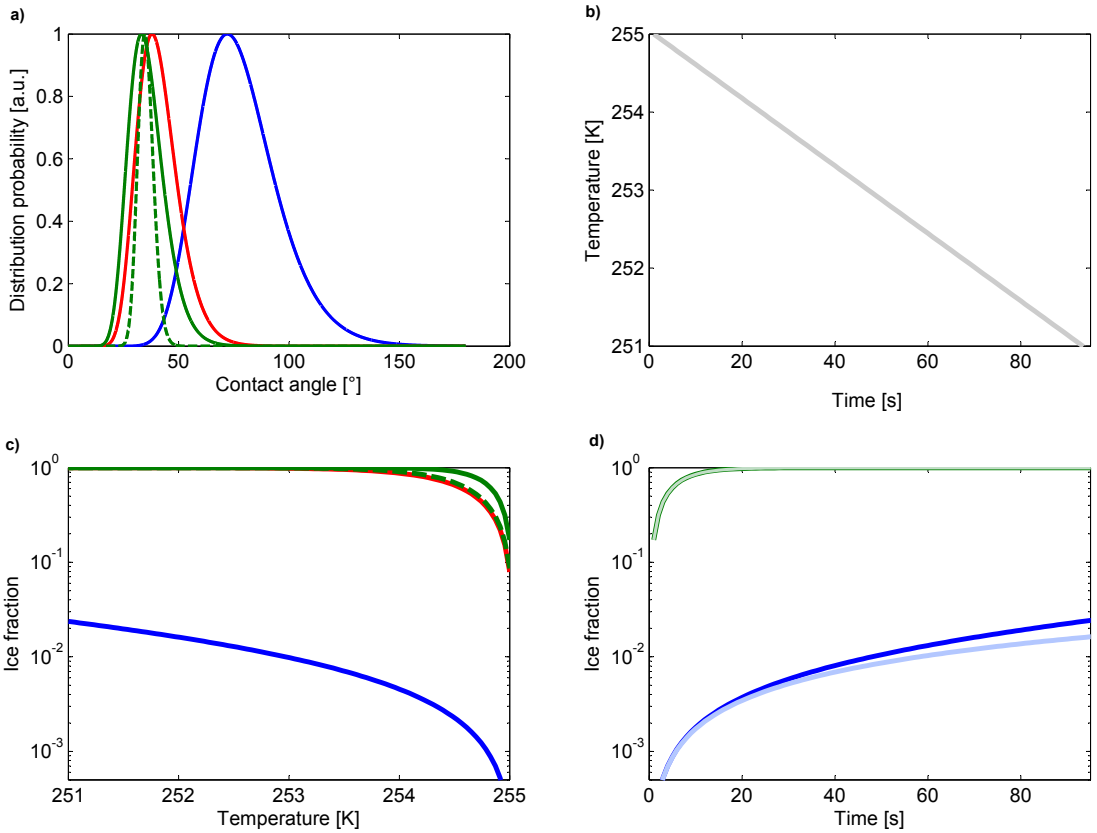

Figure 2.1: *a) Contact angle distributions with different median contact angles and contact angle distribution widths representing "very good" ice nuclei (green), "good" ice nuclei (red) and "dust" ice nuclei (blue)*
b) Prescribed temperature ramp
c) Ice fractions calculated for different contact angle distributions
d) Comparison between ice-active particle fractions for freezing along a cooling ramp (dark green, dark blue) or at constant temperature (light green, light blue)

theory formulations as described in this chapter (following Chen et al. (2008)). Note that for the calculations presented in Fig. 2.1 the Zeldovich factor was set to $Z_{imm} = 1$. The diffusion energy was chosen according to the range of values presented in the study by Chen et al. (2008) with $\Delta G_a = 15 \cdot 10^{-20}$ J. The prescribed temperature ramp starting at 255 K is depicted in Fig. 2.1b whereas the ice fractions are shown in Fig. 2.1c.

All "very good" ice nuclei are activated to ice crystals when the temperature drops below 253 K. The ice fractions observed for the narrow contact angle distribution ($\sigma_{theta} = 0.10$) are initially by a factor of 2 smaller than the ice fractions predicted for the broad contact angle distribution ($\sigma_{theta} = 0.23$). Note that the narrow contact angle distribution includes fewer contributions by very efficient ice nuclei than the broad distribution. Thus, ice fractions for the broad contact angle distribution are expected to be larger.
The "good" ice nuclei are also activated completely below 253 K. The ice fractions are remarkably similar to the results obtained for the "very good" ice nuclei with the narrow distribution. Therefore, for fitting observations with classical nucleation theory formulations it has to be considered that several median contact angles and contact angle distribution widths might lead to an agreement between measured data and calculated freezing curves if the contact angle distributions have a significant overlap. This finding might only be relevant within a certain contact angle distribution range and for certain temperatures but higher uncertainties regarding the fitted parameters might result from these ambiguities.
The simulated "dust" ice nuclei produce ice fractions which are by approximately two orders of magnitude lower than for the "very good" and "good" ice nuclei. The maximum ice fraction which is predicted at 251 K is $f_{ice} = 2.5\%$.

Another feature of freezing described by classical nucleation theory is depicted in Fig. 2.1d which shows a comparison between freezing curves as expected for the cooling ramp (panel b) and a constant temperature $T = 255$ K for the cases considering the "dust" ice nuclei and the "very good" ice nuclei. Freezing occurs even if there is no change in temperature (see eq. 2.7). For the "very good" ice nuclei there is no difference between cooling rate dependent freezing and ice formation at constant temperature. For the "dust" ice nuclei,

the difference between the two cases (cooling rate vs. constant temperature) is less than a factor of 2 between the predicted ice fractions. Thus, in this example the contact angle distribution parameters are more important than the time scale.
In conclusion, nucleation rate formulations based on classical nucleation theory can be used to fit observed freezing curves for aerosols with different ice nucleation efficiencies. However, the range of possible contact angle distribution parameters should be investigated in detail when applying classical nucleation theory. Classical nucleation nucleation theory may also account for the time dependence of freezing which distinguishes this approach from the ice nucleation active surface site density theory which will be described in the next section.

2.2 Ice nucleation active surface site density approach

The ice nucleation active surface site (INAS) density approach is based on the assumption that ice nucleation occurs at characteristic sites at the aerosol particle's surface (Fletcher, 1969). Ice nucleation at these ice active sites is observed to occur seemingly instantaneously if certain temperature (and humidity) thresholds are reached (singular ice nucleation behavior). The INAS approach was motivated by experimental studies finding that the time dependence induced by the inherent stochasticity of ice nucleation was masked by the change in temperature or relative humidity for certain aerosol types and that the observed ice crystal concentration is strongly related to the aerosol surface available for ice nucleation (e.g., Möhler et al. (2006)). A description of immersion freezing similar to the ice nucleation active surface site density concept was already proposed in an experimental study by Vali (1971) where a temperature dependent ice nuclei concentration was derived. Later on, Fletcher (1974) quantified the ice nucleation efficiency of aerosol particles by using a temperature dependent expression for the ice nucleation sites per square centimeter of the particle surface.

Connolly et al. (2009) then investigated the immersion freezing and deposition nucleation

properties of three mineral dust samples and directly related the ice crystal concentration to the measured aerosol surface and the change in temperature. For immersion freezing, the fraction of aerosol particles nucleating ice at a certain temperature is given by the INAS density n_s with

$$\frac{n_{ice}}{n_0} = 1 - \exp(-A_{aer} \cdot n_s(T)) \tag{2.8}$$

where n_{ice} is the number of ice crystals and n_0 the number of particles available for ice nucleation, i.e. particles being immersed in droplets. A_{aer} is the aerosol surface and $n_s(T)$ the temperature dependent INAS density function given in [m^{-2}]. Note that the $n_s(T)$ relation stated in eq. 2.8 implicitly assumes a monodisperse aerosol population. However, the INAS density approach was also used for describing the ice nucleation efficiency of a polydisperse aerosol population (Niemand et al., 2012). The INAS density for polydisperse aerosol can be approximated for small ice fractions ($f_{ice} < 10\%$) by

$$n_s(T) \approx \frac{n_{ice}}{A_{aer}} \ [\mathrm{m}^{-2}] \tag{2.9}$$

with n_{ice} being the ice crystal number concentration (given in [cm^{-3}] for AIDA cloud chamber measurements) and A_{aer} being the total aerosol surface area (given in [μm^2 cm^{-3}] for AIDA cloud chamber experiments). For extending the INAS density approach to deposition nucleation, in addition to the temperature dependence, the dependence of n_s on relative humidity needs to be considered. Note that the actual INAS density can vary among particles of different sizes, i.e. with varying chemical composition and surface morphologies, whereas the INAS density given by eq. 2.9 is a value averaged over the whole aerosol size distribution.

Several experimental studies have found that the INAS density can be used to represent ice nucleation efficiencies of different aerosol types in a consistent way (Hoose and Möhler (2012) and references therein). In the limit of near-zero cooling rates this parameterization predicts that there will be no additional ice crystals forming without a change in temperature. This is partly in contrast to results obtained from classical nucleation theory formulations which predict that ice crystals form even at constant temperature if there are enough efficient ice nuclei (compare Fig. 2.1d).

Also, defining and measuring the surface A_{aer} to which the heterogeneous ice nucleation process is related, has been subject to some debate within the atmospheric sciences

community (Murray et al., 2012). For determining the total aerosol surface area, the aerosol size distribution can be used to estimate the geometric surface (e.g., Connolly et al. (2009); Niemand et al. (2012)). Alternatively, the aerosol surface area can be derived from Brunauer-Emmett-Teller (BET) gas adsorption measurements as employed in the studies by Murray et al. (2011) and by Broadley et al. (2012). The BET surface based on the adsorption of gas molecules includes contributions by small surface irregularities which will be neglected by geometric surface area estimates. The two methods deliver surface areas which differ by probably up to a factor 10 (Murray et al., 2012). Note, however that in climate models only the geometric particle surface area is available.

2.3 Ice nucleation parameterizations with stochastic and singular aspects

A disadvantage of the INAS density approach is the missing description of time-dependent ice nucleation at constant temperature. This deficit has inspired efforts to extend the purely temperature dependent formulations of ice nucleation efficiencies by explicitly representing the time dependence of ice nucleation and thus the cooling rate dependence of the observed ice formation rates. Stochastic temperature fluctuations of ice nucleation events were investigated by letting ensembles of droplets containing aerosol particles experience several freeze/thaw cycles at different cooling rates (Vali and Stansbury, 1965; Vali, 2008). A change in cooling rate is assumed to be reflected in a change in the observed median freezing temperature leading to a cooling rate dependence of eq. 2.9 with

$$n_s(T-\alpha) \approx \frac{n_{ice}}{A_{aer}} \; [\mathrm{m}^{-2}] \tag{2.10}$$

with the temperature shift α (in [K]) given by $\alpha = \beta \cdot ln(|r|)$ where $\beta = 0.66$ is an empirical parameter (Vali and Stansbury, 1965) and r represents the value of the cooling rate [K/min]. Note that other studies have found that β might be larger ($\beta = 2.01$ (Murray et al., 2011)) and thus appears to be not very well constrained by measurements.

A more mechanistic approach was pursued by Niedermeier et al. (2011b). In their study

the so-called soccer ball model was proposed which is based on the assumption that not all ice nucleation sites at the surface of an individual particle show the same ice nucleation efficiency (i.e. contact angle). According to the soccer-ball model, patches with varying contact angles are distributed across the surface of an aerosol particle. The number of active site patches as well as the contact angle distribution can be varied within this parameterization framework. Thus, the full range from nearly singular to fully stochastic ice nucleation behaviour can be reproduced. However, neither the size of the patches nor the contact angle distribution of individual particles are parameters that can be constrained directly by measurements.

2.4 Ice nucleation parameterizations encomprising several aerosol types

The parameterizations that have been discussed in this chapter so far were mainly applied to specific aerosol types, such as certain mineral dusts or bacteria. However, atmospheric measurements often do not explicitly distinguish between different aerosol species. Thus, in several studies combinations of laboratory data and field measurements have been used to develop more general parameterizations intended to be used in regional and global climate models (e.g., Meyers et al. (1992); DeMott et al. (2010); Phillips et al. (2012)). Generally, most of these parameterizations assume a temperature or humidity dependent power law behavior of the ice crystal concentration.

Meyers et al. (1992) parameterized the ice nucleation concentration n_{ice} observed for combined condensation freezing and deposition nucleation as a power law relation depending only on the saturation ratio S_{ice} with

$$n_{ice} = \exp(-0.639 + 0.1296 \cdot 100 \cdot (S_{\text{ice}} - 1)) \; [\text{l}^{-1}] \tag{2.11}$$

The ice nucleation data from which this parameterization was derived was collected during atmospheric field measurements investigating orographic clouds (Rogers, 1982) and the ice nucleation properties of urban air (Al-Naimi and Saunders, 1985) with continuous flow diffusion chambers. This relation is, however, only justified for temperatures between 253

and 266 K and should not be extrapolated beyond this temperature range.

DeMott et al. (2010) parameterized the ice crystal concentration observed at water saturation (immersion freezing) based on an extensive collection of field measurements and derived a temperature dependent relation with

$$n_{ice} = 5.94 \cdot 10^{-5} \cdot (237.16 - T)^{3.33} \cdot n_{aer}^{2.64 \cdot 10^{-2}(273.16-T)+3.3 \cdot 10^{-3}} [l^{-1}] \tag{2.12}$$

where T is the temperature in [K] and n_{aer} refers to the concentration of particles larger than 0.5 µm given in [cm^{-3}].

A parameterization that was tailored more to the specific ice nucleation properties of certain aerosol types was proposed by Phillips et al. (2008) (updated in Phillips et al. (2012)) on the basis of continous flow measurements and corresponding ambient aerosol data. This parameterization distinguishes between four subgroups: dust/metallic, soot, soluble organics and primary biological aerosol particles (PBAP) such as fungi, bacteria and pollen. Note that for estimating the ice crystal number concentration this parameterization uses the aerosol number concentration as well as the aerosol surface that is available for heterogeneous ice nucleation. Additional empirical parameters are the aerosol-specific freezing onsets and factors describing the individual contributions by immersion freezing and deposition nucleation in the thermodynamic regime where both freezing modes may occur. Contact nucleation is parameterized separately and will not be considered explicitly in this work. The contribution of mineral dusts and metallic compounds to the concentration of atmospheric ice nuclei is given by

$$c_{IN,DM} \approx \int_{log[0.1\mu m]}^{\infty} \{1 - \exp[-\mu_{DM}(D_{DM}, S_{ice}, T)]\} \cdot \frac{dn_{DM}}{d(\log D_{DM})} d(\log D_{DM}) [m^{-3}] \tag{2.13}$$

where $\mu_{DM}(D_{DM}, S_{\text{ice}}, T)$ is the average number of activated ice embryos per aerosol particle. $\mu_{DM}(D_{DM}, S_{\text{ice}}, T)$ is defined in Phillips et al. (2008) as a function of aerosol diameter D_{DM}, temperature T in [°C] and relative humidity over ice S_{ice}. n_{DM} is the number mixing ratio of aerosol particles belonging to the dust/metallic compounds group given in [kg^{-1}]. Thus, $c_{IN,DM}$ is given as a number mixing ratio but it is approximately equal to the number concentration given in [m^{-3}].

2.5 Ice nucleation parameterizations in climate models

Numerical models covering different spatial and temporal scales have been used to estimate the contribution of heterogeneous ice nucleation to the observed ice crystal concentration (e.g., Liu et al. (2012), Spichtinger and Gierens (2009), Barahona and Nenes (2009)). Also, the role of different aerosol particle species as atmospheric ice nuclei has been investigated. Selected results from modelling studies relying on different ice nucleation parameterizations as described in the previous sections will be discussed briefly in the following paragraphs.

Ice nucleation in cirrus clouds can either occur in solution droplets (homogeneous ice nucleation) or as heterogeneous nucleation initiated by aerosol particles such as mineral dust. Depending on temperature and relative humidity over ice, immersion freezing and deposition nucleation are possible ice nucleation pathways. For some thermodynamic conditions homogeneous as well as heterogeneous ice nucleation can occur. The share of aerosol induced ice formation, however, is not only determined by the ice nucleation efficiencies of the aerosol particles but also by feedbacks between droplets and ice crystals within the clouds. Thus, numerical models have specifically investigated the competition between freezing of solution droplets and heterogeneous ice nucleation in cirrus clouds. Spichtinger and Cziczo (2010) describe ice nucleation within a box model by different freezing thresholds and find that heterogeneous ice nucleation influences the temporal development of relative humidity over ice in cirrus clouds. This deviation causes homogeneous freezing to be either diminished or even completely suppressed (Spichtinger and Gierens, 2009). A parcel model study conducted by Kärcher and Lohmann (2003) finds that aerosol particles with low freezing thresholds decrease the number of ice crystals compared to cirrus cloud formation by purely homogeneous freezing. This effect, however, depends not only on the distribution of freezing thresholds among the aerosol particles but also on the updraft velocity of the simulated air parcel (Kärcher and Lohmann, 2003). With regard to freezing in cirrus clouds, many models agree on the fact that heterogeneous

ice nucleation becomes especially important for low updraft velocities ($w < 0.2$ ms^{-1}) and high ice nuclei concentrations (Spichtinger and Cziczo, 2010; Sassen and Benson, 2000). Thus, the presence of heterogeneous ice nuclei can have a significant influence on the structure of cirrus clouds, but also on mixed-phase clouds in lower layers of the atmosphere.

As a next step, other models have been used investigate the influence of different aerosol species on atmospheric ice nucleation processes while relying on different ice nucleation parameterizations. Hoose et al. (2010) used classical nucleation theory with aerosol specific contact angles to investigate the contribution of mineral dust, biological particles and soot to the global ice crystal concentrations. Mineral dust particles were found to have a large impact on ice formation on mixed-phase clouds and also soot might have a distinct impact on heterogeneous ice nucleation. Biological particles, however, were found to contribute only marginally to cloud ice nuclei (Hoose et al., 2010). Within the uncertainty ranges, these estimates also agree with field measurements (see references in Hoose et al. (2010)).
Ice nucleation parameterizations other than classical nucleation theory were also able to reproduce observations. Eidhammer et al. (2009) showed that the parameterization proposed by Phillips et al. (2008) is able to predict ice crystal concentrations within the range of observed concentrations. Note, however, that these measured atmospheric ice crystal concentrations also may scatter over several orders of magnitudes at a given temperature. Comparing several parameterizations, some studies find that parameterizations developed from the Phillips et al. (2008) parameterization might underestimate ice crystal concentrations in contrast to classical nucleation theory based approaches (Liu et al., 2012; Curry and Khvorostyanov, 2012). Another study comparing ice crystal concentrations calculated with different parameterization concluded that the Phillips et al. (2008) parameterization predicted higher tropospheric ice crystal concentrations - at least in the Northern Hemisphere - than the parameterization developed by Meyers et al. (1992) (Yun and Penner, 2012). In the study by Niemand et al. (2012) an INAS density based parameterization describing immersion freezing of dust particles is compared to the Phillips et al. (2008) parameterization, the approach proposed by DeMott et al. (2010) and clas-

sical nucleation theory (Hoose et al., 2010). At 255 K, the ice crystal concentrations predicted by Hoose et al. (2010) and Phillips et al. (2008) agree well with atmospheric measurements whereas the approaches proposed by DeMott et al. (2010) and Niemand et al. (2012) result in ice crystal concentrations which are by one order of magnitude lower than the measured values. Note, however, that the atmospheric measurements bear a considerably large measurement uncertainty. Also, the parameterization developed by Niemand et al. (2012) only considers freezing of mineral dust particle whereas the atmospheric measurements might be influenced by a contribution by highly ice-active biological particles such as pollen or bacteria.

From these model comparisons it can be concluded that the general parameterizations do not always agree with each other and therefore more aerosol specific parameterizations should be developed in order to improve the representation of heterogeneous ice nucleation processes within models and consequently the agreement with observations. Hence, there is also the need for more extended atmospheric measurements relying on different ice nuclei counters to decrease the measurement uncertainties.

In the following chapters, the INAS density approach will be extended towards a temperature and humidity dependent formulation for describing deposition nucleation. This approach will then be compared to the parameterizations developed by Phillips et al. (2008) and Meyers et al. (1992).

Chapter 3

Investigating ice nucleation properties of mineral dusts with AIDA cloud chamber experiments, box model calculations and cold stage studies

3.1 AIDA cloud chamber experiments[1]

The ice nucleation properties of aerosol samples can be investigated at the AIDA (Aerosol Interaction and Dynamics in the Atmosphere) aerosol and cloud chamber facility at the Karlsruhe Institute of Technology under atmospherically relevant conditions. Within the AIDA chamber humidified air can be expanded and thereby cooled, simulating the ascent of an air parcel in the atmosphere. The expansion process is almost adiabatic with

$$\frac{dT_g}{dp} = \frac{R_a}{c_{p,a}} \cdot \frac{T_g}{p} \tag{3.1}$$

[1]This section was partly taken from "Ice nucleation properties of fine ash particles from the Eyjafjallajökull eruption in April 2010" (Steinke et al., 2011)

where T_g is the temperature within the AIDA cloud chamber vessel, p is the pressure, R_a and $c_{p,a}$ are the gas constant and the specific heat capacity of moist air. Note that the walls of the cloud chamber vessel are not actively cooled and thus stay close to the initial temperature. The walls therefore provide a source of heat and water vapor to the volume within the AIDA chamber.

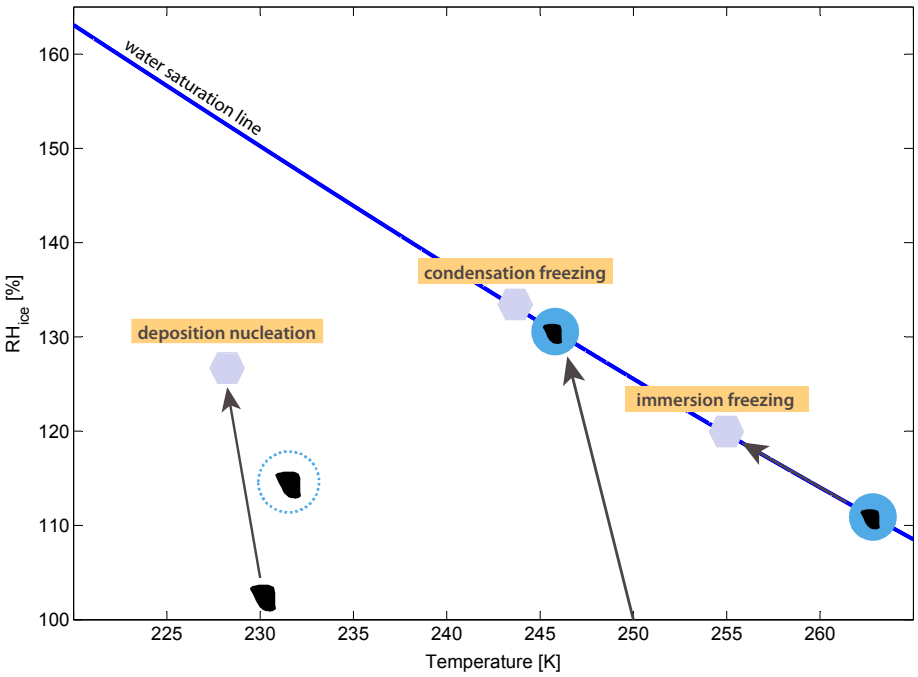

Figure 3.1: *Ice nucleation modes observed during AIDA cloud chamber experiments depending on temperature and relative humidity over ice; arrows indicate possible experimental trajectories (adapted from Hoose and Möhler (2012))*

Experiments in the cloud chamber typically follow a trajectory where the gas temperature decreases while the relative humidity increases. Possible trajectories are indicated by the arrows in Fig. 3.1. Depending on temperature and relative humidity, different ice nucleation modes can be observed. At temperatures above 240 K, many aerosol particles initiate ice nucleation via the condensation or immersion freezing pathway as depicted in Fig. 3.1. Within this work, all freezing events observed after droplet activation are attributed to immersion freezing. At lower temperatures, ice nucleation is typically initiated through the deposition nucleation mode which occurs at subsaturated conditions with

respect to water. Contact nucleation is not considered in this work because in most of the experiments all particles are activated to droplets and thus no dry interstitial aerosol particles are available for contact nucleation. Ice multiplication via the Hallett-Mossop process is assumed to be negligible at temperatures below 260 K (Mossop, 1978).

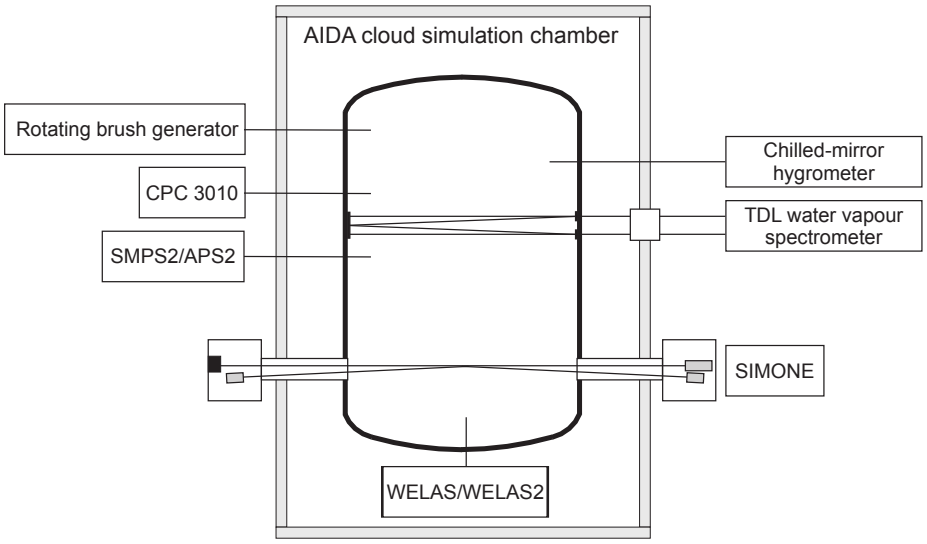

Figure 3.2: *Schematic drawing of the AIDA cloud chamber: aerosol instrumentation (rotating brush generator, APS, SMPS, CPC3010) and instruments used for characterization of the droplet/ice crystal population (welas/welas2, SIMONE) and for the relative humidity measurements (TDL, chilled-mirror hygrometer)*

Figure 3.2 shows a schematic drawing of the AIDA chamber: the vessel, where the experiments take place, is situated within a large temperature-controlled housing. For the expansion experiments, the gas pressure inside the vessel is lowered at controllable rates with a strong vacuum pump. Rigorous cleaning (i.e. pumping the vessel down to pressures below 0.1 hPa and flushing with synthetic air) results in very low background concentrations of aerosol particles (typically below 0.1 cm^{-3}). Additionally, most expansion experiments were preceded by a reference activation during which the background aerosol is activated to droplets or ice crystals, depending on the temperature and humidity conditions within the chamber.

With several optical instruments, aerosol particles, droplets and ice crystals can be measured and distinguished from each other. In the following, the characteristics of these instruments (Wagner et al., 2009) will be summarized briefly:

- Sizing and counting of the droplet and ice crystal population is done by the two optical particle counters **welas** and **welas2** (Palas GmbH) which detect scattering signals from single particles crossing a beam of white light within the respective instrument. The intensity of the scattering pulses is then taken as a measure of the corresponding particle size. The detection ranges (for liquid droplets) are 0.8–46 µm and 5.0–240 µm, respectively (Saathoff et al., 2013). Depending on the observed ice nucleation mode and the initial size distribution of the aerosol particles, a size threshold can be set which allows to calculate the number concentration of ice crystals.

- **SIMONE** (Scattering Intensity Measurements for the Optical Detection of Ice) detects scattering signals from particles crossing the pathway of a laser beam (λ = 488 nm) which horizontally traverses the cloud chamber. Scattering signals are measured in forward (at 2°) and near-backward (at 178°) direction. Additionally, for the near-backward scattering signal, the depolarization, which can be taken as an indicator of the dominating presence of either water droplets or ice crystals, is measured using a Glan laser prism to separate the parallel and the perpendicular polarized components of the near-backward scattered light.

- The humidity conditions in the cloud chamber are derived from **TDL** (tunable diode laser) absorption spectroscopy measurements. From scanning over a selected water-vapor absorption line at 1.37 µm, the absolute concentration of water vapor within the cloud chamber can be inferred with an accuracy of ±5% (Fahey et al., 2009). The concentration measurements can then be converted into relative humidity values using the AIDA mean gas temperature T_g and the saturation vapor pressure of water (Murphy and Koop, 2005). Additionally, the total water concentration can be determined from chilled mirror hygrometer measurements.

With this instrumentation, ice nucleation via immersion freezing can be clearly distinguished from deposition nucleation.

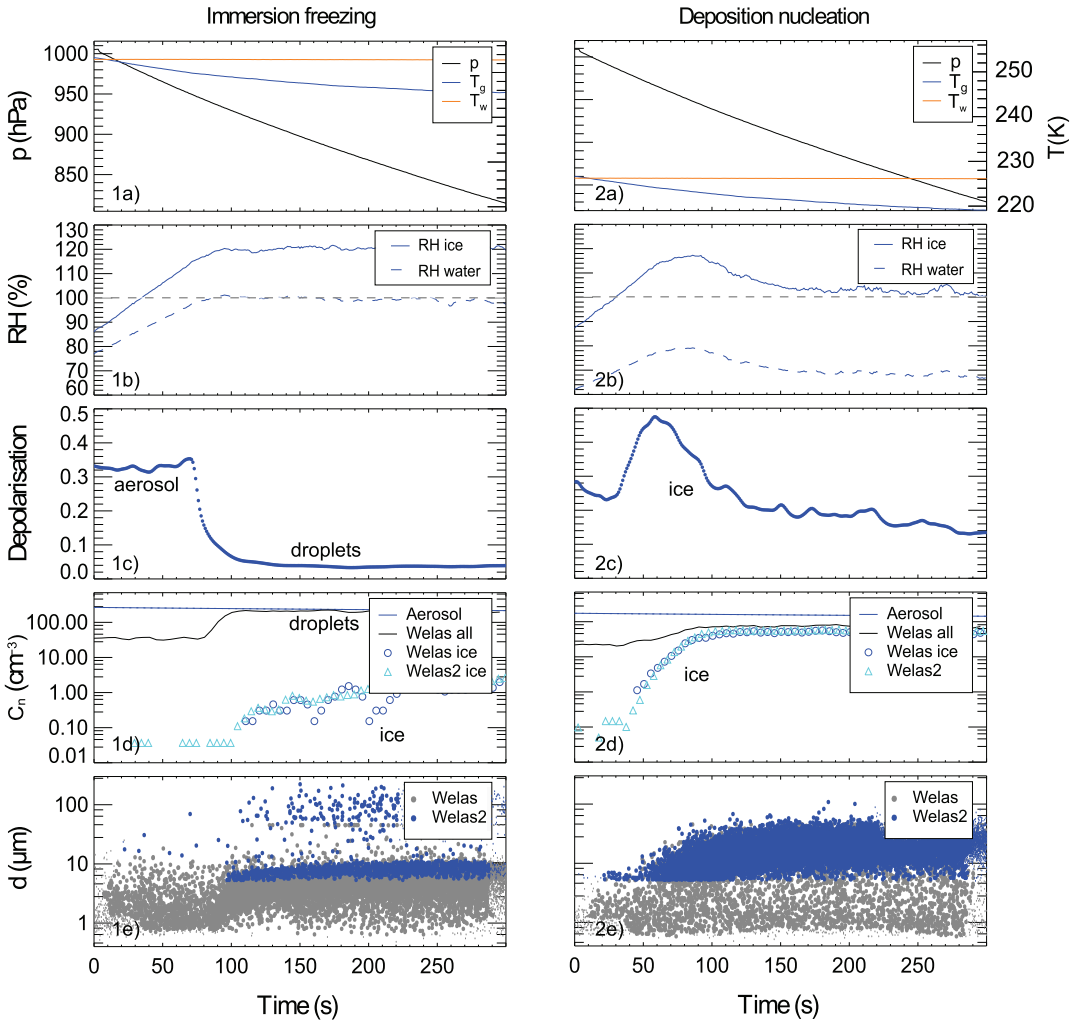

Figure 3.3: *Time series of two experiments showing immersion freezing (1a-1e) and deposition nucleation (2a-2e)*

a) *Variation of the thermodynamical variables during expansion: decrease in gas temperature T_g and pressure p; the temperature at the walls of the vessel T_w stays approximately constant.*

b) *Development of relative humidity over water and over ice as derived from TDL data.*

c) *Depolarization of the backwardly scattered light (SIMONE) as an indication for the dominance of either droplets or ice crystals.*

d) *Aerosol number concentrations (CPC3010) compared to particle concentrations (welas/welas2); ice crystal number concentrations are calculated from welas/welas2 data.*

e) *Temporal evolution of particle sizes as measured by welas/welas2.*

In Fig. 3.3 data for two experiments is shown – the experiment on the left (1a to 1e) is an example for immersion freezing of volcanic ash (EY01), whereas the experiment on the right side (2a to 2e) is characterized by pure deposition nucleation initiated likewise by volcanic ash.
As the structure of the data sets is conceptually the same for both experiments, a general overview will be given, together with the main conclusions that can be drawn from the measurements:

- The first panels a) show the progression of an expansion experiment: the cloud chamber is pumped down from atmospheric pressure to a pressure p of ~ 800 hPa. At the same time, the gas temperature T_g, which is the average temperature in the volume of the cloud chamber, drops as approximately decribed by eq. 3.1. The temperature T_w, which is the average of several sensors on the walls of the aerosol vessel, remains almost constant during the expansion. The temperature uncertainty is ΔT_g = 0.3 K (Möhler et al., 2006).

- Panels b) show the evolution of the relative humidities over water (RH_{wat}) and over ice (RH_{ice}) as derived from the TDL water vapor measurements.

- The SIMONE depolarization signal is shown in panels c): a depolarization value of ~ 0.3 was observed for the volcanic ash particles. The growth of droplets and ice crystals can be clearly differentiated: formation of (spherical) droplets is accompanied by a decrease in depolarization. For immersion freezing experiments with only low number concentrations of nonspherical ice crystals with a concomitant high droplet number concentration there is no significant change in the depolarization due to the the formation of ice crystals.

- The particle concentrations and size distributions that are shown in the panels d) and e) are compilations of data from welas, welas2 and CPC3010. The welas and welas2 instruments give information regarding the number concentrations (panels d) and optical sizes (panels e) of droplets and ice crystals. The particles measured by welas/welas2 before the expansion experiment starts are aerosol particles that are large enough to be detected by these instruments. In panel d), the number

concentration as measured by the two optical particle counters is shown without differentiating between aerosol particles, droplets and ice crystals (welas all). Additionally, the ice crystal concentration can be derived by applying a size threshold to the data presented in panels e) according to the fact that ice crystals are typically much larger than aerosol particles and droplets. For the immersion freezing experiment, the size separation between droplet population and ice crystals is clearly visible (1e). Thus, the threshold is set at a particle size of d = 20 µm. For deposition nucleation, this ice crystal threshold is set to a slightly smaller value of d = 15 µm in order not to underestimate the number density of small ice crystals. Complementing the data on droplets and ice crystals, the aerosol particle concentration is shown in panels d).

Putting together the information from all the instruments, it is possible to distinguish between immersion freezing (1a to 1e) and deposition nucleation (2a to 2e): First, from looking at the humidity data (1b and 2b) it can be seen that water saturation is only reached during the first experiment. The emergence of droplets is confirmed by the decrease of the depolarization signal (1c) from ~ 0.3 to values below 0.05 – this can be reasoned by the fact that aerosols which have been activated to droplets, in contrast to dry aerosol particles, are spherical objects which do not cause significant depolarization. Ice nucleation sets in only after droplet formation has started (1d, 1e).
For deposition nucleation, the depolarization signal (2c) is more difficult to interpret because it also depends on ice crystal sizes and habits: during our experiments, overall, a slight decrease in depolarization was observed during deposition nucleation. Sometimes, however, the initiation of deposition nucleation can be accompanied by an increase in depolarization (2e) which can be explained by the presence of small micrometer-sized ice particles during the initial nucleation and growth stage as such small particles have a maximum in depolarization (Wagner et al., 2009). Deposition nucleation is also associated with an immediate growth of ice crystals at a certain supersaturation over ice (2d, 2e)

Aerosol samples were generally introduced into the AIDA chamber with a rotating brush generator (RBG 1000, Palas GmbH) combined with one or several cyclone impactor stages which allow for defining a particle size cutoff. The aerosol size distribution for

each aerosol sample is derived from combining SMPS (Scanning Mobility Particle Sizer – TSI) and APS (Aerodynamical Particle Sizer – TSI) measurements. From the aerosol particle size distribution that is obtained by combining the APS and SMPS data (Möhler et al., 2008a), the aerosol surface distribution can be estimated from the mobility diameters and subjected to a lognormal fitting routine.

Within this work, the cloud chamber was used to investigate the ice nucleation properties of different mineral dust species such as fossil diatomite, desert dusts and soil dusts with a complex organic composition. The ageing of atmosperic aerosol was also simulated by letting sulfuric acid or volatile secondary organics condense onto the aerosol particles' surfaces. The ice nucleation properties of these aged mineral dust particles were then compared to uncoated mineral dust particles.

3.2 Numerical modelling with ACPIM

The AIDA cloud chamber simulates the ascent of cloud parcels in the atmosphere and the activation of aerosol particles to droplets and ice crystals. Complementary, the box model ACPIM (Aerosol-Cloud-Precipitation Interaction Model, University of Manchester, Connolly et al. (2009)) is able to calculate the ascent of virtual air parcels allowing for a more detailed investigation of aerosol-cloud-processes. ACPIM assumes a closed parcel which does not exchange energy or moisture with the environment. The change in temperature is described by

$$\frac{dT}{dt} = \left(\frac{R_m}{p} \cdot \frac{dp}{dt} - \frac{L_v}{T} \cdot \frac{dr_v}{dt} + \frac{L_f}{T} \cdot \frac{dr_i}{dt} \right) \cdot \frac{p}{c_{pm}} \tag{3.2}$$

where T is the temperature within the air parcel, R_m is the gas constant for moist air, p is the pressure, L_v is the latent heat for vaporization, r_v is the vapor mixing ratio, L_f is the latent heat of fusion, r_i is the ice mixing ratio, and c_{pm} is the specific heat of moist air. The total water content is described by

$$\frac{dr_v}{dt} + \frac{dr_l}{dt} + \frac{dr_i}{dt} = 0 \tag{3.3}$$

with r_l being the liquid water mixing ratio. Note that for the AIDA cloud chamber neither eq. 3.2 nor eq. 3.3 hold strictly because during an expansion experiment the walls of the

cloud chamber act as a source of heat and moisture.

The box model describes aerosol particles and droplets within a two-dimensional grid where each grid point corresponds to a certain mass ratio between water and dry aerosol mass at a defined particle size. A similar grid structure is applied for describing the interaction between aerosol particles and ice crystals. ACPIM also encomprises a detailed aerosol thermodynamics scheme which describes hygroscopic growth and subsequent droplet activation of aerosol particles (Topping et al., 2005; Dearden et al., 2011). In this work, the model is mainly used to test an ice nucleation active surface site density approach with additional time dependent source terms. Note that ACPIM is also able to describe processes relevant to immersion freezing and deposition nucleation, including secondary processes such as riming, aggregation and ice multiplication (Connolly et al., 2012). However, for the modelling studies presented in this work these processes were not considered. The aerosol size distributions were set up with a minimum particle size $d = 0.002$ µm and extended up to $d = 10^5$ µm. The bin sizes were determined by using a logarithmic scaling factor of 2. For the simulations presented in this work, the time step was chosen to be $\Delta t = 5$ s. The updraft velocities of the simulated air parcels were prescribed as fixed values.

The results from using ACPIM to investigate the contributions of time dependent source terms to the predicted ice crystal concentrations will be presented in the next chapter.

3.3 Cold stage experiments

With experiments at the AIDA cloud chamber, ice nucleation properties of complex aerosol populations can be observed under atmospherically relevant conditions. However, the detailed observation of microphysical ice nucleation processes is not possible during large scale cloud chamber experiments.

It has been postulated that heterogeneous ice nucleation occurs at characteristic surface sites (Fletcher, 1969) which possess physico-chemical properties distinguishing those sites from the average aerosol surface. However, the exact nature of these sites remains unclear because of the high variability with regard to the chemical composition of different

aerosol species. Additionally, most natural aerosol particles exhibit a very complicated morphology as shown in Fig. 3.4 for a mineral dust particle.

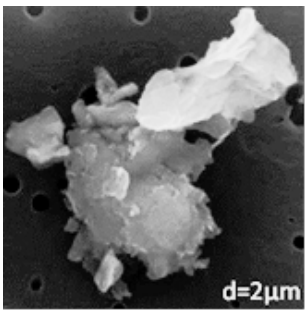

Figure 3.4: *Microscope image of a mineral dust particle (courtesy of A. Kiselev)*

It has been speculated that the spatial arrangement of certain molecules at the surfaces of aerosol particles is able to mimic the hexagonal structure of ice which lowers the energy barrier for the formation of ice crystal precursors (Pruppacher and Klett, 1997). Contrasting this approach, however, molecular dynamics simulations suggest that the determining factor is not so much the ice-like lattice structure of molecules at the particle surface but is probably more likely that certain groups of hydrophilic molecules enhance the adsorption of water molecules to the surface where then hydrogen bonds between adjacent molecules can form more easily (Nutt and Stone, 2004). Simulations investigating freezing at a kaolinite surface suggest that the ice nucleation ability of kaolinite is not mandated by a good lattice match but rather by a long-range ordering effect exhibited by the kaolinite surface which results in an ice-like layer close to the surface (Cox et al., 2013).

Note that the exact structure of the initial ice clusters is still under debate. Experimental evidence suggests that ice clusters might not consist of purely hexagonal molecular structures but also encomprise cubic ice or amorphous structures (Cox et al., 2012; Carrasco et al., 2009). It has also been proposed that surface defects such as trenches might be favorable for the formation of ice (Croteau et al., 2010). Hence, as a first step towards investigating the interaction between aerosol particles and the ice phase, an experimental setup has been built which allows to investigate the freezing of small droplets (d = 90 µm) which have been placed on certain substrates.

At the heart of the experimental setup is a temperature controlled stage (cold stage) upon which different substrates such as silicon wafers can be placed. The cold stage setup has been described in detail in the work by diNatale (2012). A sketch of the experimental setup is shown in Fig. 3.5.

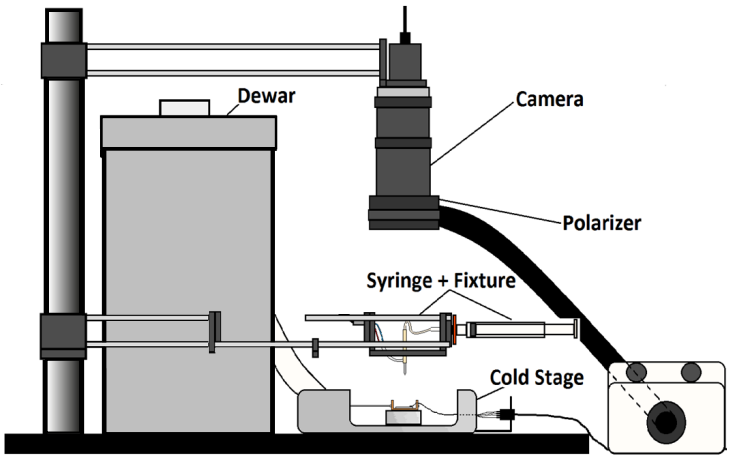

Figure 3.5: *Schematic drawing of the cold stage setup (adapted from Haarig (2013))*

Individual substrates are cooled down to the dew point temperature before an array of several hundreds of small water droplets (d = 90 µm) is printed onto the substrate. The droplets are printed with a piezo-electric injector using a standard syringe as reservoir for deionized water (setup described in Duft and Leisner (2004)). Note that close to the dew point, evaporation or condensational growth of droplets is assumed to be negligible.
The temperature is measured directly at the surface of each substrate. Droplets typically are cooled at rates between 1 and 10 K/min by using liquid nitrogen as coolant.
The freezing of droplets as the temperature decreases during an experimental run is detected by observing light scattered back from the droplets or ice crystals. The light source in this experimental setup consists of LEDs which are arranged as a ring. The white light emitted from these LEDs is transmitted through a polarization filter with linear polarization. A camera is situated above the cold stage and detects light transmitted through a second polarization filter after being scattered back from the droplets or ice crystals.
Figure 3.6 (left) shows an array of liquid water droplets as they are viewed by the camera

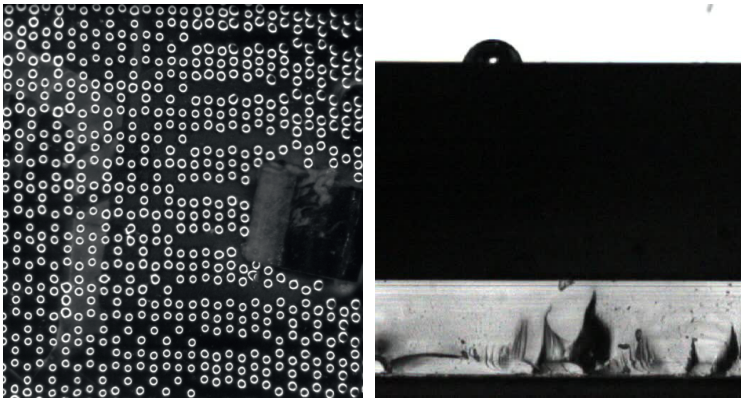

Figure 3.6: *Array of water droplets on a silicon wafer and close-up side view of a sessile droplet on top of a silicon wafer (courtesy of M. Haarig)*

before the start of an experimental run. A magnified view of a single droplet at room temperature is depicted in Fig. 3.6 (right). Water contact angles of droplets vary between 30° and 85° for the materials that have been investigated (Haarig, 2013). From the initial image showing the liquid droplets their positions on the substrate are determined and from the increase of backscattered white light intensity within these individual regions of interest the freezing of droplets is diagnosed. This information is then used to derive temperature dependent freezing curves.

In order to develop a better understanding of the microphysical processes contributing to heterogeneous ice nucleation, several substrates with different characteristics (e.g. surface roughness) were investigated. Monocrystalline materials such as silicon (Plano GmbH), graphite and copper (Goodfellow Ltd.) are commercially available and may be used as ice nucleus substitutes with very regular surfaces. The roughness of monocrystalline surfaces varies among different materials with copper exhibiting an average surface roughness in the range of micrometers whereas silicon is much smoother with roughness values in the range of nanometers. However, the surface structure of these materials is much less complicated than the morphology of natural aerosol particles such as mineral dust particles (Fig. 3.4). Note that all substrates have been subject to different cleaning procedures as described in the work by Haarig (2013).

The chemical composition of muscovite (Conrad) is much closer to natural mineral dust particles than the monocrystalline substrates. Therefore, the ice nucleation properties of muscovite were investigated with the cold stage setup as well. Also, the influence of trenches on the ice nucleation properties of silicon wafers were investigated. These experiments are then compared to results from cold stage experiments with mineral dust suspension droplets in order to link the ice nucleation behaviour of very defined surfaces to the freezing properties of complex natural aerosol particles. For comparing between the different ice nucleating materials, the ice nucleation active surface site density approach (see ch. 2) was used. First results from the cold stage studies are presented in the next chapter.

Chapter 4

Experimental results

4.1 Time dependence of deposition nucleation: AIDA experiments with Arizona Test Dust as a test case

Developing ice nucleation parameterizations from cloud chamber studies is a further step towards improving the implementation of cloud microphysics within global and regional climate models. The AIDA cloud chamber is generally used to simulate the ascent of cloud parcels in the atmosphere and to investigate the formation of ice crystals under atmospherically relevant conditions. The cooling rates can be varied, providing access to different ice nucleation time scales. Hence, AIDA cloud chamber experiments might help to answer the question at which cooling rates and for which aerosol types the inherent stochasticity of ice nucleation must be explicitly considered by ice nucleation parameterizations. For the experiments presented in this section, the AIDA cloud chamber is used to simulate cirrus cloud conditions for investigating deposition nucleation initiated by dust particles.

4.1.1 AIDA deposition nucleation experiments

Deposition nucleation experiments with Arizona Test Test Dust were conducted at the AIDA cloud chamber. Arizona Test Dust (ATD, Powder Technology Inc.) is used as a substitute for naturally occuring desert dusts. Note that ATD consists of desert dust which was washed, dried and milled to provide enough material in all size classes. Thus, the composition of individual ATD particles is probably more homogeneous than the composition of original desert dusts and also the surface properties might differ from natural dusts. To investigate the impact of time dependence and variations in the aerosol size distribution on the deposition nucleation efficiency of ATD, the experimental cooling rate was varied between 0.3 K/min and 2.9 K/min and also the aerosol size distribution was varied by either including or discarding particles larger than 1 µm. Several sets of experimental runs were conducted, starting at 250 K, 235 K or 220 K.

- For all experiments, the ice nucleation efficiency was quantified by determining the ice nucleation thresholds and by calculating ice nucleation active surface site (INAS) densities and the contact angle distribution parameters. The contact angle distribution parameters are derived by using classical nucleation theory to fit the observed ice fractions (eq. 2.1). An average INAS density function (eq. 2.9) was derived and compared to two empirically derived parameterizations (Meyers et al., 1992; Phillips et al., 2008) with regard to their sensitivity to temperature and relative humidity over ice.

- The relevance of time dependence to ATD deposition nucleation was inferred by describing the time dependent contribution either by a linear time dependent source term or by an exponential function increasing time. The INAS density functions - with and without the time dependent source terms - were then tested within the box model ACPIM with regard to the impact of variations in cooling rate and aerosol number concentration on the observed ice fractions.

An overview of all experiments considered in this study is provided in Table 4.1. Note that cyclone impactors are used to define an aerosol particle size cutoff at approximately 1 µm. With a defined cutoff the disproportional contribution of larger aerosol particles to the observed formation of ice can be eliminated. Only two experiments were conducted

without using cyclone impactors (see Table 1: IN17_22 and IN17_24).

During all experiments that are listed in Table 4.1 the ice crystal concentrations as well as the aerosol size distributions were measured. The cooling rate and the aerosol surface were varied in a systematic manner in order to investigate the impact of these factors on the observed ice crystal concentration. The cooling rate determines the time scale that is relevant to the observed ice nucleation and thus gives experimental access to the time dependence of heterogeneous ice nucleation.

Table 4.1: Overview of ice nucleation experiments with ATD as carried out at the AIDA cloud chamber; reference experiments being omitted

Experiment	T_{start} [K]	Aerosol concentration [cm^{-3}]	Median diameter [µm]	Aerosol surface area density [$\mu m^2 cm^{-3}$]	Cooling rate [K/min]
IN17_01	250.2	99	0.25	23	0.3
IN17_02	249.2	137	0.24	40	0.6
IN17_04	249.9	43	0.24	9	0.5
IN17_06	249.7	38	0.21	10	0.3
IN17_08	250.1	62	0.24	17	0.3
IN17_10	249.8	44	0.24	14	2.5
IN17_11	249.8	504	0.23	119	2.7
IN17_12	249.7	508	0.23	126	0.8
IN17_13	250.2	500	0.24	139	0.4
IN17_15	234.7	22	0.22	6	1.1
IN17_16	235.3	26	0.20	9	2.9
IN17_18	234.8	151	0.23	40	2.8
IN17_21	234.8	107	0.19	18	1.1
IN17_22*	235.5	171	0.37	162	1.1
IN17_24*	235.0	139	0.35	209	1.1
IN17_26	235.4	48	0.22	13	0.7
IN15_04	222.8	451	0.22	100	2.4
IN15_12	222.7	809	0.24	201	2.7

Deposition nucleation is a process that depends largely on relative humidity over ice, but also on temperature. Due to experimental restrictions not all areas in the T/RH_{ice} space are accessible during AIDA cloud chamber experiments. The initial cooling phase is always accompanied by an increase in RH_{ice} which defines trajectories in the T/RH_{ice} space.

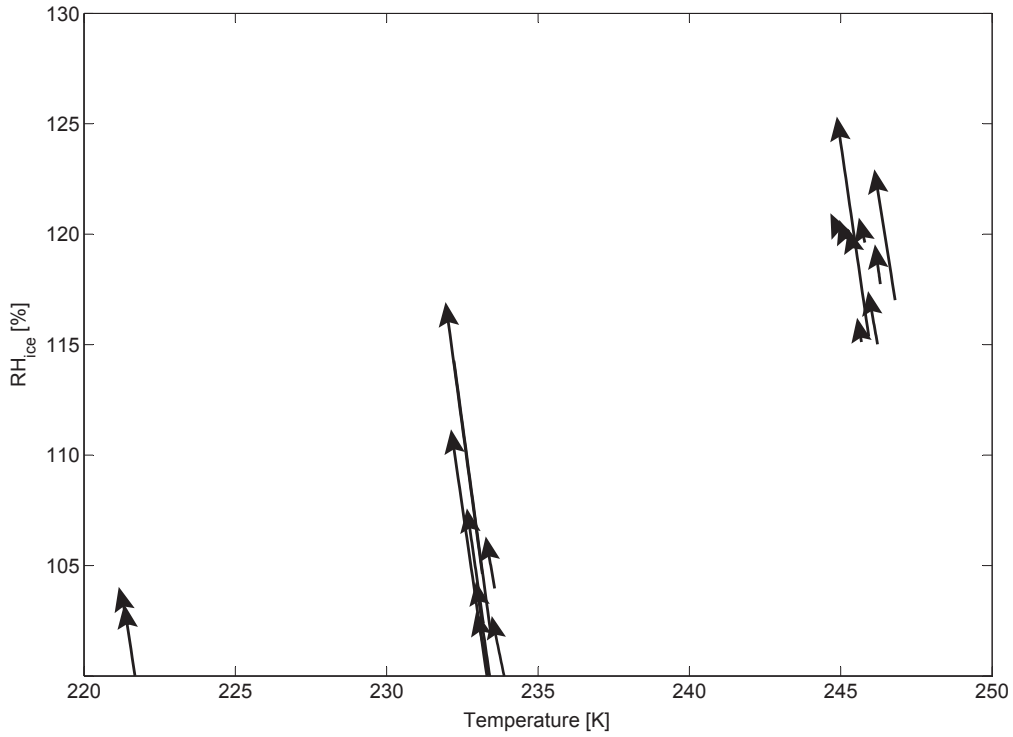

Figure 4.1: *Trajectories of ice nucleation experiments: temperature and RH_{ice} change simultaneously during expansion experiments; trajectories are shown from the point on when ice crystal concentrations first exceed background concentrations - only the part is shown for which RH_{ice} increases linearly with temperature*

Figure 4.1 shows trajectories of all AIDA expansion experiments described in Table 1. All trajectories in Fig. 4.1 start shortly after ice formation was observed and end when ice crystal growth leads to a deviation from the linear increase in RH_{ice}. All experimental runs began at initially subsaturated conditions with respect to ice. From Fig. 4.1 it can be observed that trajectories for experiments starting at 235 K are more similar to each other than those of the experiments at warmer temperatures.

4.1.2 Aerosol surface distribution of ATD particles

Information about the total aerosol surface area density is needed to calculate the INAS densities. The aerosol surface area density is derived from the measured size distribution after conversion into an aerosol surface distribution. To this surface distribution a log-normal fit is applied from which the total aerosol surface area density can be estimated through integrating the distribution. An exemplary aerosol surface distribution is shown in Fig. 4.2.

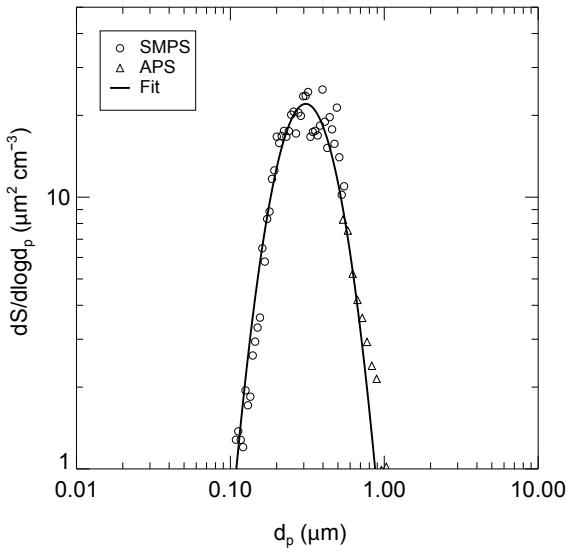

Figure 4.2: *Aerosol surface distribution for dust particles (Arizona Test Dust) with lognormal fit:* $d_{med,surf}$ = 0.32 *µm;* σ_{surf} = 1.55 *(exp. IN17_04)*

Note that APS and SMPS data in combination cover the whole size range. The median diameter of the surface distribution lies at $d_{med,surf}$ = 0.32 µm, whereas the median diameter of the number size distribution is $d_{med,num}$ = 0.24 µm. In most experiments, the aerosol size distribution was cut off at about 1 µm by using cyclone impactor stages after the rotating brush generator. Only for exp. IN17_22 and exp. IN17_24, the impactor stages were not used, resulting in a shift of the size distribution towards larger sizes with $d_{med,num}$ = 0.35 µm and $d_{med,num}$ = 0.37 µm (see also Table 4.1).

4.1.3 Ice nucleation properties of ATD

Thermodynamic ice nucleation thresholds

The relative humidities over ice for which an ice number fraction f_{ice} = 1% was observed are presented in Fig. 4.3 separately for experiments starting at T_{start} = 250 K (Fig. 4.3, top) and T_{start} = 235 K (Fig. 4.3, bottom).

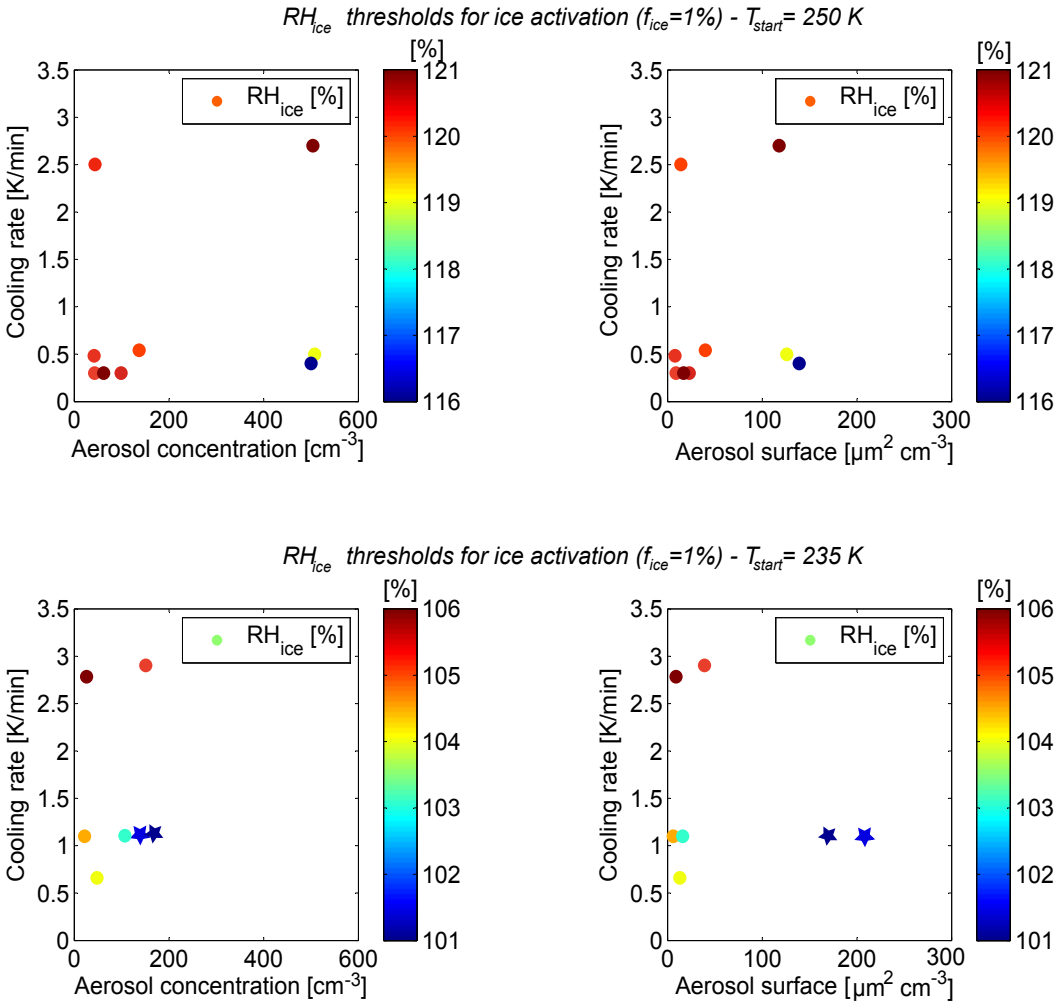

Figure 4.3: *Thermodynamic thresholds for ice nucleation: relative humidity over ice at an ice number fraction f_{ice} = 1% for experiments starting at T=250 K (top row) and at T=235 K (bottom row); symbols indicate variations in the aerosol size distribution with • denoting standard experiments using cyclones for defining a aerosol size cutoff, and ⋆ for experiments without cyclones resulting in a shift of the aerosol size distribution towards larger particles*

For the experiments starting at 220 K, rapid ice nucleation was observed slightly above ice saturation (data not shown). Furthermore, the humidity thresholds are shown either with respect to the initial aerosol concentration of each experiment (Fig. 4.3, left) or with respect to the total aerosol surface area density (Fig. 4.3, right). Also, in the subgraphs of Fig. 4.3 the relation between humidity thresholds and cooling rate is depicted. Fig. 4.3 shows that for T_{start} = 250 K the relative humidity thresholds vary non-systematically (i.e. no correlation with the cooling rate) between 116% and 121%, whereas for T_{start} = 235 K ice nucleation already occurs at relative humidities slightly above saturation and humidity thresholds vary between 101% and 106%. For experiments with the aerosol size distribution being shifted towards larger particles (T_{start} = 235 K) the ice nucleation onset is observed at the lowest relative humidities compared to the other experiments. This observation agrees with the assumption that larger particles within an aerosol population reduce the onset humidity threshold. The range of the observed humidity values corresponds to the measurements uncertainty $\Delta RH_{ice} \approx 3 - 5\%$ with the thresholds for larger particles being at the lower end of the observed humidity values. Figure 4.3 shows that there is no stringent relation between relative humidity thresholds and cooling rates. If ice nucleation was best described by a purely temperature or relative humidity dependent INAS density, then we would expect no influence of the cooling rate on the observed ice nucleation thresholds because for a similar aerosol size distribution the ice fraction obtained at a certain temperature or relative humidity will always be the same. Conversely, if ice nucleation was optimally described by a time dependent heterogeneous nucleation rate approach, the freezing onset would have been shifted towards lower relative humidities for low cooling rates. This is due to the fact that for low ice-active particle fractions the observed ice crystal number concentration can be approximated by $\Delta n_{ice} \approx n_0 \cdot J_{het}(T, S_{ice}) \cdot A_{aer} \cdot \Delta t$ where n_0 is the initial particle concentration, J_{het} is the heterogeneous nucleation rate, A_{aer} is the aerosol surface available for ice nucleation and Δt is the time step during which only small changes ΔS_{ice} and ΔT occur. Δt and ΔS_{ice} are related by the experimental cooling rate r with $r = \Delta T/\Delta t$ and thus $\Delta S_{ice}/\Delta t \propto r$ at the beginning of the cooling phase. This means that within the humidity interval ΔS_{ice}, Δn_{ice} will be larger for slow cooling rates because the interval Δt is larger than for fast cooling rates. Because neither a completely singular behavior (i.e. always the same ice nucleation threshold) nor

a relation between cooling rate and thresholds could be deduced from our measurements, the influence of different cooling rates (corresponding to ice nucleation time scales) on the observed ice fraction cannot be inferred directly. A similar behavior is observed for the temperature thresholds (data not shown).

In contrast to the lack of evidence for an impact of changing cooling rates on the ice nucleation thresholds, increasing the aerosol surface by introducing larger particles does lead to reduced ice nucleation thresholds as also observed in other experimental studies (e.g Welti et al. (2009)).

Ice nucleation active surface site densities

As a first step, the ice nucleation efficiency is expressed as the INAS density averaged over the whole aerosol population for each experiment. This INAS density n_s (Niemand et al., 2012) is approximated as

$$n_s = n_{ice}/A_{aer}\ [\mathrm{m}^{-2}] \tag{4.1}$$

with the ice crystal concentration n_{ice} [cm^{-3}] and the total aerosol surface area density A_{aer} [$\mu\mathrm{m}^2\mathrm{cm}^{-3}$]. Note that n_s can also be interpreted as a way of normalizing ice crystal concentrations. Thus, eq. 4.1 may include an implicit time dependence of the observed ice crystal formation.

The INAS densities are depicted in Fig. 4.4 with respect to $\mathrm{RH_{ice}}$ (left) or with respect to a thermodynamic variable x_{therm} (right) which is defined as

$$x_{therm} = -(T \cdot [K^{-1}] - 273.2) + (S_{\mathrm{ice}} - 1) \cdot 100 \tag{4.2}$$

as an approximation for

$$x_{therm} = -1.085 \cdot (T \cdot [K^{-1}] - 273.2) + 0.815 \cdot (S_{\mathrm{ice}} - 1) \cdot 100 \tag{4.3}$$

which was derived from least-square fitting assuming that n_s depends exponentially on temperature and the saturation ratio with respect to ice S_{ice}.

The length of each n_s trajectory generally corresponds to a time period of $\Delta t \leq 25$ s starting at the first observation of ice nucleation. For experiments during which the growth of ice

crystals led to an early deviation from the linear increase of relative humidity over ice, this time interval Δt was chosen to be shorter than 25 s. The time interval Δt was defined with regard to excluding reductions of the observed ice crystal concentration by sedimentation, assuming that the largest ice crystals grow to approximately 100 µm. These large crystals determine the sedimentation time scale and sediment with terminal velocities between 0.1 and 10 cm/s (Westbrook, 2008). This corresponds to sedimentation time scales between 20 and 2000 s for an average fall distance of 2 m (half of the cloud chamber height). Thus, the time scale was chosen to be $\Delta t = 25$ s.

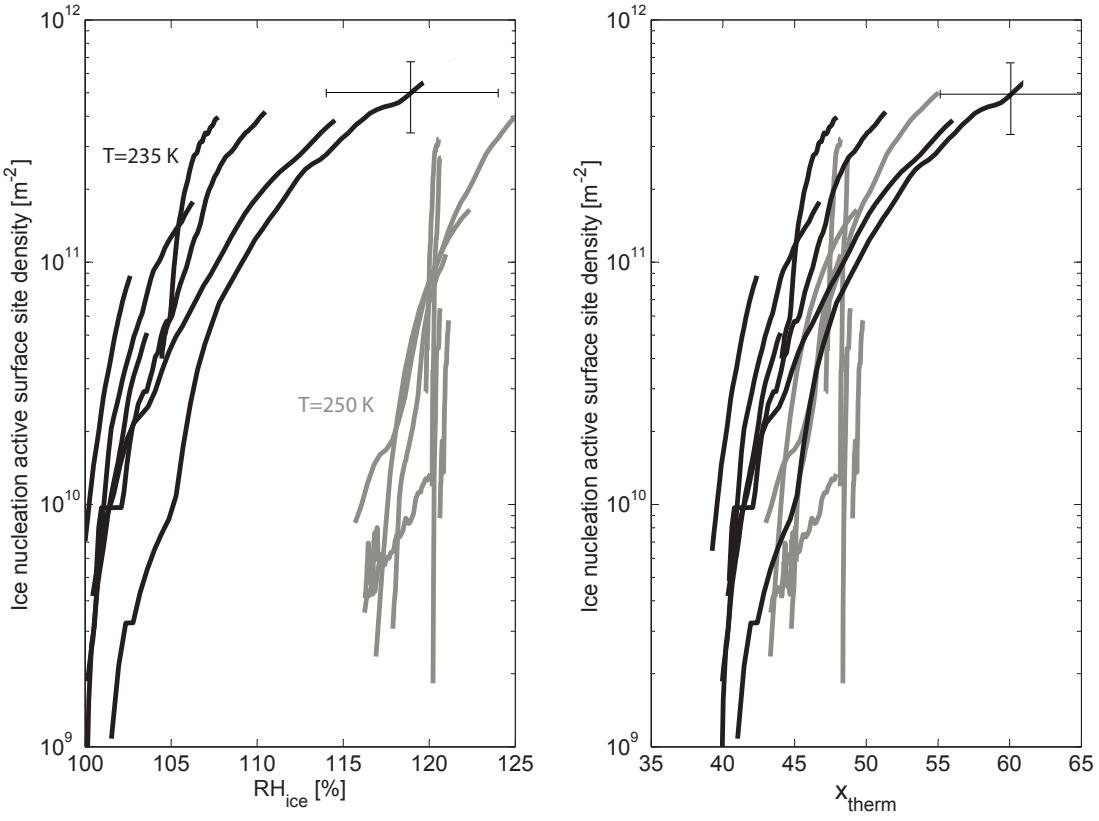

Figure 4.4: *Ice nucleation active surface site densities n_s for all experiments starting either at T_{start} = 235 K or T_{start} = 250 K: INAS densities are depicted with respect to relative humidity over ice (left) and with respect to the thermodynamic variable x_{therm} (right) with $x_{therm} = -(T \cdot [K^{-1}] - 273.2) + (S_{ice} - 1) \cdot 100$*

In Fig. 4.4 (left) the two groups of experiments starting either at 235 K or 250 K are clearly separated. Thus, Fig. 4.4 (left) shows that within the temperature range between 230 and 250 K, deposition nucleation as a process does not only depend on RH_{ice} but it is also controlled by temperature. By representing the INAS densities as a function of relative humidity and temperature - see Fig. 4.4 (right) - the INAS trajectories fall much closer together which means that deposition nucleation can be described by the change in x_{therm} as defined by eq. 4.2.

The n_s trajectories as shown in Fig. 4.4 are afflicted with two sources of uncertainty of which the n_s values themselves are the first source. The measurement uncertainty of n_s is determined by the uncertainties $\Delta n_{ice}/n_{ice} \approx 25\%$ and $\Delta A_{aer}/A_{aer} \approx 25\%$ which results in $\Delta n_s/n_s \approx 35\%$. Secondly, the position of each trajectory within the T/RH_{ice} space is affected by the uncertainties ΔT = 0.3 K and ΔRH_{ice} up to 5%. These uncertainties then translate into the uncertainty of the thermodynamic variable x_{therm} with $\Delta x_{therm} \approx 5$. Figure 4.4 shows that the experiments at higher relative humidities over ice (corresponding to warmer temperatures (T_{start} = 250 K)) are characterized by a much larger variety in the slopes of INAS density trajectories than the experiments at lower relative humidities over ice (corresponding to colder temperatures (T_{start} = 235 K)).

4.1.4 Comparison to other parameterizations

In this section, an average INAS density function is derived and compared to the dust-adapted parameterization by Phillips et al. (2008, 2012) and the general parameterization by Meyers et al. (1992). Complementing the INAS density approach, also results from parameterizing the observed ice fractions by classical nucleation theory are presented. Additionally, the time scale that is relevant for deposition nucleation of ATD is determined.

General ice nucleation active surface density approach

Figure 4.4 shows that the n_s values do not diverge by more than one order of magnitude which suggests that the observed INAS density trajectories may be described by an average INAS density function. According to least-square fitting, all measurements can be

described by the fit function $n_s(x_{therm})$

$$n_s(x_{therm}) = 1.88 \cdot 10^5 \cdot \exp(0.2659 \cdot x_{therm}) \quad [\mathrm{m}^{-2}] \tag{4.4}$$

The measurements together with the fit ($r^2 = 0.49$) are depicted in Fig. 4.5.

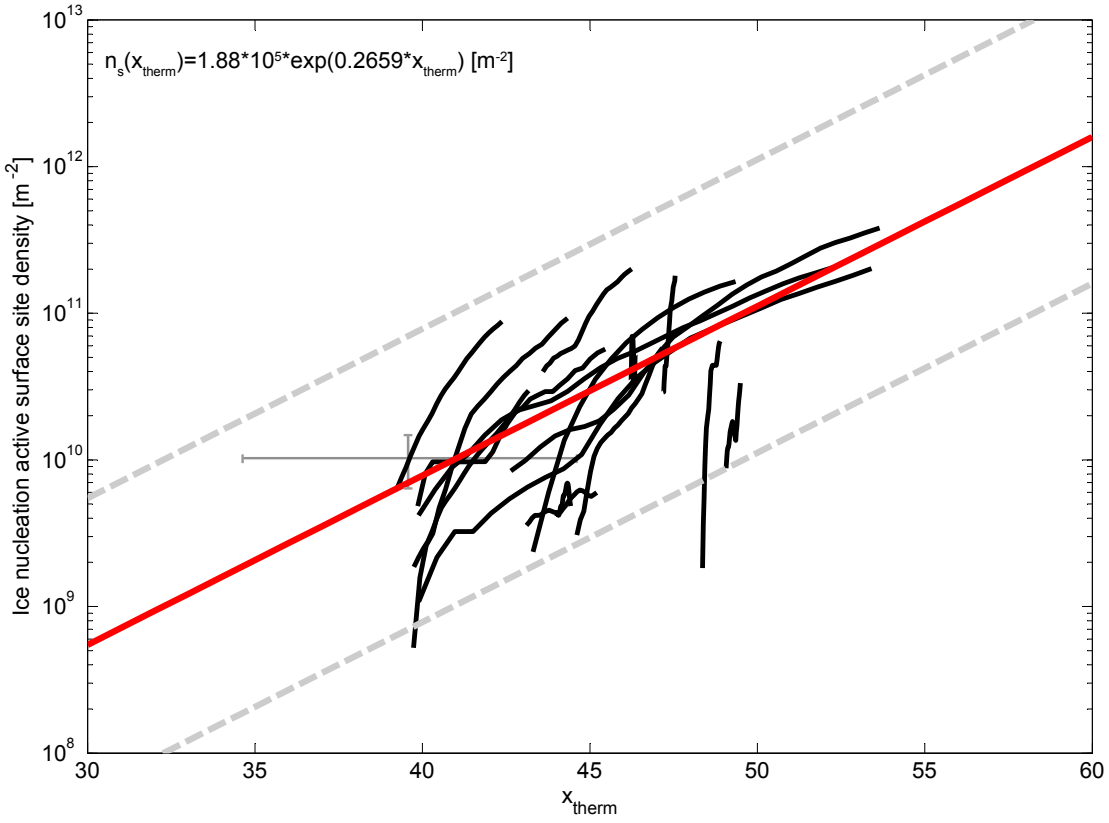

Figure 4.5: *Ice nucleation active surface site densities as in Fig. 4.4 with exponential fit function; grey lines indicate deviations from the fitting function by an order of magnitude*

Figure 4.6 shows all measured n_s values corresponding to the T/RH_{ice} trajectories of each experimental run. Isolines indicate the increase of the fit function $n_s(x_{therm})$ with temperature and relative humidity over ice.

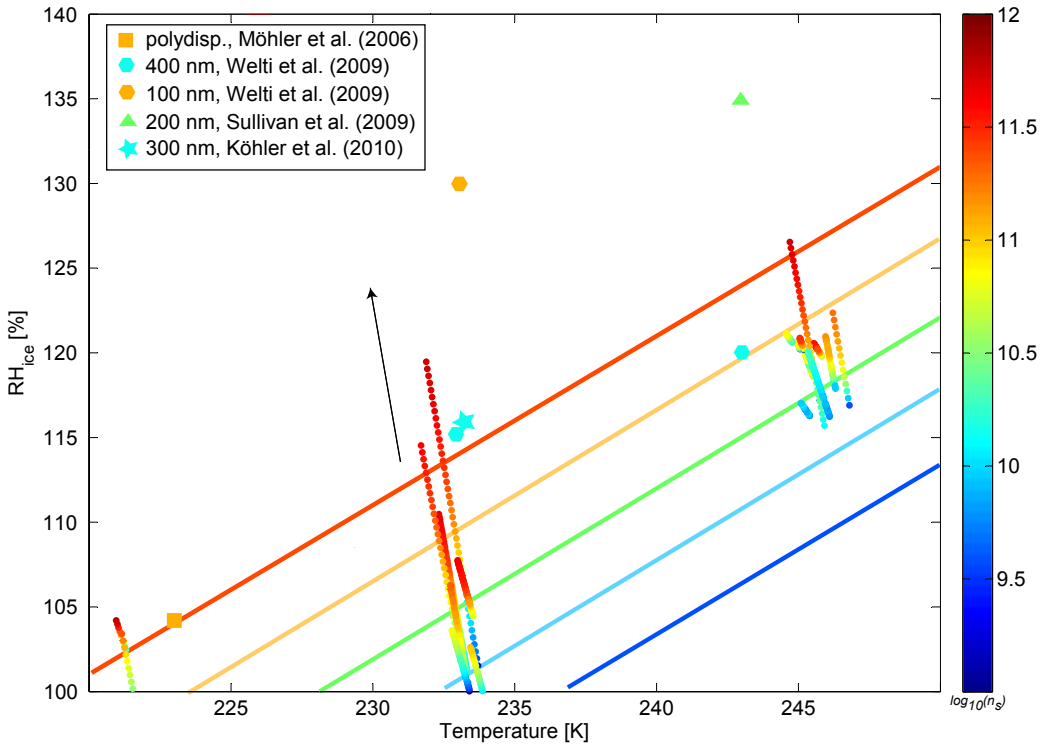

Figure 4.6: *n_s trajectories derived from experimental runs (see Table 4.1) - the arrow indicates decreasing temperature and increasing RH_{ice} during expansion experiments (see Fig. 4.1); colored lines correspond to isolines of the fitted INAS density ($log_{10}(n_s)$) from Fig. 4.5 - symbols indicate ice nucleation active surface site densities derived from experimental studies by other authors*

The comparison with a previous AIDA cloud chamber study by Möhler et al. (2006) shows that the derived INAS density n_s agrees well with our fitted $n_s(x_{therm})$. However, the INAS densities derived from ice fractions observed in studies by Koehler et al. (2010), Sullivan et al. (2010a) and Welti et al. (2009) generally differ by more than one order of magnitude from our fitted $n_s(x_{therm})$. In the study by Koehler et al. (2010) a continuous flow diffusion chamber was used to investigate the ice nucleation properties of ATD particles with selected diameters of 200, 300 or 400 nm. A continuous flow diffusion chamber was also used by Sullivan et al. (2010a) who investigated monodisperse ATD particles (d = 200 nm). Welti et al. (2009) investigated the deposition nucleation properties of size

selected ATD particles with the Zurich Ice Nucleation Chamber (ZINC). In all studies the ATD sample was dry-dispersed by either using a rotating brush generator or a fluidized bed generator. The INAS density values derived from the aforementioned studies are much lower than the INAS densities derived within this experimental study. The differences between our measurements and other experimental studies might be explained differences in the ice nucleation active surface site density values for particles of different sizes.

Comparison to parameterizations proposed by Phillips et al. (2008) and Meyers et al. (1992)

The ice nucleation parameterization developed by Phillips et al. (2008) (updated in Phillips et al. (2012)) is tailored to different aerosol groups such as mineral dust/metallic compounds, soot, organic compounds and primary biological particles.

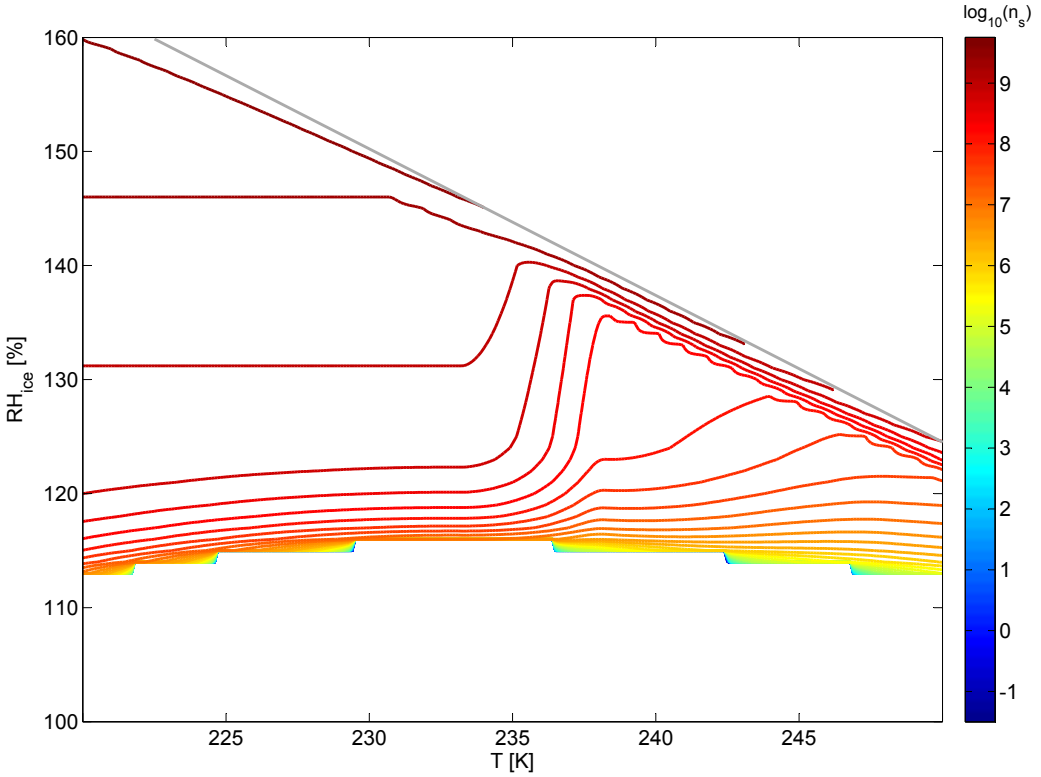

Figure 4.7: *Isolines for the INAS density calculated according to the parameterization by Phillips et al. (2008); the grey line indicates water saturated conditions*

The Phillips parameterization is derived from field campaigns investigating the ice nucleation properties of atmospheric aerosol with a continuous flow diffusion chamber. Figure 4.7 shows isolines with constant INAS density values as predicted for temperatures between 220 and 250 K. The Phillips parameterization (Phillips et al., 2008, 2012) predicts between 232 and 237 K that the INAS isolines bend within the T/RH_{ice} space which would provide a further motivation to construct a temperature and humidity dependent formulation of deposition nucleation at least within this temperature range (see Fig. 4.7). The bending of the n_s isolines between 233 and 248 K was also suggested by Hoose and Möhler (2012) based on a compilation of data from various experimental studies.

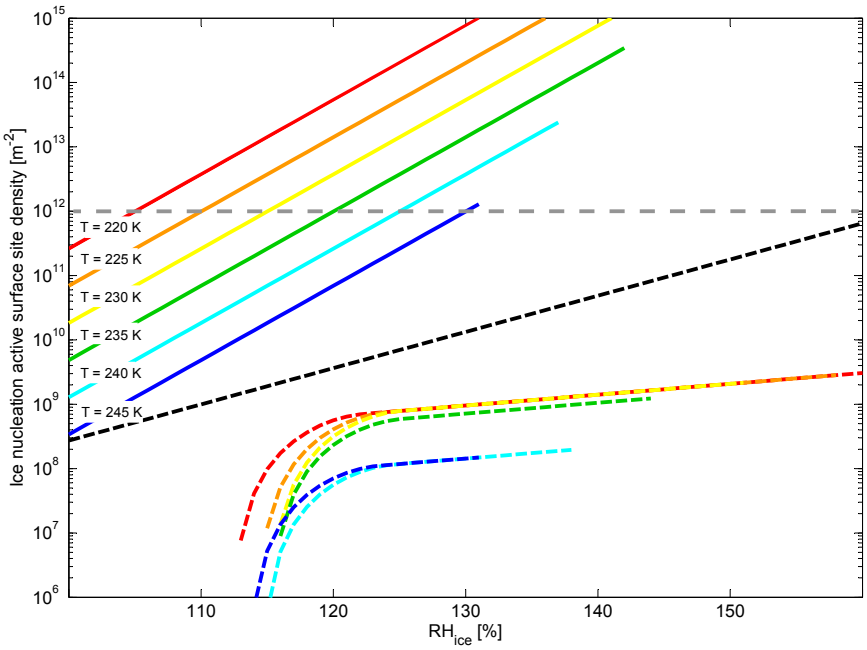

Figure 4.8: *Comparison between INAS densities derived from this work (colored lines), the dust-adapted parameterization by Phillips et al. (2012) (colored dashed lines) and the parameterization by Meyers et al. (1992) (black dashed line); for the Phillips parameterization, colors indicate the same temperatures as for our parameterization - the grey dashed line indicates the experimental limit for n_s values derived from expansion experiments presented in this study*

Figure 4.8 shows a comparison between the INAS density values derived from our experimental parameterization (eq. 4.4), from the ice crystal concentration as parameterized by Phillips et al. (2008, 2012) and from the ice crystal concentration derived by using the purely humidity dependent parameterization proposed by Meyers et al. (1992) with

assuming a generic aerosol surface area density of $A_{aer} = 2 \cdot 10^{-6} \mathrm{m}^2\mathrm{m}^{-3}$ as proposed in Phillips et al. (2012) for background concentrations of tropospheric aerosol. The dashed grey line in Fig. 4.8 indicates the experimental limit of observed ice nucleation active surface site densities in this study ($f_{ice} < 10$ %). The INAS density lines as shown in Fig. 4.8 are also restricted by deposition nucleation only occuring below water saturation.

Our experimental parameterization predicts n_s values which are by several orders of magnitude larger than for the other two parameterizations. Larger deviations between ice crystal predictions based on the Phillips parameterization and based on the INAS density approach were also found in a study investigating the immersion freezing properties of mineral dust particles (Niemand et al., 2012). For immersion freezing, an INAS density parameterization based on cloud chamber experiments with desert dusts was implemented within the regional model COSMO-ART and it was found that for temperatures above 255 K the ice nuclei concentration diagnosed from comparable model runs with the Phillips parameterization differed by several orders of magnitude from the INAS density based calculations (Niemand et al., 2012).

Note, however, that for the comparison between the three approaches in this work not the absolute INAS density values are considered to be most relevant but the slopes of the n_s curves because the absolute values are determined by the assumed aerosol surface area density A_{aer}. The parameterizations by Phillips et al. (2008) and Meyers et al. (1992) predict INAS densities with significantly differently slopes (i.e. dependence on relative humidity over ice) compared to the results from our ATD measurements.

Comparison to classical nucleation theory

Classical nucleation theory can be used to fit results from deposition nucleation experiments with ATD particles. Ice formation requires that stable ice clusters are formed which corresponds to overcoming an energy barrier ΔG_{dep} which separates the metastable water phase from the more stable crystalline ice phase. Classical nucleation theory describes heterogeneous ice nucleation by a form factor $f(m)$ which leads to a reduction of the energy barrier ΔG_{dep}. With a reduced energy barrier, ice formation can occur at tem-

peratures above the homogeneous ice nucleation threshold. The form factor $f(m)$ with $m = \cos(\theta)$ depends on the so-called contact angle θ. The ice fraction observed for an aerosol population can be related to an average contact angle θ depending on the observed ice nucleation efficiency. For aerosol species with several ice nucleation active components such as mineral dusts, a single contact angle is often not sufficient to describe the observed ice fractions (Wheeler and Bertram, 2012). In these cases, a contact angle distribution produces a better agreement between measurements and classical nucleation theory fit (Marcolli et al., 2007; Lüönd et al., 2010; Wheeler and Bertram, 2012).

In this study, the observed ice nucleation efficiency is expressed by a fitted contact angle distribution for each experimental run. The contact angle distribution is determined by an apparent median contact angle μ_θ and an apparent contact angle distribution width σ_θ. These parameters μ_θ and σ_θ can be derived from applying eqs. 2.1, 2.5 and 2.6 to the observed ice fractions (Chen et al., 2008). In this study, the time intervals for which the parameters μ_θ and σ_θ were estimated as best fitting average values varied between Δt=10 s and Δt=30 s. For most experiments, the aerosol size distribution was assumed to be lognormal with the median diameter μ_d = 0.23 µm and the geometric size distribution width σ_d = 1.56. Only for the experiments without cyclone impactors (i.e. larger particle being present) the aerosol size distribution parameters were chosen to be μ_d = 0.35 µm and σ_d = 1.73. Figure 4.9 shows the median contact angles μ_θ and the contact angle distribution widths σ_θ as obtained for each experimental run. In Figure 4.9, additionally the humidity ranges over which the contact angle parameters were obtained are indicated. The uncertainty range of the estimated contact angle parameters was not explicitly quantified. However, the spread of obtained median contact angles suggests that the uncertainties are probably very large. These uncertainties are also rooted in the ambiguities of the classical nucleation theory fit because for some cases contact angle distributions with a significant overlap may produce similar ice fractions.

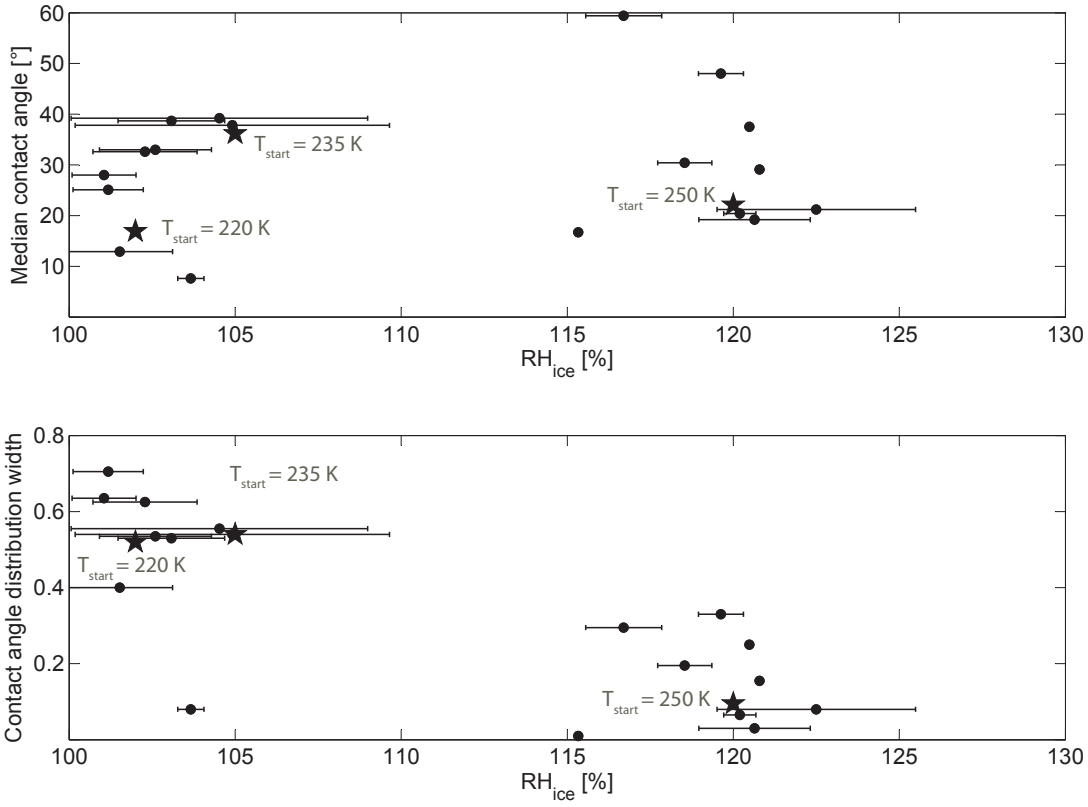

Figure 4.9: *Apparent median contact angle μ_θ and contact angle distribution width σ_θ as inferred from classical nucleation theory with • indicating values obtained for individual experiments and ⋆ indicating the average values; indicated is also the humidity interval for which the apparent median contact angle was estimated*

For the experiments starting at T_{start} = 250 K, the median contact angles μ_θ vary between 18° and 40° (excluding two outliers), whereas for experimental runs starting at T_{start} = 235 K or T_{start} =220 K, the median contact angles μ_θ were found to scatter between 25° and 40° resp. between 8° and 13°. It cannot be excluded that the observed ice nucleation efficiencies might be better described by a bi-modal contact angle distribution representing two distinct types of ice nucleation sites. This hypothesis is motivated by finding a weaker agreement between measured and fitted ice fractions for median contact angles around 80°. However, in this study only a unimodal distribution was considered for fitting the observed ice fractions.

For high temperature deposition nucleation (T_{start} = 250 K) the contact angle distribu-

tion parameters which best described all experimental runs (r^2 = 0.48) were μ_θ = 22.1° and σ_θ = 0.095. For deposition nucleation at lower temperatures, the contact angle parameters were found to be μ_θ = 36.2° and σ_θ = 0.520 (r^2 = 0.52) for experiments at T_{start} = 235 K and μ_θ = 16.9° and σ_θ = 0.540 (r^2 = 0.89) at T_{start} = 220 K.

Thus, the best fit values for the apparent median contact angle μ_θ increase with higher supercooling and then decrease again which is seemingly counter-intuitive. However, this behaviour is probably related to the large uncertainties involved in the measurements and the fitting procedure. Note, however, that increasing median contact angles with lower temperature were also observed during immersion freezing studies investigating the ice nucleation properties of kaolinite (Welti et al., 2012). The median contact angle increasing with greater supercooling was interpreted as the surface features (i.e. ice nucleation properties) of individual dust particle becoming less relevant at lower temperatures. Similarly as the median contact angles, the contact angle distribution widths vary considerably between experimental runs and tend to be much larger at low temperatures and low relative humidities. The contact distribution widths also increase for higher supercooling. From the experiments presented in the previous paragraphs it can be concluded that using classical nucleation theory to describe the deposition nucleation efficiency of mineral dust particles or other aerosol species requires a large number of experiments investigating combinations of different cooling rates, aerosol size distributions and thermodynamic regimes (i.e. temperature and relative humidity) to derive the contact angle distribution parameters in relation to these various conditions.

Deriving apparent INAS density values from classical nucleation theory

As an example for bringing together classical nucleation theory formulations and the INAS density approach, in the following paragraphs apparent INAS densities as derived for two different contact angle distributions are presented. The prescribed temperature and humidity changes represent conditions which resemble AIDA cloud chamber experiments.

Figure 4.10 shows a temperature ramp corresponding to a cooling rate of $r \approx 2.5$ K/min (Fig. 4.10a) and a change in relative humidity over ice which is assumed to be comparable to the expected change observed in AIDA cloud chamber experiments (Fig. 4.10b). Calculations were performed for time steps of Δt = 1 s.

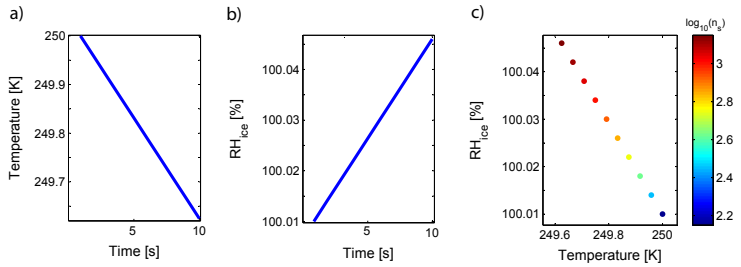

Figure 4.10: *INAS density values calculated from classical nucleation theory for a temperature ramp (a) representing a cooling rate of $r = 2.5$ K/min and simultaneous change in the relative humidity (b) comparable to AIDA cloud chamber experiments*

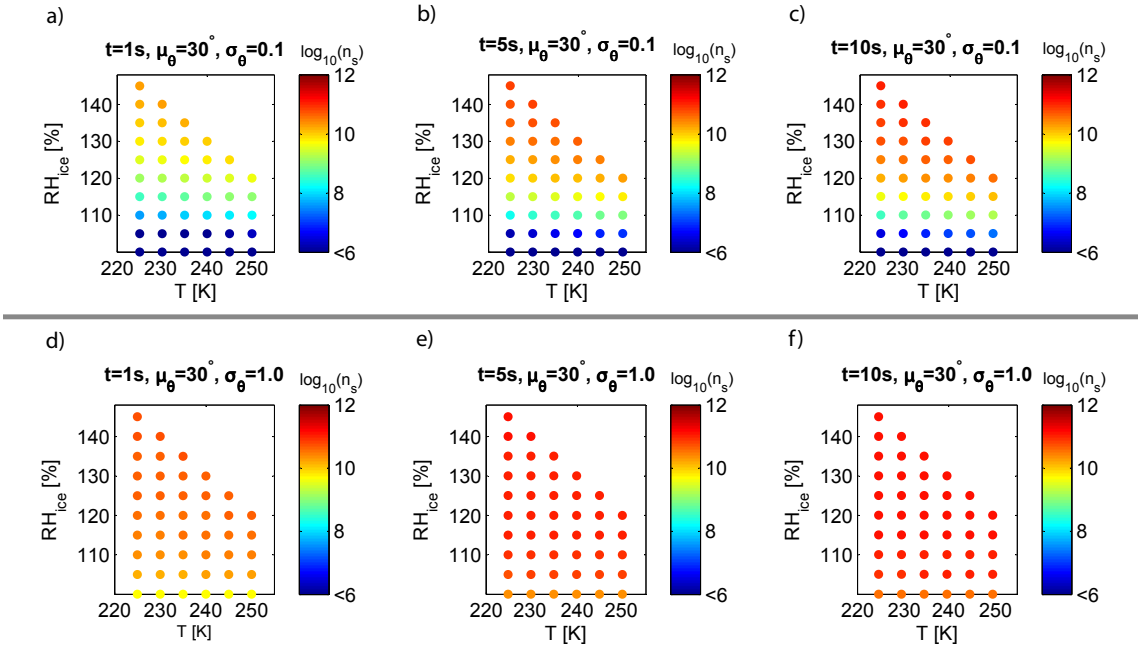

Figure 4.11: *INAS density values as derived from classical nucleation theory for a narrow contact angle distribution with $\mu_\theta = 30°$ and $\sigma_\theta = 0.1$ (a-c) and a broader contact angle distribution with $\mu_\theta = 30°$ and $\sigma_\theta = 1.0$ (d-f); the INAS density values are depicted for three different time steps, i.e. after 1 s (a,d), after 5 s (b,e) and after 10 s (c,f)*

For these conditions, the ice fraction predicted by classical nucleation theory for deposition nucleation was calculated according to Chen et al. (2008) while assuming a contact angle distribution with μ_θ = 30° and σ_θ = 0.1. From the calculated ice fraction, the corresponding INAS density values were calculated under the assumption of an average per-particle-surface of A_p = 0.13 µm^2 corresponding to a particle diameter of d_p = 0.2 µm. The temperature decreases from 250.0 to 249.6 K, whereas the relative humidity over ice increases from 100.01% to 100.05% within the simulated time period of $\Delta t_{tot} = 10s$ (Fig. 4.10a and b). The INAS density values for deposition nucleation at 250 K and humidities slightly above ice supersaturation are very small and range from 10^2 to 10^3 m^{-2}. The same calculations as presented in Fig. 4.10 were repeated for a range of initial temperature and humidity conditions.

The INAS density values depicted in Fig. 4.11 are derived from classical nucleation theory according to Chen et al. (2008) as described for Fig. 4.10. The thermodynamic starting conditions were varied between 225 and 250 K and relative humidity between RH_{ice} = 100% and RH_{ice} = 145%. Each gridpoint in the subfigures of Fig. 4.11 corresponds to a simulated temperature and humidity ramp. The INAS density values shown in Fig. 4.11 were calculated for a narrow contact angle distribution (μ_θ = 30° and σ_θ = 0.1) and a broader contact angle distribution (μ_θ = 30° and σ_θ = 1.0). The broader contact angle distribution includes contributions from very efficient ice nuclei (i.e. small contact angles) which are, however, very rare. Also, Fig. 4.11 shows how the apparent INAS density values develop over time.

Fig. 4.11a shows INAS density values predicted for the narrow contact angle distribution after Δt = 1 s. The INAS density values increase with higher relative humidities over ice at a constant temperature. At constant relative humidity, the INAS density values either stay constant or decrease slightly with higher supercooling. Note that only INAS density values below water saturation are depicted because only deposition nucleation is considered. The INAS density values vary between 10^2 (see Fig. 4.10) and 10^{10} m^{-2}. For the following time steps Δt = 5 s (Fig. 4.11b) and Δt = 10 s (Fig. 4.11c), the general trend of the INAS density values with temperature and relative humidity persists. The

predicted INAS density increase to approximately 10^{11} m^{-2} at high relative humidity over ice.

In Fig. 4.11d the relation between INAS densities and the thermodynamic conditions (i.e. temperature and relative humidity over ice) is depicted for a broader contact angle distribution with $\mu_\theta = 30°$ and $\sigma_\theta = 1.0$. The predicted INAS densities vary between $7 \cdot 10^9$ m^{-2} and $5 \cdot 10^{10}$ m^{-2}. Especially at low supersaturations, the difference to the INAS density values for the narrow contact angle distribution becomes evident. At low relative humidities, the INAS densities predicted for the broader contact angle distribution are by several orders of magnitude higher than for the narrow contact angle distribution. The INAS density values increase with relative humidity over ice as observed for the narrow contact angle distribution, but for the broader contact angle distribution the change in INAS densities with temperature is even weaker. After Δt = 10 s, the INAS densities increase to values up to 10^{11} m^{-2}. Note that this limit is not only determined by the contact angle distribution parameters and the prescribed thermodynamic conditions but also by the aerosol surface which is used to calculate the INAS density values.

From Fig. 4.11 it can be concluded that the apparent INAS densities are mostly influenced by the relative humidity over ice. The impact of changes in temperature is only weak. Especially at relative humidities slightly above ice supersaturation, the predicted INAS densities are sensitive to the contact angle distribution width and considerably higher for broader contact angle distributions. For developing classical nucleation theory based parameterizations from observations, the contact angle distribution width must be thoroughly characterized for a wide range of temperature and relative humidity conditions. The observed increase of deposition INAS density values with higher supercoolings could not be reproduced with classical nucleation theory.

4.1.5 Time dependence of deposition nucleation and extension of the INAS density approach

Ice nucleation active surface site densities - per definition - depend only on temperature and relative humidity over ice. However, as ice nucleation is a stochastic process it can be assumed that the INAS densities derived from experimental data include an implicit time dependence. Thus, for isothermal experiments, the observed n_s values would increase over time. For quantifying the time dependence of deposition nucleation two different approaches are used.

Time dependent ice nucleation may be described by

$$n_s = \tilde{n}_s + a_3 \cdot t \tag{4.5}$$

$$= a_1 \cdot \exp(a_2 \cdot x_{therm}) + a_3 \cdot t \ [\mathrm{m}^{-2}] \tag{4.6}$$

where x_{therm} is defined by eq. 4.2 and t [s] is the time starting from the first observation of ice crystals, neglecting ice formation below the detection limit. For deriving the coefficients in eq. 4.6 only the first 20 s after ice formation was observed are considered for which the ice fractions were smaller than $f_{ice} < 10\%$. The first part of eq. 4.6 expressed as $\tilde{n_s}$ describes the formation of ice crystals caused by the "best" ice nuclei among the dust particles. Upon reaching certain thermodynamic thresholds (i.e. x_{therm} values) these particles initiate ice nucleation immediately within the temporal resolution of our experimental setup. The linear source term then describes the formation of ice by the less efficient ice nuclei components which are only activated after a certain period of time. The coefficients in eq. 4.6 are determined from least-square fitting as $a_1 = 1.9 \cdot 10^3$ [m^{-2}], $a_2 = 0.363$ and $a_3 = 3.7 \cdot 10^6$ [$\mathrm{m}^{-2}\mathrm{s}^{-1}$] ($r^2 = 0.74$).

The other time dependence approach assumes that the measured INAS densities converge towards a certain ice nucleation active surface site density $\tilde{n}_s(x_{therm})$ at a constant x_{therm} value after very long periods of time. Time dependence is then described by

$$n_s = \tilde{n}_s \cdot (1 - \exp(-b_3 \cdot t)) \tag{4.7}$$

$$= b_1 \cdot \exp(b_2 \cdot x_{therm}) \cdot (1 - \exp(-b_3 \cdot t))[\mathrm{m}^{-2}] \tag{4.8}$$

The coefficients in eq. 4.8 are determined as $b_1 = 8.1 \cdot 10^5$ [m^{-2}], $b_2 = 0.254$ and $b_3 = 0.065$ [s^{-1}] ($r^2 = 0.70$).

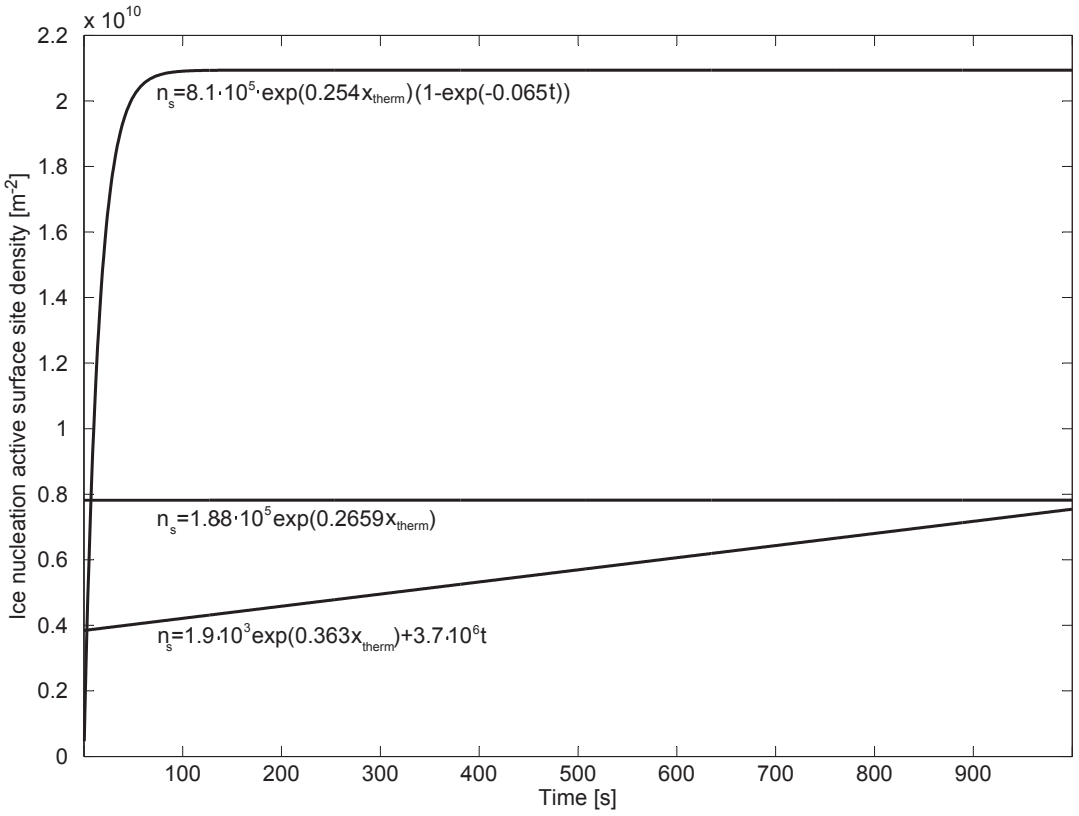

Figure 4.12: *Ice nucleation active surface site densities over time as predicted by eqs. 4.4, 4.6 and 4.8 for* x_{therm} = 40

Figure 4.12 shows how the ice nucleation active surface site densities as described by eqs. 4.6 and 4.8 evolve over time. The thermodynamic variable x_{therm} is assumed to have a constant value x_{therm} = 40. For comparison, also the n_s value predicted by the parameterization without time dependence is shown. For the time dependence as described by eq. 4.6 the predicted ice nucleation active surface site density is initially smaller than the value obtained from eq. 4.4 but gradually converges towards the INAS density obtained from the time independent parameterization. This behaviour describes that at first only the most ice active nucleation sites initiate the formation of ice wheras the more inefficient sites require a certain amount of time to become active. Equation. 4.8 predicts a steep increase of the ice nucleation active surface site densities, followed by a convergence towards a constant value. This constant value corresponds to a state at a constant value of x_{therm} where most of the ice active surface sites have become active with only very few inefficient sites not being involved in the formation of ice. It is assumed

that these inefficient ice nucleation sites would only activate at time scales longer than relevant for atmospheric ice nucleation processes.
Both time dependence approaches fit the measurements reasonably well and thus both descriptions might be used for the description of time dependent deposition nucleation. Note, however, that eq. 4.6 and eq. 4.8 need to be viewed as very simplistic approaches. Nevertheless, these equations could be used to evaluate the time dependence of ice nucleation initiated by other particle species.

Relevance of the time dependent source term

The box model ACPIM (aerosol-cloud precipitation interaction model) which was developed at the University of Manchester (Connolly et al., 2009) was used to calculate the ice formation within an ascending air parcel with a prescribed ice nucleation parameterization. The ice nucleation parameterizations as described by eqs. 4.4, 4.6 and 4.8 were analyzed for different updraft velocities and aerosol parameters as described in Table 4.2. Each parcel run is initialized at cirrus cloud conditions with $T = 235$ K, $p = 550$ mbar and $RH_{wat} = 68\%$. The parcel is then allowed to develop for $\Delta t = 600$ s resp. for $\Delta t = 1200$.

Table 4.2: Overview of cloud dynamics and aerosol property parameters as used for the ACPIM runs

Aerosol concentration [cm^{-3}]	1	100	
Aerosol particle median diameter [µm]	0.2	0.4	
Updraft velocity w [m/s]	0.05	0.5	5.0

The aerosol concentration is varied between between 1 and 100 cm^{-3} to transfer the experimentally derived INAS densities into a context with atmospherically relevant aerosol concentrations. The contribution of larger particles is investigated by shifting the median diameter of the aerosol size distribution from 0.2 µm to 0.4 µm. The updraft velocities of the simulated air parcels are varied to allow for attributing the ice crystal concentration not only to changes in the aerosol properties, but also to variations in cloud dynamics.

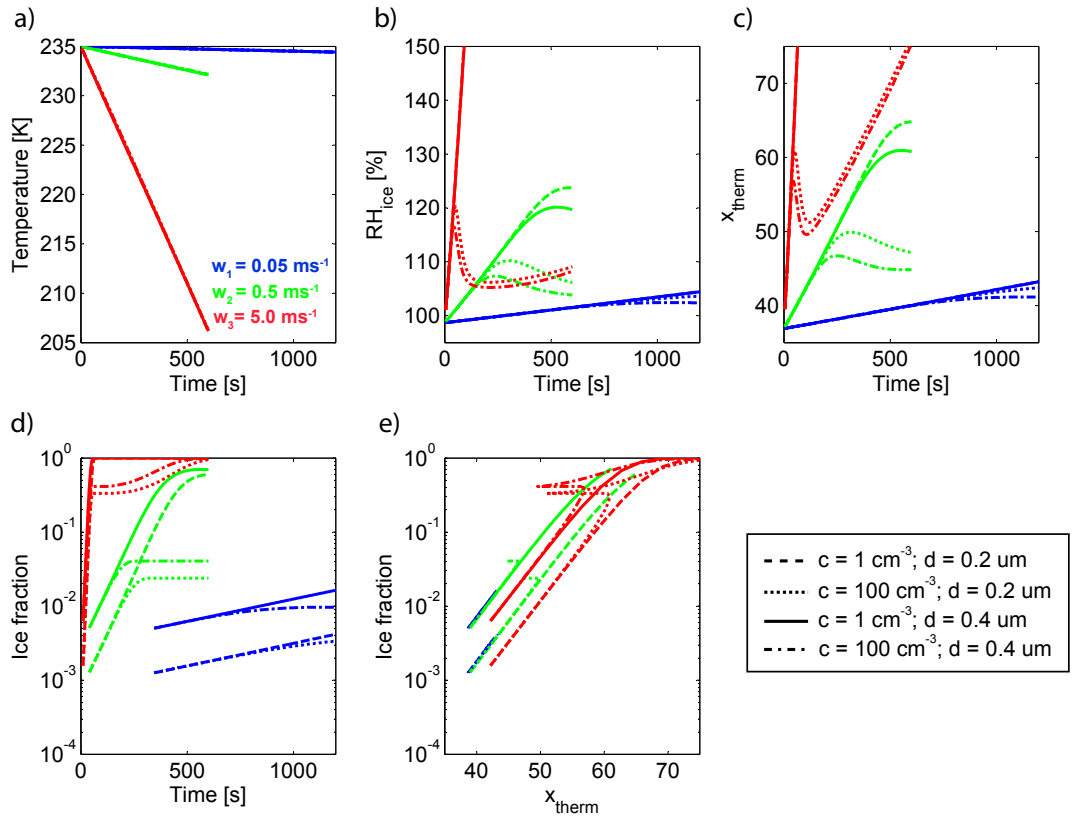

Figure 4.13: *Time series for calculations with the box model ACPIM: parcel runs with varying updraft velocities (indicated by color) for investigating the influence of aerosol concentration and the aerosol median diameter on the observed ice active fractions; all runs start at T=235 K and S_{wat}=0.68 - ice nucleation is parameterized by eq. 4.4*

Figure 4.13 shows the decrease in temperature (Fig. 4.13a), the development of relative humidity over ice (Fig. 4.13b), and the change in the thermodynamic variable x_{therm} as defined in eq. 4.2 (Fig. 4.13c). The observed ice fractions at different updraft velocities are depicted as a function of time (Fig. 4.13d) and as a function of the thermodynamic variable x_{therm} (Fig. 4.13e). For each updraft velocity value the trajectories are calculated for all aerosol parameters as described in Table 4.2. For the trajectories shown in Fig. 4.13, ice nucleation is assumed to be independent of time.

- For the lowest updraft velocity ($w_1 = 0.05$ m s^{-1}), the reduction in temperature is less than 1 K over the whole simulated time period. Likewise, the increase in relative humidity over ice is less than 5%. Thus, only a small supersaturation is reached.

The thermodynamic variable x_{therm} increases from x_{therm} = 37 to x_{therm} = 42. After Δt = 1200 s, the observed ice fractions remain below 2%.

- For intermediate updraft velocities (w_2 = 0.5 m s^{-1}), the parcels are cooled to 232 K and reach peak relative humidity values of RH_{ice} = 110% at high aerosol concentrations and RH_{ice} = 120% at low aerosol concentrations. The increase in x_{therm} is strongly driven by the increase in relative humidity and thus x_{therm} can reach peak values of x_{therm} = 47 and x_{therm} = 65. The observed ice fractions are strongly influenced by the prevalent aerosol concentrations and vary between 2 and 70%.

- At very large updraft velocities (w_3 = 5.0 m s^{-1}), temperatures as low as 206 K are reached within 600 s. However, the determining factor for these simulations is the peak relative humidity which is related to the prescribed aerosol concentration. At low aerosol concentrations, all aerosol particles are activated within less than 100 s. After ice activation is completed, relative humidity increases further to values larger than RH_{ice} = 200%. For high aerosol concentrations, the conversion of all aerosol particles into ice crystals is only achieved at the end of the parcel run whereas the peak relative humidity (RH_{ice} = 120%) is already reached within the first 100 s of the simulation.

Figure 4.14 shows simulations similar to those depicted in Fig. 4.13. However, for the simulations presented in Fig. 4.14 ice nucleation was assumed to be time dependent according to eqs. 4.6 and 4.8. Note that the temperature and relative humidity trajectories are very similar to the runs without time dependent ice nucleation (not shown). Likewise, the evolution of x_{therm} is similar.

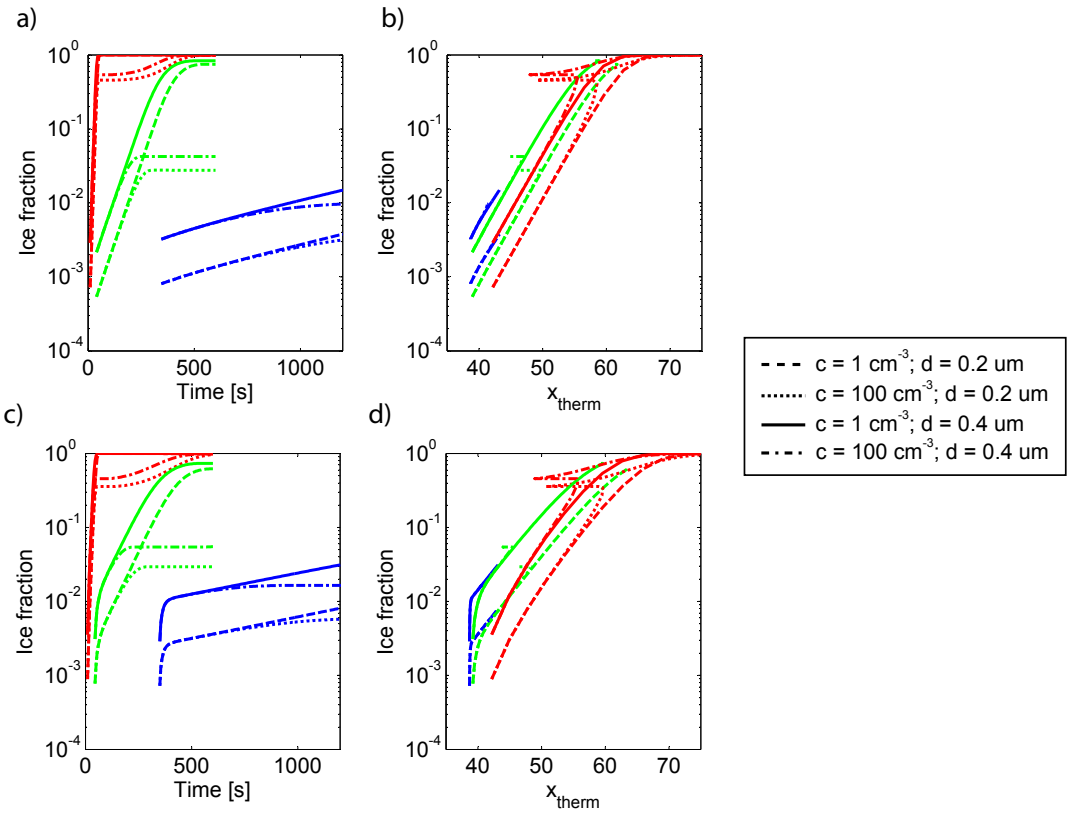

Figure 4.14: *Time series for calculations with the box model ACPIM: parcel runs with varying updraft velocities (indicated by color) for investigating the influence of aerosol concentration and the aerosol median diameter on the observed ice active fractions; all runs start at T=235 K and S_{wat}=0.68 - for the subfigures a) and b) ice nucleation is parameterized by eq. 4.6, whereas for c) and d) eq. 4.8 was used*

Comparing the predicted ice fractions at the end of the updraft periods, the first time dependent ice nucleation parameterization (eq. 4.6) does not produce results deviating much from those based on eq. 4.4. Only the initial increase of the observed ice fractions is steeper than for purely humidity and temperature dependent ice formation. The sec-

ond time dependent ice nucleation parameterization (eq. 4.8) generally predicts ice active fractions being higher than the purely x_{therm} dependent parameterization by a factor of 2 which is largely due to the coefficient b_1. Note that the time dependent ice nucleation parameterization described by eq. 4.8 predicts rapid ice nucleation at low ice-active fractions. The measurements shown in Fig. 4.4 at least partially corroborate this result.

From this simple case study it can be concluded that the importance of time dependence for deposition nucleation initiated by ATD particles is generally small and only relevant at low to moderate updraft velocities and small ice fractions.

4.1.6 Application of the INAS density approach to the deposition nucleation by natural dusts

The results from the deposition nucleation experiments with ATD suggest that deposition nucleation at temperatures warmer than 220 K can be best described by a temperature and humidity dependent ice nucleation active surface site density approach.

Table 4.3: Overview of selected deposition nucleation experiments with mineral dusts and clay minerals conducted at the AIDA cloud chamber

Reference	Material	Temperature range [K]
Cziczo et al. (2009)	Illite	238 – 243
Möhler et al. (2006)	Saharan Dust, Asian Dust	208 – 224
This work	Saharan Dust	220 – 243

Figure 4.15 shows the ice nucleation efficiencies of Saharan Dust (SD2), illite (Cziczo et al., 2009) and Asian Dust (Möhler et al., 2006) expressed as ice nucleation active surface site densities.

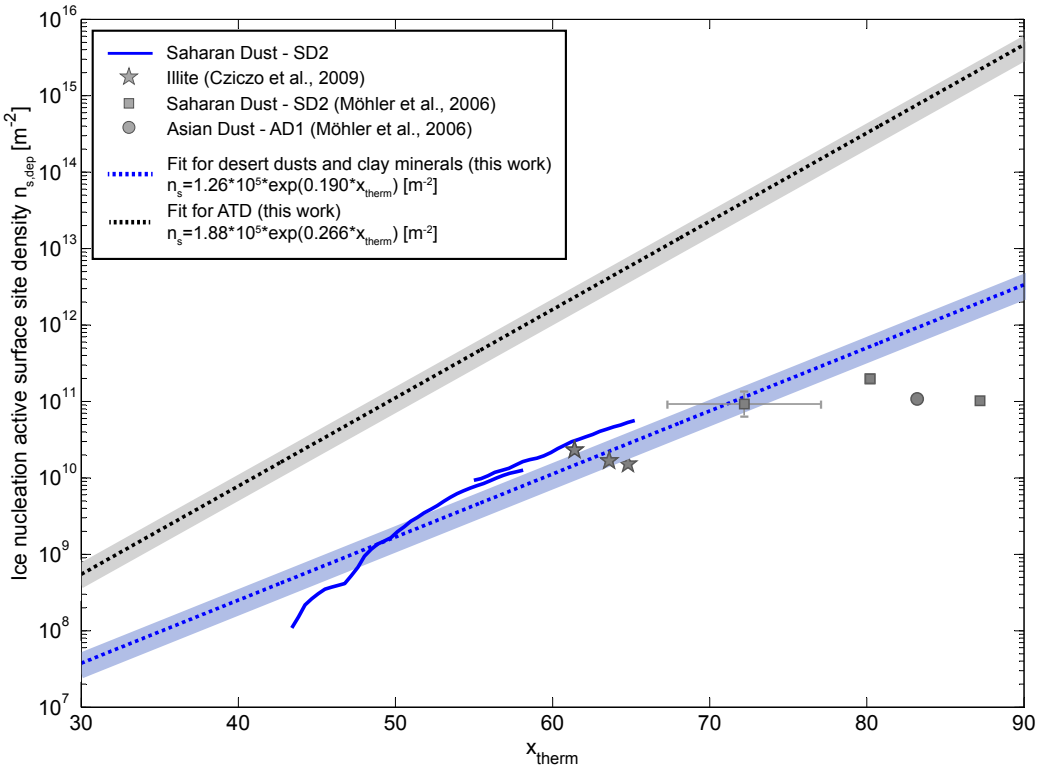

Figure 4.15: *Deposition nucleation efficiency for unprocessed mineral dusts and clay minerals quantified by the ice nucleation active surface site densities - INAS densities are shown as a function of x_{therm}; shading indicates the measurement uncertainties*

These measurements have been fitted with an exponential function

$$n_{s,dep}(x_{therm}) = 1.26 \cdot 10^5 \cdot \exp(0.190 \cdot x_{therm}) \ [\mathrm{m}^{-2}] \tag{4.9}$$

which depends on the thermodynamic variable x_{therm} as defined by eq. 4.2. From Fig. 4.15 it can be inferred that eq. 4.9 fits the measurements especially well in the range between $x_{therm} = 40$ and $x_{therm} = 70$. The measurements at large values of $x_{therm} \approx 80$ correspond to deposition nucleation observed at temperatures lower than 210 K where the validity of the x_{therm} approach as given by eq. 4.2 is slightly questionable because experimental studies (Hoose and Möhler, 2012) and the Phillips parameterization (Phillips et al., 2008) suggest that the form of the INAS density isolines should be described by a different relation than eq. 4.2. Figure 4.15 also demonstrates that the deposition nucleation efficiency of Arizona Test Dust is higher than the ice nucleation efficiency inferred for unprocessed

natural dusts and clay minerals. It should be noted, however, that even for the deposition nucleation efficiency of ATD an investigation of the ice nucleation behaviour close to water saturation at temperatures above 235 K is needed to find an even more adequate formulation than the linear approximation for x_{therm}. The deposition nucleation properties of ATD have been investigated at least for the temperature range between 220 and 250 K but more deposition nucleation measurements with mineral dusts for which the aerosol surface area is available are needed for developing a reliable prediction of the ice crystal number concentration contributed by dust deposition nucleation. Also, the time dependence of deposition nucleation initiated by desert dusts and clay mineral should be investigated.

4.1.7 Summary

From cloud chamber experiments with Arizona Test Dust, deposition nucleation at temperatures warmer than 220 K has been identified as a process which is not only controlled by relative humidity over ice, but also partly by temperature. Thus, ice nucleation parameterizations should consider the temperature dependence of deposition nucleation at higher temperatures.

Cloud chamber experiments with ATD were also used to investigate the time dependence of deposition nucleation. For inferring the time dependence, the ice nucleation efficiencies expressed as ice nucleation active surface site densities were compared among experimental runs with different cooling rates. The potential impact of the time dependent contribution was investigated by using numerical calculations with a box model (ACPIM, University of Manchester) simulating the ascent of cloud parcels. It was found that the time dependent terms are mostly relevant at cooling rates below 0.5 ms^{-1}.

The ice nucleation efficiency of ATD was expressed by an exponential INAS density function with

$$n_{s,dep}(x_{therm}) = 1.88 \cdot 10^5 \cdot \exp(0.266 \cdot x_{therm}) \ [m^{-2}] \qquad (4.10)$$

where x_{therm} depends linearly on temperature and relative humidity.

Likewise, the deposition nucleation efficiency of mineral dusts and clay mineral was expressed as

$$n_{s,dep}(x_{therm}) = 1.26 \cdot 10^5 \cdot \exp(0.190 \cdot x_{therm}) \ [\mathrm{m}^{-2}] \tag{4.11}$$

These parameterizations should only be applied for temperatures between 220 and 250 K.

4.2 Diatomite

The AIDA cloud chamber was also used to investigate the ice nucleation properties of other mineral dust samples such as fossil diatomite. Diatoms are microalgae which consist of single cells enclosed within a silica shell. As living organisms these microalgae are mainly emitted over the oceans by bubble-bursting and wave-breaking processes (Cipriano and Blanchard, 1981). Additionally, from paleolakes and former fluvial regions fossil diatomite is lofted into the lower and upper troposphere (Harper and McKay, 2010). One of the most active regions with regard to the emission of fossil diatomite is the Bodélé sink in Northern Africa (Todd et al., 2007; Warren et al., 2007). Several thousand years ago the lake MegaChad was one the largest lakes in this region, but it dried out and left large deposits of diatomite behind. The emission of diatoms and fragments benefits from the coincidence of strong surface winds, the landscape structure consisting of turbulence inducing dunes and finally the presence of large diatomite flakes which are easily lofted into the air where they collide and fall apart releasing smaller particles (Warren et al., 2007). Close to the source region two size modes are found for atmospheric diatoms - a coarse mode centered at approximately 1 µm and a fine mode at 0.5 µm. Silicon-rich particles (presumably fossil diatoms) over Niger were mostly larger than 0.4 µm (Chou et al., 2008). Dust plumes containing diatoms may travel as far as to the equatorial North Atlantic and even Antartica (Harper and McKay, 2010). The Bodélé sink contributes between 6 and 18% to the global dust burden (Todd et al., 2007).

Dust plumes emitted from the Saharan region carry fossil diatoms and provide a substantial number of ice nuclei impacting the structure of clouds. Field measurements have found ice nuclei concentrations up to 300 l^{-1} (at 255 K) for Saharan dust events in Europe (Klein et al., 2010). Note that even though these ice nuclei were mainly silicates and carbonates a contribution by co-transported biological particles or from regional ice nuclei sources could not be excluded. Also, the ice nucleation properties of fossil diatoms were not known.

4.2.1 Ice nucleation properties of fossil diatomite

The ice nucleation properties of commercially available fossil diatom particles (Agrinova) were investigated for immersion freezing and deposition nucleation.

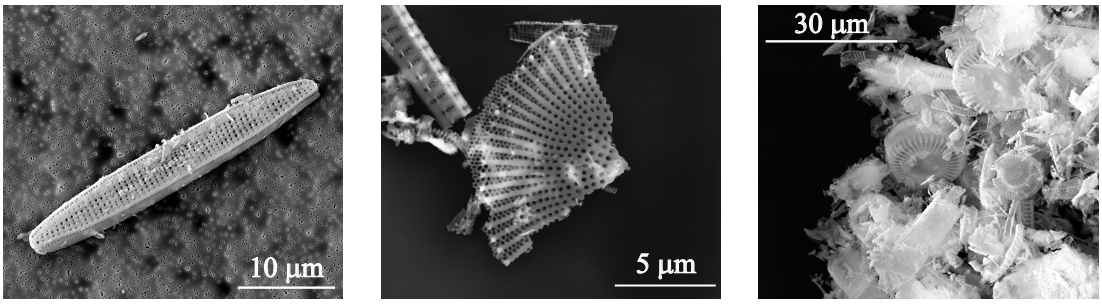

Figure 4.16: *Microscope images of a fossil diatom particle (left), a diatom fragment (middle) and an overview of the bulk sample (right) - images: courtesy of A. Kiselev*

Figure 4.16 shows an intact diatomite particle, a fragment of a circular fossil microalga and an overview of the bulk sample. A large part of the sample consists of small ($d \approx 1$ µm) diatom fragments.

The experiments which are discussed in this section are listed in Table 4.4.

Table 4.4: Overview of AIDA cloud chamber experiments with fossil diatomite

Experiment	Initial temperature [K]	Aerosol concentration [cm^{-3}]	Median diameter [µm]	Ice nucleation mode
IN15_59	262	241	0.33	Imm. freezing
IN15_42	243	395	0.30	Dep. nucleation
IN15_44	233	281	0.31	Dep. nucleation
IN15_46	223	367	0.36	Dep. nucleation
IN16_12	244	305	0.29	Dep. nucleation

The ice nucleation efficiency is quantified by the ice nucleation active surface site densities with $n_s = n_{ice}/A_{aer}$ for immersion freezing and deposition nucleation. The ice crystal concentration is measured with an uncertainty $\Delta n_{ice}/n_{ice} \approx 25$ %. For desert dust particles the measurement uncertainty of the aerosol surface area is given by $\Delta A_{aer}/A_{aer} \approx 25$ %. Note, however, that the fossil diatom particles are even more aspherical than desert dust particles. Also, diatomite particles are characterized by a large number of micropores and

other surface features as shown in Fig. 4.16. Thus, the diatom surface area determined by using the volume equivalent diameters as measured with APS and SMPS will probably deviate more strongly from the actual surface area as for the desert dust particles.

Therefore, the BET surface areas for fossil diatomite and ATD were measured in order to provide upper limits for the underestimation of the aerosol surface area[1]. The BET surface for diatoms is 43 m^2/g, whereas for ATD this value is lower with 12 m^2/g. The mass density within the AIDA chamber was not explicitly measured, and therefore only estimates can be made with regard to the BET surface area of the aerosol population within the AIDA chamber. It should also be noted that the BET analysis was conducted for the bulk aerosol whereas for the AIDA cloud chamber experiments in most cases a cyclon impactor was used to eliminate larger aerosol particles. Therefore, only rough estimates can be made.

The BET surface of a single ATD particle can be estimated by assuming that the dust particles are massive spheres with a diameter of d = 0.23 µm and a bulk density of ρ_{ATD} = 2.6 g/cm^3. With these values, the mass and the BET-based aerosol surface area can be estimated as $A_{aer,BET}$ = 0.20 μm^2 for a single ATD particle.

Similarly, for single diatom particles the aerosol surface area can estimated. In Fig. 4.16 (left) a cylindrical diatomite particle is shown with a length of l = 20 µm and a diameter of d = 2 µm. The cylindric particle is assumed to be hollow and to have an average wall thickness of about 0.01 µm. With a bulk density comparable to mineral dust ρ_{Dia} = 2.6 g/cm^3, the BET-based aerosol surface can be estimated as $A_{aer,BET}$ = 137 μm^2. The particle depicted in Fig. 4.16 (middle) can be approximated as the quarter of a disk with a radius r = 6 µm and a thickness of 0.01 µm. With these dimensions the aerosol surface is estimated as $A_{aer,BET}$ = 124 μm^2.

From these order-of-magnitude estimates it can be concluded that the aerosol surface area of a diatom is potentially much larger than the surface area of an ATD particle. Note, however, that the actual densities of ATD particles and fossil diatoms might differ from the standard values assumed for mineral dust. Also, the aerosol particles within the AIDA chamber are not monodisperse. Additionally, the morphology of the diatom particles differs from that of mineral particles, especially with regard to the occurence of

[1] BET measurements were conducted by T. Kisely (INE, Karlsruhe Institute of Technology)

pores which might encourage the formation of ice. The potential influence of morphology will be discussed at the end of this chapter when the results of the cold stage studies are presented.

Immersion freezing initiated by fossil diatomite

Figure 4.17 shows the ice nucleation active surface site density for diatomite over a comparatively narrow temperature range between 254 and 257 K. For comparison, also the INAS densities for desert dusts are shown (Niemand et al., 2012).

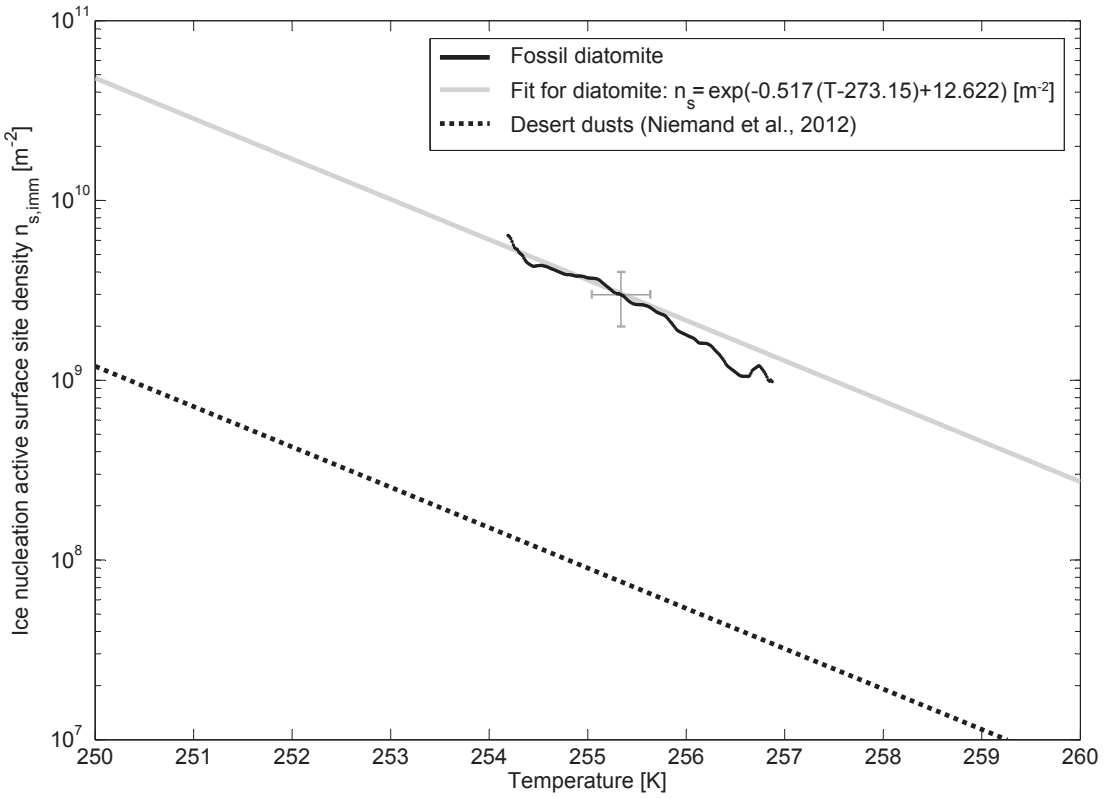

Figure 4.17: *Ice nucleation active surface site density for immersion freezing initiated by fossil diatomite particles compared to the ice nucleation efficiency of desert dusts*

Diatomite is a very active immersion freezing ice nucleus compared to desert dusts with the temperature dependent INAS density $n_{s,imm}$ being described by

$$n_{s,imm} = exp(-0.517 \cdot (T - 273.15) + 12.622) \ [\mathrm{m}^{-2}] \qquad (4.12)$$

where T is the temperature given in [K]. Note that fossil diatoms consist of highly condensed amorphous silicate whereas mineral dusts consist of several mineral components (Gendron-Badou et al., 2003; Broadley et al., 2012). Thus, not only the morphology of fossil diatoms is very different from desert dusts but also the chemical composition.

Deposition nucleation initiated by fossil diatomite

Below 253 K, fossil diatoms initiate deposition nucleation. The INAS density values as they increase with supercooling and relative humidity are shown in Fig. 4.18.

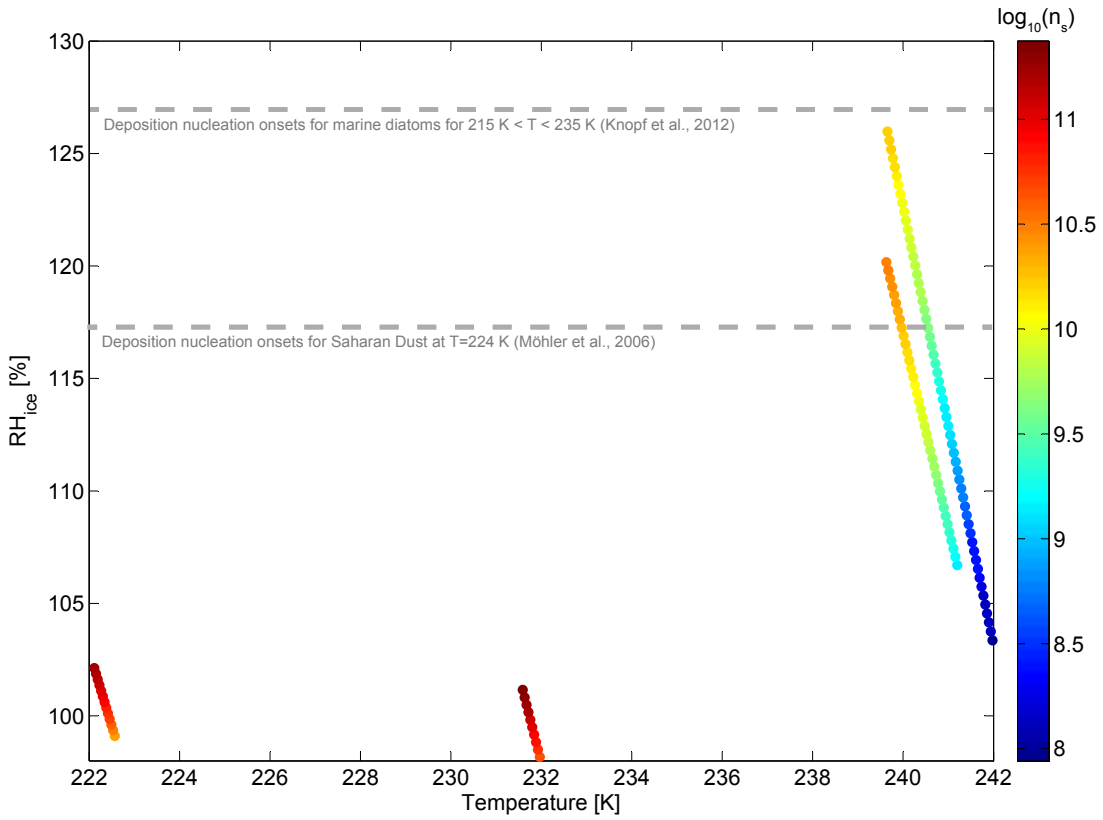

Figure 4.18: *INAS density trajectories for ice nucleation initiated by fossil diatomite via the deposition nucleation mode in the T/RH_{ice} space*

Figure 4.18 shows that experiments with similar T/RH_{ice} trajectories and cooling rates may exhibit different ice nucleation efficiencies. This feature might be either caused by the heterogeneity of the fossil diatomite particles themselves or larger deviations between

measured and actual aerosol surface because the particles are highly non-spherical.

Fossil diatom particles become ice active at very low relative humidity over ice whereas the deposition nucleation onsets for living marine diatomite are much higher at about RH_{ice} = 127% between 215 K and 235 K. Note that marine diatoms not only consist of silicates, but they also contain various proteins and polysaccharides (Knopf et al., 2011). Experimental studies suggest that these organic compounds do not influence the ice nucleation properties of the diatoms (Alpert et al., 2011). However, certain organic compounds may suppress ice nucleation as was shown by AIDA experiments with SOA coated diatomite particles which will be presented in the last section of this chapter. Additionally, organic compounds might prevent the diatom micropores from filling with ambient water and thus prevent freezing within micropores (Marcolli, 2013). The ice nucleation onset for a sample of Saharan Dust is at RH_{ice} = 117 % (Möhler et al., 2006) and fossil diatoms are therefore more efficient ice nuclei than desert dusts.

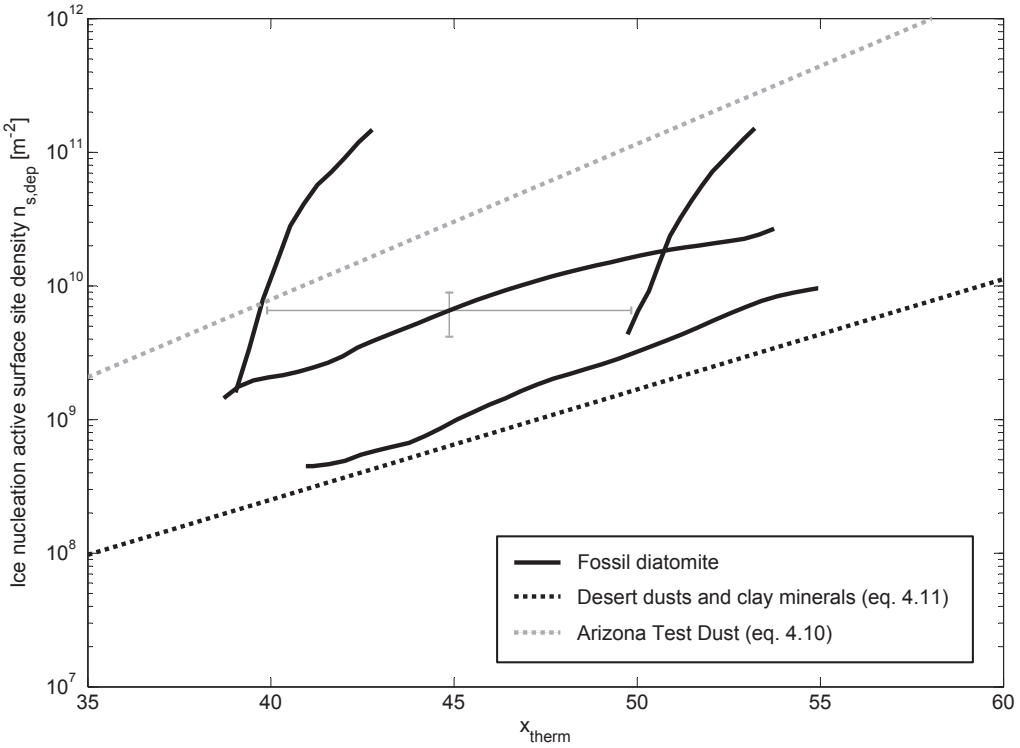

Figure 4.19: *INAS density trajectories for ice nucleation initiated by fossil diatomite via the deposition nucleation mode as a function of* x_{therm}

Figure 4.19 shows the INAS densities for the deposition nucleation mode as a function of the thermodynamic variable x_{therm} with $x_{therm} = -(T - 273.2) + (S_{ice} - 1) \cdot 100$. From Fig. 4.19 it is evident that x_{therm} as a linear combination of temperature and relative humidity is probably only a good approximation for temperatures above 235 K, because temperature as a driving factor for ice nucleation seems to become less important at lower temperatures. The slopes of the INAS densities depicted in Fig. 4.19 differ significantly between experiments below and above 235 K. Therefore, no parameterization was found for deposition nucleation initiated by fossil diatom particles. However, it can still be concluded that fossil diatoms are on average more active ice nuclei with respect to the initiation of deposition mode nucleation than desert dusts and clay minerals. However, fossil diatoms are less ice-active than Arizona Test Dust.

4.2.2 Summary

Immersion freezing and deposition nucleation was investigated for fossil diatomite particles. Fossil diatoms are emitted in particular by the Bodélé sink in Northern Africa which contributes up to 18% to the global dust burden according to model estimates (Todd et al., 2007). Fossil diatoms and fragments proved to be very active ice nuclei in the immersion freezing mode, but also in the deposition nucleation mode. Comparing the ice nucleation active surface site densities, fossil diatoms are more ice-active than desert dusts in both ice nucleation modes. However, it was noted that the estimation of the aerosol surface area relevant for heterogeneous ice nucleation might be difficult for materials with very complex morphologies such as fossil diatom particles.

For immersion freezing, the ice nucleation properties of fossil diatoms can be described by

$$n_{s,imm} = \exp(-0.517 \cdot (T - 273.15) + 12.622) \ [\mathrm{m}^{-2}] \tag{4.13}$$

Note, however, that only one single experimental run could be used to derive this parameterization.

With number concentrations of atmospheric diatom particles not being available, the ice nuclei concentration contributed by fossil diatoms can only be roughly estimated. Assuming that 5% of all dust particles are fossil diatoms and that their size distribution does not differ much from the mineral dust particles, the aerosol surface area contributed by diatom particles can be estimated as $A_{aer} \approx 45\ \mu m^2 cm^{-3}$ according to model estimates of the mineral dust aerosol surface area (Klein et al., 2010). This would result in an ice nuclei concentration of $c_{IN} = 135\ l^{-1}$ at 255 K with the measured ice nuclei concentration being up to $c_{IN,obs} = 300\ l^{-1}$ during a Saharan dust event (Klein et al., 2010). Thus, fossil diatoms could contribute significantly to the global ice nuclei concentration. However, so far no studies report that fossil diatom particles have been found in ice crystal residuals which means that they are probably highly ice-active but also very rare.

4.3 Volcanic ash[2]

Eruptions of volcanoes like El Chichon (1980) or Mt. Pinatubo (1991) had significant impacts on the global atmospheric temperature (Soden et al., 2002) because of the emission of large amounts of sulphur species into the stratosphere. Such major eruptions (with magnitudes larger than 4.5) occur at intervals ranging from four years to about 1000 years depending on the eruption strength. Non-explosive volcanic activities involving slow degassing are associated with at least regional impacts on climate (Durant et al., 2010). For several years, attention to the impact of volcanic emissions on climate has been mainly focused on the contribution of volcanic sulfur species to the stratospheric aerosol layer and the subsequent impact on the global radiation budget (Mather et al., 2003) or, alternatively, the possible interaction between anthropogenic particles and sulphuric acid droplets of volcanic origin (Raga et al., 1999).

During the recent explosive eruption (April/May 2010) of the Eyjafjallajökull located on Iceland's southern coast, not only 3 Tg of SO_2 were released into the atmosphere, but also about 10 Tg of ash mass (Schumann et al., 2011). Estimates from inverse modelling suggest that volcanic ash emissions with regard to particles with diameters between 2.8 and 28 µm amount to approximately 8 Tg (Stohl et al., 2011). The Eyjafjallajökull eruptions in 2010 generally reached heights of several kilometers producing an ash cloud which was transported over a distance of several hundreds of kilometers (Gudmundsson et al., 2010) towards Northern and North Western Europe. Ash particles smaller than 10 µm are predicted to have atmospheric residence times of several days (Rose and Durant, 2009) and may alter cloud properties by acting as ice nuclei in mixed-phase and cirrus clouds.

In laboratory experiments (Durant et al., 2008; Fornea et al., 2009 and references therein) and atmospheric measurements (Bingemer et al., 2012; Seifert et al., 2011) the role of volcanic ash particles as potential ice nuclei has been investigated. Volcanic ash particles ($250 < d < 300$ µm) from Mt. St. Helens were observed to nucleate ice via immersion freezing at temperatures of about 255 K (Fornea et al., 2009). For several Japanese

[2]Large parts of this section were taken from "Ice nucleation properties of fine ash particles from the Eyjafjallajökull eruption in April 2010" (Steinke et al., 2011)

volcanoes such as Mt. Asama, a significant correlation between volcanic activity and an increase of atmospheric ice nuclei concentrations in Tokyo was observed for meteorological conditions which allowed the transport of volcanic ash over several kilometers. The increase in IN concentrations was especially pronounced for temperatures below 258 K (Isono et al., 1959a). A similar observation was made for Hawaiian volcanoes, where eruptions of the Kilauea were followed by IN concentrations (measured at 252 K) rising to more than one order of magnitude above background concentrations (Hobbs et al., 1971).

Even though it was demonstrated that volcanic ash particles can be efficient ice nuclei, it remained unclear whether volcanic ash particles are relevant for atmospheric ice nucleation processes, because the ash particles' properties as ice-forming nuclei had neither been investigated for particles smaller than ~100 µm nor for temperatures below ~250 K. Also, some measurements suggest that not all eruptions contribute to atmospheric IN concentrations, as the ice nucleation properties of volcanic ash particles depend on their volcanic source and the resulting chemical composition (Isono et al., 1959a) - e.g., volcanic ash particles might become deactivated in volcanic plumes which are rich in sulfuric gases (Schnell and Delany, 1976). A comparison of ash samples from ten different Japanese volcanoes indeed has shown that freezing thresholds vary not only amongst volcanoes, but also for different types of eruptions. In general, freezing onset temperatures varied between 250 and 265 K (Isono et al., 1959b; Mason and Maybank, 1958; Schaefer, 1949; Durant et al., 2008).

Ice nucleation properties of volcanic ash were investigated over a temperature range between 219 and 264 K. The volcanic ash sample (referred to as 'EY01') used for the experiments presented in this work had been collected at a distance of 58 km from the Eyjafjallajökull on the morning of April 15, 2010 after a major eruption phase had started on April 13, 2010 (Gudmundsson et al., 2010)[3]. According to a study by Gislason et al. (2011), the ash from Eyjafjallajökull is dominated by andesitic glass. However, they also found crystals of plagioclase, pyroxene and olivine. In addition to the ice nucleation ex-

[3]Mrs. Gudrun Larsen (Institute of Earth Sciences, University of Iceland) is thanked for kindly having provided the volcanic ash sample from Eyjafjallajökull.

periments in the AIDA cloud chamber, filter samples were taken from the aerosol in the cloud chamber and analyzed with an environmental scanning electron microscope (ESEM – FEI Quanta 650 FEG) combined with an energy dispersive X-ray analysis module (EDX – QUANTAX, Bruker). This method gives access to the surface morphology and the chemical composition of individual particles. Additionally, the amount of soluble sulfates on the surfaces of the ash particles was analyzed with an ion chromatograph (DX500, Dionex): for this analysis 53 mg of volcanic ash were suspended in 20 ml of high-purity water (Nanopure, Barnstead) and only the solution was analyzed for major anions and cations including sulfate.

Table 4.5: Overview of AIDA cloud chamber experiments with volcanic ash

Experiment	Initial temperature [K]	Aerosol concentration [cm^{-3}]	Median diameter [µm]	Ice nucleation mode
IN14_95	264	293	0.38	No ice
IN14_98	259	305	0.38	Imm. freezing
IN14_100	253	277	0.35	Imm. freezing
IN14_103	253	506	0.34	Imm. freezing
IN14_105	245	551	0.35	Imm. fr./Dep. nuc.
IN14_107	236	319	0.35	Dep. nucleation
IN14_110	226	185	0.37	Dep. nucleation

In Table 4.5 all cloud chamber experiments investigating the ice nucleation properties of volcanic ash particles are listed.

4.3.1 Characteristics of volcanic ash particles

For investigating the relative contribution of larger particles ($d > 5$ µm) to the ice nucleation efficiency of the total volcanic ash particle population, two ice nucleation experiments (IN14_100 and IN14_103) were conducted at the same temperature, but with different aerosol size cutoffs. As can be seen from Fig. 4.20, this cutoff lies at ~ 15 µm for experiment IN14_100, and at ~ 5 µm for experiment IN14_103. The median of the aerosol surface distribution is shifted from $d_{med,surf}$ = 1.36 µm to a smaller value $d_{med,surf}$ = 0.77 µm when using a cyclone. From the aerosol surface distributions it can be seen that the volcanic ash particles fall mostly within the atmospherically relevant size range of particles

smaller than ~ 10 µm which can stay elevated for several days (Rose and Durant, 2009).

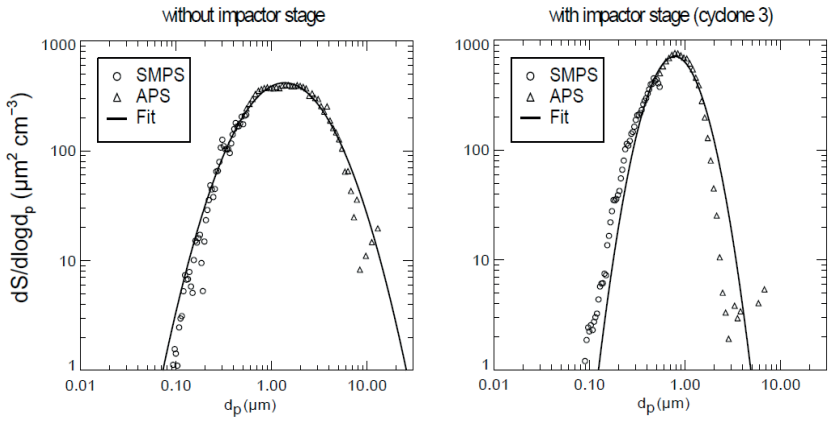

Figure 4.20: *Aerosol surface distributions of volcanic ash particles: comparison between distributions as obtained without (left) and with (right) using an impactor (cyclone 3) – aerosol surface distributions are calculated from number size distributions as measured by APS and SMPS*

a) $d_{med,surf}$ = 1.36 *µm;* σ_{surf} = 2.33 *(exp. IN14_100)*

b) $d_{med,surf}$ = 0.77 *µm;* σ_{surf} = 1.66 *(exp. IN14_103)*

In Fig. 4.21 two ESEM images of volcanic ash particles are shown. The particle on the left side of Fig. 4.21 has relatively sharp edges with smaller particles being attached to the particle's surface. The picture on the right side shows a particle that consists of several small particles (with sizes of ~ 0.2 µm).

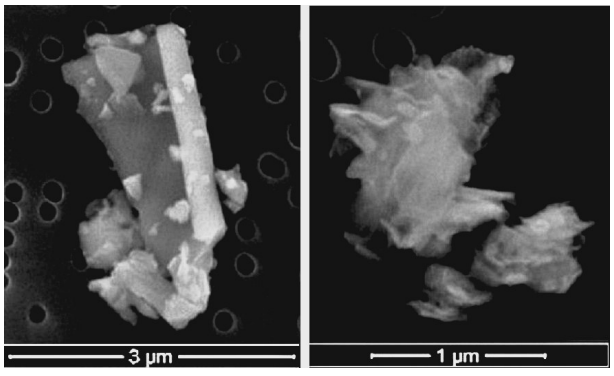

Figure 4.21: *ESEM images of two ash particles from the Eyjafjallajökull (sample name: EY01): examples for different particle surface structures*

The high silicate content of the volcanic ash particles as determined from EDX analysis suggests that they are on average chemically akin to particles belonging to the coarse fraction of certain mineral dusts (e.g., Saharan dust) (Formenti et al., 2003; Linke et al., 2006; Krueger et al., 2004). Compared to mineral dusts, volcanic ash particles may have been exposed to additional chemical processing because of the presence of sulfuric acid during particle production (Mather et al., 2003). Therefore we have also measured the sulfate content in our volcanic ash samples by ion chromatography. The sulfate content as derived from our leaching experiments was approximately 0.1 g per kg of ash mass, which is slightly lower than for similar samples that have been investigated (Eiríksdottir and Alfredsson, 2010). However, direct atmospheric measurements of volcanic ash particles being coated by sulfuric acid are still missing (Flentje et al., 2010).

4.3.2 Immersion freezing by volcanic ash particles

Figure 4.22 depicts the ice nucleation active surface site (INAS) densities derived from two experiments (IN14_100 and IN14_103). Both expansion experiments started at the same temperature, but during the second experiment (IN14_103) a cyclone was operated in series with the rotating brush generator, which resulted in the elimination of particles larger than approximately 5 µm (see Fig. 4.20). Freezing occured after aerosol particles had been activated to droplets. Therefore, Fig. 4.22 represents ice nucleation active surface site densities for immersion freezing of volcanic ash particles. The overlap between both experiments demonstrates that INAS densities $n_{s,imm}$ are similar within uncertainties from measurements and fitting procedures. Thus, it can be concluded that larger particles within the size interval between 5 and 10 µm – constituting roughly half of the total aerosol surface – do not contribute over-proportionally to the INAS density $n_{s,imm}$ in comparison to the particles smaller than 5 µm. The assumption of the INAS density $n_{s,imm}$ for volcanic ash not depending strongly on particle size is therefore supported by this finding.

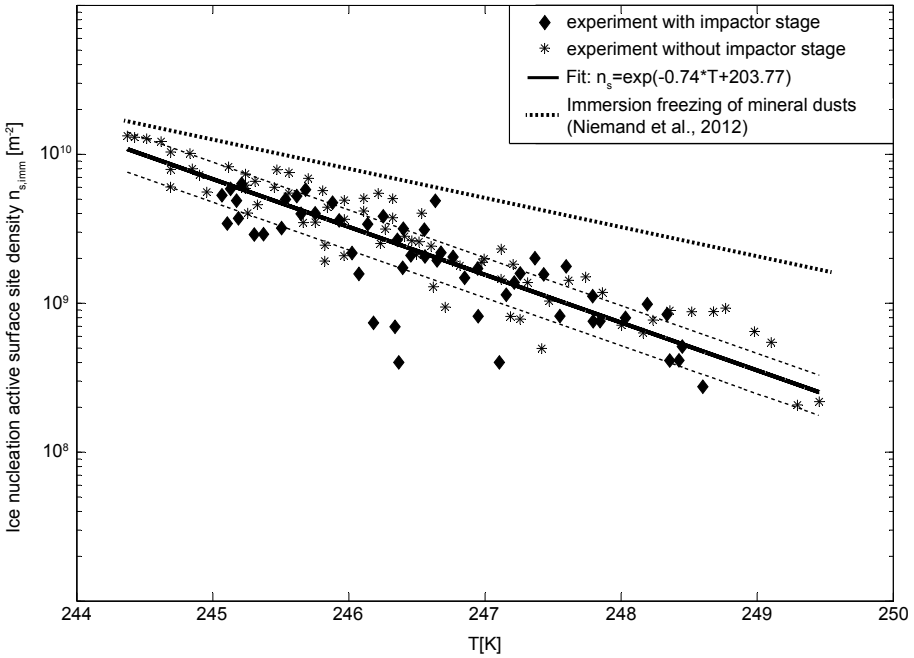

Figure 4.22: *Ice nucleation active surface site densities for immersion freezing of volcanic ash particles (EY01) with fit (—) and measurement uncertainties (- -); for comparison average INAS densities for desert dusts (Niemand et al., 2012) are depicted*

From the measurement data, a fit relating the ice nucleation active surface site density $n_{s,imm}$ and temperature was derived (method described in detail by Niemand et al. (2012)):

$$n_{s,imm}(T) = \frac{n_{imm}}{A_{aer}} = \exp(-0.74 \cdot T + 203.77)\,[\mathrm{m}^{-2}] \tag{4.14}$$

where T is temperature in [K], n_{imm} the ice crystal number density and A_{aer} the aerosol surface density scaled with losses due to diluting the aerosol by pumping. This relation is valid for temperatures between 244 and 250 K. Above 250 K the ice fraction f was less than 0.1 % and therefore only a rough estimate of $n_s \sim 10^8$ m^{-2} at 252 K can be given. The dashed lines in Fig. 4.22 depict the uncertainty $\Delta n_{s,imm}$ of the fit that can be attributed to measurement and evaluation uncertainties in the ice crystal number density n_{imm} (as derived from the welas/welas2 measurements) and the aerosol surface density A_{aer} (as derived from the APS/SMPS measurements). From the measurement uncertainties $\Delta n/n$ and $\Delta A_{aer}/A_{aer}$ being at least ±25%, $\Delta n_{s,imm}/n_{s,imm}$ is estimated to be ±35%.

Note that a factor that could have a major influence on the measurement uncertainty

ΔA_{aer} is that A_{aer} is derived under the simplifying assumption of spherical particles which does not apply for volcanic ash particles. However, also in volcanic ash dispersion models (Emeis et al., 2011) and for the evaluation of atmospheric measurements (Stohl et al., 2011) volcanic ash particles are assumed to be spherical. Note that the review by Murray et al. (2012) points out that measurements by Fornea et al. (2009) which investigated the droplet freezing properties of large particles (d > 100 µm) delivered ice nucleation active surface site densities at temperatures above 250 K which matched very well with the temperature trend of the measurements presented in this work. Compared to desert dusts, volcanic ash is less efficient than natural mineral dusts for temperatures above 245 K.

4.3.3 Deposition nucleation by volcanic ash particles

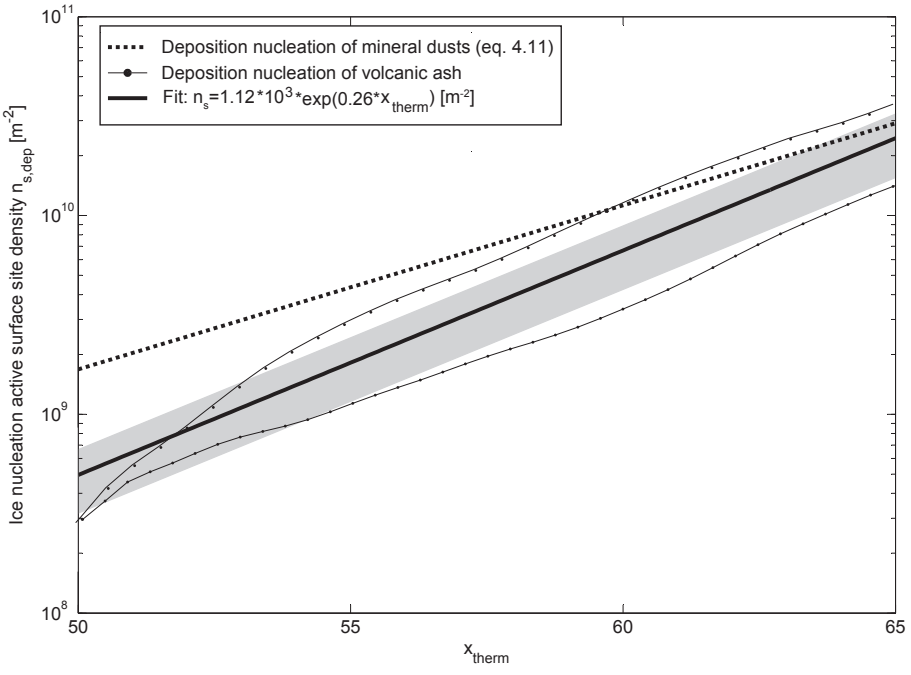

Figure 4.23: *Ice nucleation active surface site densities for deposition nucleation of volcanic ash particles (EY01) in comparison to the ice nucleation efficiency of mineral dusts; grey shading indicates the measurement uncertainty of the INAS density*

Analogously as for the immersion freezing experiments with volcanic ash, the ice nu-

cleation active surface site densities have been calculated for deposition nucleation at temperatures below 242 K. In Fig. 4.23 ice nucleation active surface site densities are presented as a function of the thermodynamic variable x_{therm} which is a linear combination of temperature and relative humidity over ice. As a comparison, the ice nucleation active surface site density derived for mineral dusts and clay minerals which has also been derived from cloud chamber experiments is depicted. Figure 4.23 shows that volcanic ash particles are slightly less ice-active than mineral dusts in the deposition nucleation mode which is similar to their observed immersion freezing properties.

4.3.4 Summary

Volcanic ash particles initiate the formation of ice over a large range of atmospheric conditions with regard to relative humidity and temperature. Our results agree well with a study of Hoyle et al. (2011) in which the ice nucleation properties of the same Eyjafjallajökull sample were investigated. For AIDA cloud chamber experiments, no ice formation was observed at 260 K and the ice active fractions of volcanic ash particle did not exceed a threshold of 0.1% before reaching temperatures lower than 250 K. Deposition nucleation was observed only at temperatures below 242 K. In our experiments the maximum ice fraction for volcanic ash is about 40% for deposition nucleation at RH_{ice} = 117% and T= 223 K.

Regarding the measured ice nucleation active surface site density for immersion mode freezing and deposition nucleation, fine volcanic ash from the Eyjafjallajökull eruption in April 2010 is slightly less efficient compared to certain natural mineral dusts both in immersion freezing and deposition nucleation mode (Field et al., 2006; Niemand et al., 2012; Möhler et al., 2006). Note that even though volcanic ash particles can act as efficient ice nuclei, they are currently neglected in global climate models (e.g., Hoose et al. (2010)). From atmospheric size distribution measurements in the Eyjafjallajökull ash plume (Schumann et al., 2011), estimates for atmospheric ice nuclei concentrations can be derived from the aerosol surface distributions and the ice nucleation active surface site density at a certain temperature: for immersion freezing at 248 K, roughly a concentration between 30 and 150 IN/l can be calculated with the aerosol surfaces ($A_L \approx 30$ $\mu m^2 cm^{-3}$ and $A_{NA} \approx 150$ $\mu m^2 cm^{-3}$) taken from Fig. 7 in Schumann et al. (2011) in which

aerosol surface distributions from two measurements over Leipzig (April 19th) and the North Atlantic (May 2nd) are depicted.

4.4 Soil dust

Mineral dust particles are mainly emitted by desert areas and arid regions of the world. The Saharan desert is one of the major dust sources on Earth and significantly contributes to the global dust burden with estimated emission fluxes for mineral dusts ranging from 500 to 4300 Tg yr^{-1} (Tegen and Schepanski, 2009; Huneeus et al., 2011). Freshly emitted dust particles and dust particles with changed physico-chemical properties due to long-range transport are assumed to significantly influence the structure of clouds and thus global climate.

Mineral dust particles consisting mainly of alumina silicates and clay minerals nucleate ice most efficiently at around 250 K at water-saturated conditions (Murray et al., 2012). However, ice crystals in clouds coinciding with dust events have already been detected for cloud top temperatures as high as 268 K (Sassen et al., 2003). This might be explained partly by dust events being accompanied by bioaerosols (Pratt et al., 2009; Hallar et al., 2011) because primary biological particles such as fungi or bacteria are able to initiate the formation of ice already at temperatures slightly below 273 K (Després et al., 2012). Desert dust particles transported through the atmosphere carry few microorganisms which are very well adapted to stressful environmental conditions such as desiccation, UV irradiation and nutrient depriviation (Kellogg and Griffin, 2006; Perfumo and Marchant, 2010; Toepfer et al., 2012). However, mineral dust particles containing significant amounts of organic matter are predominantly emitted from agricultural areas. Estimates regarding the contribution of agricultural areas to the global dust burden are not very well confined and range from less than 10% (Tegen et al., 2004) to 20-50% (Forster et al., 2007; Funk and Reuter, 2006; Ginoux et al., 2012).

Enhanced concentrations of biogenic ice nuclei were found over agricultural areas, especially during tilling or harvesting activities which caused even higher dust emission fluxes than wind erosion (Garcia et al., 2012; Bowers et al., 2011). The biological origin of these ice nuclei was deduced from a reduction in the ice nucleation efficiency by more than a factor of 10 after heat treatment at 371 K (Garcia et al., 2012). However, the composition

of biological ice nuclei over agricultural areas is not completely understood. For example, atmospheric bacterial communities sometimes were different than those populations found in leafs and soils on the ground (Bowers et al., 2011). Also, field measurements found ice-active bacteria from the near-surface environment to be under-represented in the atmosphere (Garcia et al., 2012).
Figure 4.24 shows a flourescence image of soil dust particles associated with colonies of living and dead bacteria.

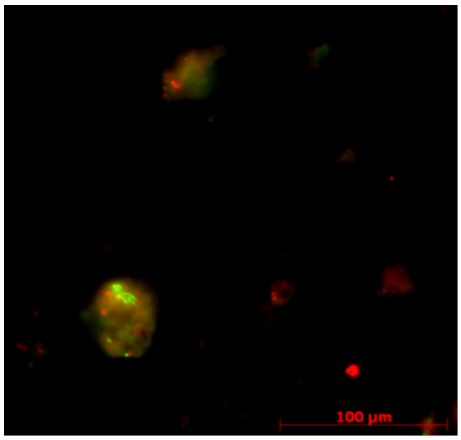

Figure 4.24: *Flourescence microscopy image of soil dust particles with living (green) and dead (red) bacteria (courtesy of A. Rieder)*

This work presents experimental results from AIDA cloud chamber studies investigating the ice nucleation properties of four different soil dust samples from agricultural areas in Germany, Mongolia and Argentina[4]. The experiments were intended to find relations between the observed ice nucleation efficiencies of the soil samples and their respective organic matter content or biological components (e.g. certain bacteria, fungi or other species). All soil samples were collected from the top soil - further details regarding the origin of the samples are listed in Table 4.6.

[4]The soil samples from Northern Germany, Mongolia and Argentina were provided by R. Funk (Zentrum für Agrarlandschaftsforschung)

Table 4.6: Overview of soil samples used for ice nucleation experiments in this work

	Germany Brandenburg (German Soil)	Germany Baden-Württemberg (Karlsruhe Soil)	Argentina La Pampa (Argentinian Soil)	China Inner Mongolia (Mongolian Soil)
Geological origin	Fluvial deposits	Fluvial deposits	Aeolian deposits	Aeolian deposits
Land use	Arable land	Arable land	Arable land	Pasture
Soil texture	Sand/loamy sand	n.a.	Sandy loam	Loam
Organic matter (dust)	2.89%	n.a.	1.45%	2.49%

All samples were sieved in order to obtain the dust fraction with particle sizes smaller than 63 µm except the Karlsruhe Soil which was sieved with a 75 µm mesh. The Argentinian Soil was available as a sample collected from the soil matrix directly, but also as dust trapped in 3.3 m height during a dust storm. The soil samples were taken from areas where soil textures and meteorological conditions may lead to an increased dust emission flux by wind erosion. The organic content of all soil samples was 1-3 % for the particles smaller than 63 µm. In the next section, a detailed analysis of the physico-chemical and the microbiological properties of three dust samples (German Soil, Argentinian Soil and Mongolian Soil) will be presented.

4.4.1 Soil sample analysis

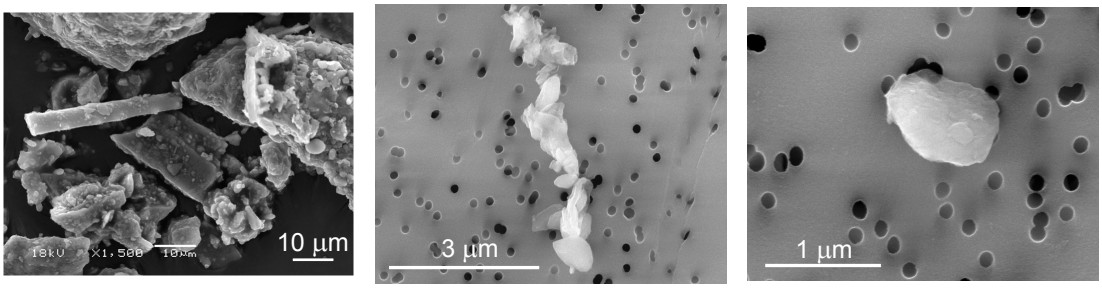

Figure 4.25: *Microscope images of soil dust particles from the bulk sample (left), an agglomerate (middle) and a single particle (right) - particles are taken from the Argentinian soil sample (courtesy of J. Busse and A. Kiselev)*

Generally, soil dusts are very complex mixtures with alumina silicates and organo-mineral complexes being the main components. Figure 4.25 shows microscope images of soil

dust particles (Argentinian Soil). In Fig. 4.25 (left) a TEM image[5] of the bulk sample is shown, whereas the other subfigures[6] show one agglomerate and a single dust particle as collected from the AIDA cloud chamber before an expansion experiment with Argentinian Soil. Argentinian soil dust mainly consists of mineral particles which often have organic agglomerates attached to their surfaces. Also, from visual inspection of the TEM image (Fig. 4.25 (left)) it could be guessed that some of the particles are phytoliths. Microscope images of the other dust samples (not shown) suggest similar features as for the Argentinian sample.

Elemental composition

Table 4.7: Analysis of the chemical composition of three dust samples - all values are given in $mg \cdot kg^{-1}$

	Fe	Mn	Cu	Zn	Ca	Mg	K	Al
Argentinian Soil	31928	485	78	6	2267	4654	5008	39457
German Soil	12185	577	263	48	2219	1649	4149	21957
Mongolian Soil	30149	546	121	417	3929	5639	6970	23431

The elemental composition of three dust samples was analyzed and is shown in Table 4.7[7]. Due to their different geological origin, the soil dust samples differ with regard to their elemental composition. The soil sample from Northern Germany contains much less iron oxides than the Mongolian Soil and the Argentinian Soil. However, the German sample contain more copper ions than the other two samples. Very striking is the enrichment of the Mongolian Soil sample in zinc and in carbonates. Note that the German Soil sample also contains less magnesium and potassium than the other samples.

[5] Image courtesy: J. Busse (Zentrum für Agrarlandschaftsforschung)

[6] Image courtesy: A. Kiselev (Karlsruhe Institute of Technology)

[7] Results from the chemical analysis were provided by R. Funk

Table 4.8: Comparison to the elemental composition of desert dusts

	K/Al	Ca/Al	Fe/Al
Argentinian Soil	0.13	0.06	0.81
German Soil	0.19	0.10	0.55
Mongolian Soil	0.30	0.17	1.29
Saharan desert dust	0.21	0.56	0.56
Arizona Test Dust	0.21	0.49	0.27

Table 4.8 then lists for the three soil samples the mass ratios K/Al, Ca/Al and Fe/Al in order to compare these values with the ratios for Saharan dust (Gomes and Gillette, 1993) and Arizona Test Dust (Vlasenko et al., 2005) which is a dust standard. The Mongolian sample is significantly enriched in iron oxides. Compared to the desert dust, the agricultural dusts have similar K/Al ratios, but are depleted in carbonates. The soil dust samples were enriched in iron oxides.

Mineralogy and organic matter from FTIR measurements

The different elemental composition of German Soil, Argentinian Soil and Mongolian Soil and their different geological origins suggest that these three soil samples might differ regarding their mineralogy and their organic matter content. Fourier transform infrared (FTIR) spectroscopy[8] was used to further analyze the properties of the soil organic matter and also the mineralogical composition.

Absorption intensities were measured for different vibrational excitations of certain molecular bonds which are characteristic for organic matter such as C-H (alkyls) or C=O (ketones, carboxylic acids or amides). The C-H bands are assumed to be an indicator for hydrophobic properties (Capriel et al., 1995) whereas the C=O bands are associated with hydrophilicity (Morrison and Boyd, 1986). Thus, the C-H/C=O ratio of the spectra can be used as a measure for the potential wettability of the soil organic matter (Ellerbrock et al., 2005) with high values indicating a low potential wettability (i.e. high potential hydrophobicity).

[8] FTIR spectroscopy results were provided by M. Leue.

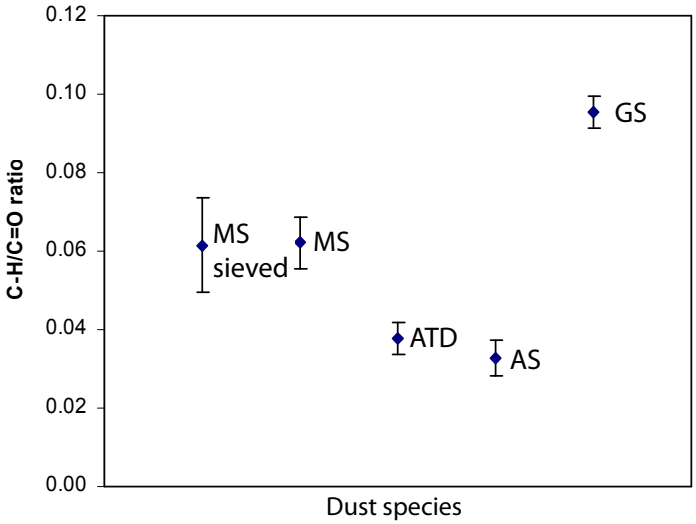

Figure 4.26: *Hydrophobicity of the soil organic matter as inferred from FTIR spectroscopy; C-H absorption intensities are taken as an indicator for hydrophobic organic matter whereas C=O absorption intensities correspond to the hydrophilic organic matter content of the soil samples (FTIR measurement: courtesy of M. Leue)*

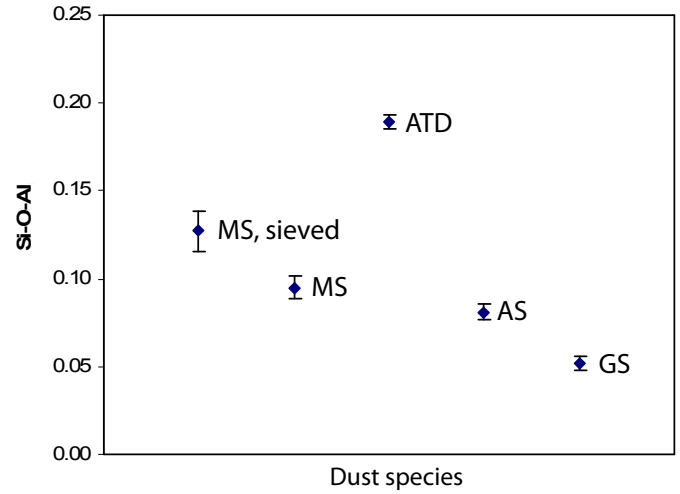

Figure 4.27: *Clay content as inferred from the FTIR absorption intensities measured at the Si-O-Al band (FTIR measurement: courtesy of M. Leue)*

Figure 4.26 shows the C-H/C=O absorption ratios for the bulk samples of Argentinian Soil, German Soil, Mongolian Soil and Arizona Test Dust. Arizona Test Dust is expected to contain very little amounts of organic matter because its origin lies in the desert areas of Arizona, USA. Thus, the C-H and C=O absorptions intensities for Arizona Test Dust merely exceed the detections limits and thus the measured absorption values are probably more uncertain than for the other samples. For Mongolian Soil and German Soil the C-H/C=O ratios indicate that the soil organic matter is less wettable than the organic matter within the Argentinian Soil sample.

Absorption at λ = 690 cm^{-1} can be attributed to the Si-O-Al band which indicates the presence of clay minerals. The absorption intensities at λ = 690 cm^{-1} are shown in Fig. 4.27 for the bulk samples of Argentinian Soil, German Soil, Mongolian Soil and Arizona Test Dust. Arizona Test Dust shows significant absorption at the Si-O-Al band whereas the values for the soil dusts are lower. This agrees with studies finding that Arizona Test Dust may contain up to 50% clay minerals (Broadley et al., 2012). From Fig. 4.27 it can be concluded that Mongolian Soil contains more clay minerals than Argentinian Soil and German Soil.

Microbiology

Three soil dust samples (Argentinian Soil, German Soil and Mongolian Soil) were also subjected to a more detailed microbiological analysis delivering an assessment of the dominating microbiological species.

Table 4.9: Results from PCR analysis: Combined number of cells and cell fragments per g

	Bacteria	Actinobacteria	Pseudonomads	Fungi
Argentinian Soil	$(1.2 \pm 0.1) \cdot 10^9$	$(5.8 \pm 0.6) \cdot 10^8$	$(1.5 \pm 0.6) \cdot 10^5$	$(1.8 \pm 1.2) \cdot 10^6$
German Soil	$(9.5 \pm 3.1) \cdot 10^8$	$(5.2 \pm 1.0) \cdot 10^8$	$(2.9 \pm 0.9) \cdot 10^6$	$(4.7 \pm 3.4) \cdot 10^7$
Mongolian Soil	$(2.0 \pm 0.2) \cdot 10^9$	$(1.4 \pm 0.1) \cdot 10^9$	$(2.1 \pm 1.6) \cdot 10^5$	$(1.3 \pm 0.9) \cdot 10^6$

Table 4.9 shows values for the number of cells and cell fragments which have been detected by using a PCR analysis[9]. In Tab. 4.9 the number concentrations of bacteria and fungi is listed for Argentinian Soil, German Soil and Mongolian Soil. Actinobacteria and Pseudonomads are analyzed separately and are treated as subgroups of the whole bacteria population. The soil dust from Mongolia contains about twice as much bacteria than the other two samples from Germany and Argentina. Conversely, the number of fungi and fungi remnants found in the sample from Northern Germany is by a factor of 10 higher than for the samples from Mongolia and Argentina. Neverless, the total number of microorganisms and cell fragments is highest for the Mongolian Soil.
The high biological activity level of the Mongolian Soil is supported by Waveband Integrated Bioaerosol Sensor (WIBS-4) measurements of the aerosol population within the AIDA cloud chamber: (8.5±1.5)% of all Mongolian Soil particles showed fluorescence signatures (i.e. biological activity) whereas for Argentinian Soil this fraction is (2.9 ± 0.7)% and for the German Soil only (2.2 ± 0.5)% of all particles fluoresced (E. Toprak, unpublished data). Note that the PCR analysis was conducted for the bulk samples which contained particles with diameters up to d = 63 µm, whereas the aerosol population within the AIDA cloud chamber is restricted to particles smaller than ≈ 15 µm.

Single particle mass spectrometry has been used to investigate how frequently particles with certain biological ion markers occur for each individual soil sample, given as a fraction of the total number of analyzed particles. Biological markers were found for 17% of all particles belonging to the Mongolian sample, but only for 12% and 5% of German Soil and Argentinian Soil particles (B. Sierau, unpublished data). Note that the mass spectrometry analysis has been conducted for the bulk samples like the PCR analysis.

Additionally, the total number of viable cells has been inferred from cultivating soil dust particles on R2A agar for 5 days at 250.7 K. These tests indicate that the Mongolian Soil contains much less viable cells than the Argentinian Soil. The total number of viable cells differ approximately by a factor of 50 between Mongolian Soil and Argentinian Soil (S. Kirchen, unpulished data). These measurements were like the WIBS-4 measurements

[9]PCR analysis data is courtesy of A. Ulrich

conducted for aerosol particles extracted from the AIDA cloud chamber.

From the microbiological analysis, it can be concluded that the Mongolian Soil was the biologically most active soil sample but it did not contain the highest number of viable cells. The German Soil sample was characterized by a high number of fungi and fungi fragments.

For the ice nucleation experiments, two additional samples were produced from the Argentinian soil dust sample by exposing a part of the sample to dry heat (383 K for one hour) and another part to high energy gamma radiation for several days. Note that the Argentinian Soil sample was chosen because viability tests had shown that this sample contained the highest number of viable organisms. Both treatments resulted in a drastic reduction of the number of viable organisms which could be inferred from cultivating these two samples on a R2A agar medium as depicted in Fig 4.28.

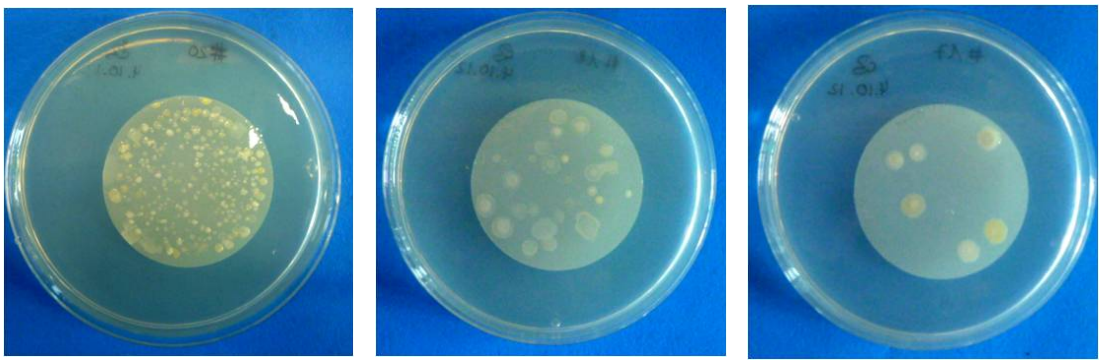

Figure 4.28: *Pictures of soil dust particles (Argentinian Soil) having been incubated on a R2A agar: untreated (left), exposed to high temperature (middle) and exposed to high energy irradiation (right) - the number of viable soil dust organisms is drastically reduced by heat or radiation treatment (images: courtesy of S. Kirchen)*

4.4.2 Ice nucleation properties of soil dust particles

The ice nucleation properties of the four soil dust samples were investigated for immersion freezing and deposition nucleation over a temperature range between 229 and 271 K. All experiments for which the ice nucleation mode could be determined unambiguously are listed in Table 4.10.

Table 4.10: Overview of AIDA cloud chamber experiments with Karlsruhe Soil (KS), German Soil (GS), Mongolian Soil (MS) and Argentinian Soil (AS); AS_gamma and AS_heat refers to treated soil samples

Experiment	Aerosol	Initial temperature [K]	Aerosol concentration [cm^{-3}]	Median diameter [µm]	Ice nucl. mode
IN15_56	KS	262	268	0.54	Imm.
IN16_02	KS	264	230	0.40	Imm.
IN16_03	KS	271	262	0.42	Imm.
IN16_09	KS	264	232	0.43	Imm.
IN19_05	MS	258	95	0.33	Imm.
IN19_06	GS	258	124	0.44	Imm.
IN19_07	AS	259	138	0.42	Imm.
IN19_35	AS_gamma	254	162	0.40	Imm.
IN19_43	AS	254	165	0.41	Imm.
IN19_44	AS_heat	254	132	0.50	Imm.
IN19_46	GS	255	167	0.45	Imm.
IN15_50	KS	233	295	0.40	Dep.
IN15_51	KS	242	339	0.46	Dep.
IN19_09	AS	248	144	0.42	Dep.
IN19_11	MS	248	124	0.52	Dep.
IN19_18	AS_wind	247	121	0.51	Dep.
IN19_30	AS_gamma	247	163	0.40	Dep.
IN19_31	AS_heat	248	224	0.35	Dep.
IN19_33	GS	248	194	0.28	Dep.
INUIT04_40	AS	248	260	0.40	Dep.
INUIT04_46	MS	238	112	0.31	Dep. nucleation
INUIT04_48	AS	238	269	0.40	Dep. nucleation

Immersion freezing initiated by soil dust particles

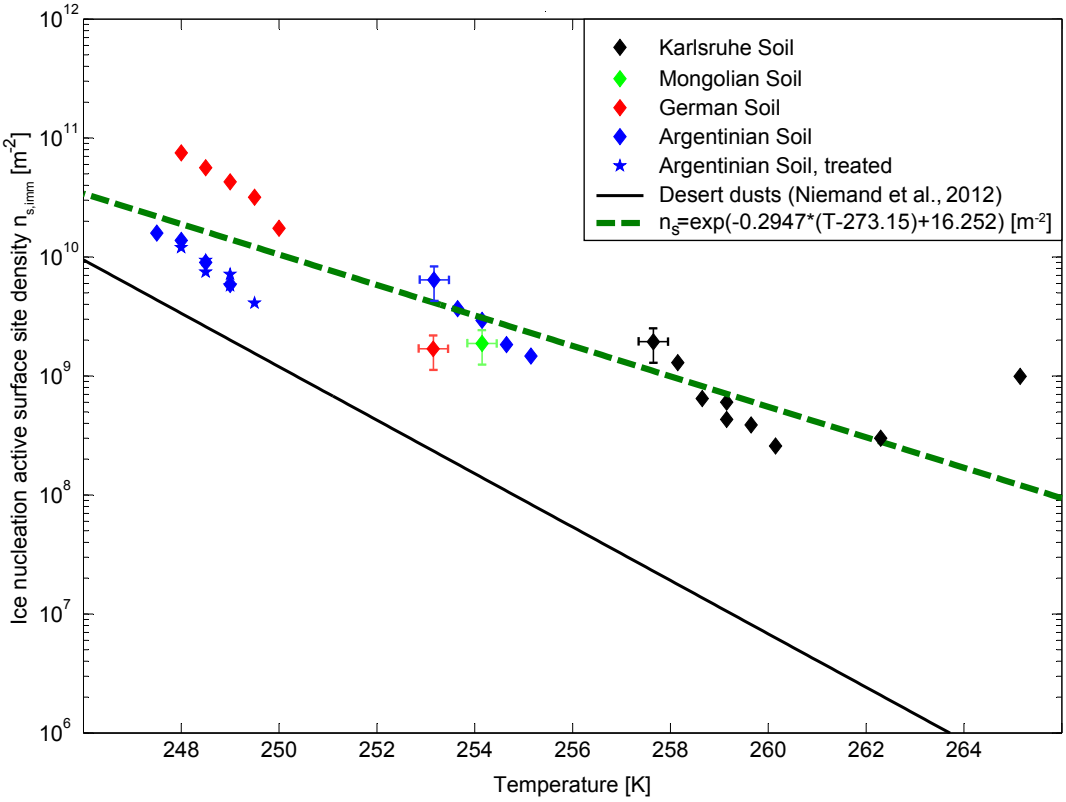

Figure 4.29: *Ice nucleation active surface site densities for immersion freezing initiated by soil dusts enriched with organic matter; for comparison the average INAS densities observed for desert dusts are shown*

Figure 4.29 shows the ice nucleation efficiencies for immersion freezing initiated by the four samples described in Table 4.6 and the two treated dust samples. The ice nucleation efficiencies are expressed as the ice nucleation active surface site (INAS) density n_s [m^{-2}] which is given by $n_s = n_{ice}/A_{aer}$ with n_{ice} [cm^{-3}] being the observed ice crystal concentration for a specific AIDA cloud chamber experiment and A_{aer} [µm^{2}cm^3] being the aerosol surface area which is available for the immersion freezing process, i.e. the aerosol surface that belongs to particles immersed within a droplet. The measurement uncertainties $\Delta n_{ice}/n_{ice} \approx 25\%$ and $\Delta A_{aer}/A_{aer} \approx 25\%$ translate into an uncertainty of the ice nucleation active surface site density $\Delta n_s/n_s \approx 35\%$. Note that the actual aerosol surface area might be underestimated by A_{aer} because it was derived from the geometric

surface using the volume equivalent diameter derived from the size distribution measurements.

The ice nucleation efficiencies depicted in Fig. 4.29 can be described by a temperature dependent relation for the INAS density with

$$n_{s,imm} = \exp(-0.295 \cdot (T - 273.15) + 16.252) \ [\mathrm{m}^{-2}] \tag{4.15}$$

The parameterization described by eq. 4.17 is only valid between 247 and 265 K.

The INAS densities for the four soil samples are compared to ice nucleation efficiencies of gamma irradiated or heated Argentinian soil and also to desert dusts which are assumed to contain only small amounts of organic matter. From Fig. 4.29 it can be concluded that the four soil dust samples are characterized by consistently higher INAS densities than the desert dusts over the temperature range between 247 and 265 K. This enhanced ice nucleation efficiency of the soil dusts is especially evident at higher temperatures. Mongolian Soil being the soil dust with the highest biological activity could not be identified as the most ice active sample. The ice nucleation efficiency of the soil samples did not differ much at 254 K but the German Soil sample was most ice active at temperatures belown 251 K. Note that the German Soil contained the highest number of fungi and fungi fragments.

Even though a severe reduction of the number of viable cells was observed, neither the heat treatment nor the irradiation had an effect on the ice nucleation efficiency of Argentinian Soil even though the treatments were intended not only to reduce the number of viable microorganisms, but also to possibly break up organic compounds. Other studies have found that heat treatments drastically reduce the ice nucleation efficiency of soil dusts (Garcia et al., 2012; Conen et al., 2011). It is, however, not entirely clear how organic matter responds to heat or irradiation. It should be considered that organic matter in soils is not only present as free organic matter, but large parts may exist in various mixing states such as mineral particles with organic coatings or organo-clay micro aggregates. These organo-mineral complex are presumably more stable than free organic matter (Chenu and Plante, 2006). Also, it has to be taken into consideration that heating

of organic matter may result in the production of new chemical compounds (González-Pérez et al., 2004). INAS densities for soil dusts measured by O'Sullivan et al. (2013) are by a factor of 20 smaller at 250 K than the average INAS density values observed in this study. Note, however, that in the study by O'Sullivan et al. (2013) the aerosol surface areas were quantified through BET analyses which deliver larger surface values than the APS/SMPS measurements and consequently smaller INAS densities.

Deposition nucleation initiated by soil dust particles

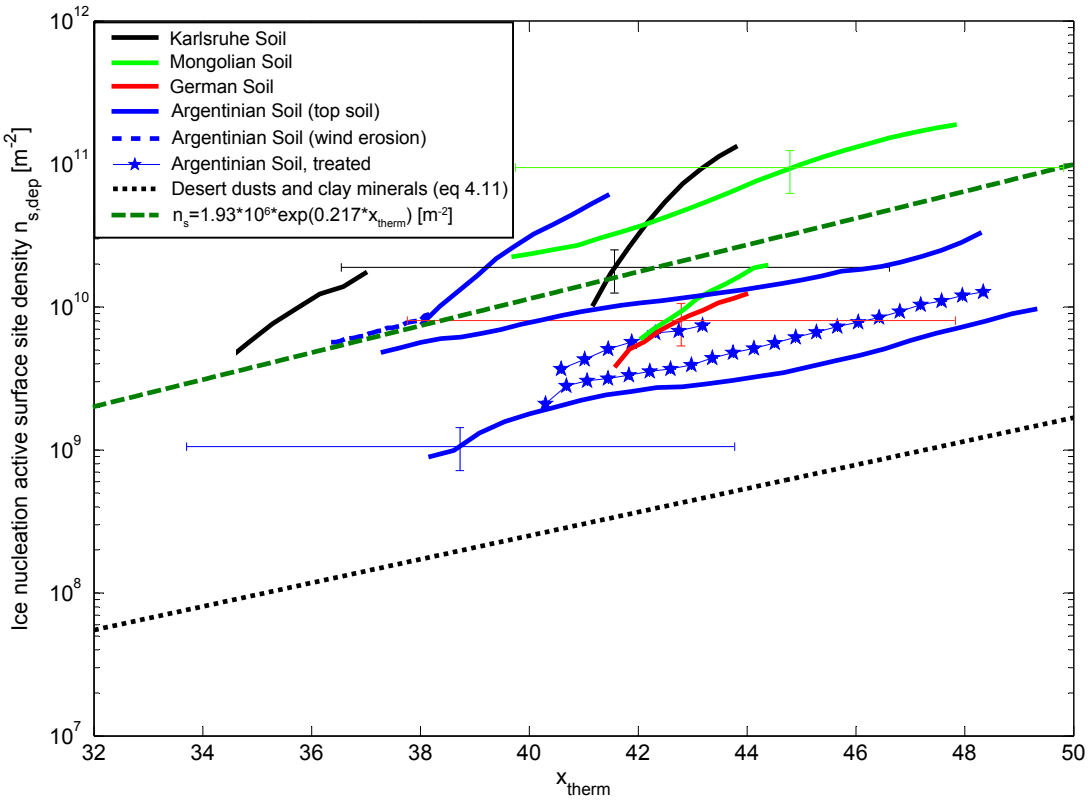

Figure 4.30: *Ice nucleation active surface site densities for deposition nucleation initiated by soil dusts compared to the INAS densities of desert dusts and clay minerals*

Ice nucleation efficiencies were also measured for deposition mode nucleation initiated by soil dust particles and are expressed as INAS densities. The ice nucleation active surface site densities are depicted in Fig. 4.30 as a function of the thermodynamic variable x_{therm}

with $x_{therm} = -(T \cdot [K^{-1}] - 273.2) + (S_{ice} - 1) \cdot 100$. The INAS densities are depicted for water subsaturated conditions and temperatures between 235 and 248 K. For comparison, the INAS densities predicted for desert dusts and clay minerals are represented as well. From Fig. 4.30 it can be observed that the ice nucleation efficiencies of the different soil samples are remarkably similar. Note that in Fig. 4.30 also the INAS densities for windblown Argentinian Soil are depicted. The INAS density values for this sample which should resemble atmospheric dust particles do not differ much from the INAS densities observed for the top soil sample. Similarly as for immersion freezing, the deposition nucleation efficiency of Argentinian Soil is not influenced by exposing the dust sample to dry heat or radiation.

The observed variations in INAS densities among the dust samples can be both attributed to the natural variability of the soil dusts and the approximations made by using x_{therm} for describing the deposition nucleation efficiency. Nevertheless, within one order of magnitude and with the thermodynamic variable x_{therm} varying within the interval $32 < x_{therm} < 50$, the INAS densities for deposition nucleation of soil dusts can be described by a fitting function

$$n_{s,dep} = 1.93 \cdot 10^6 \cdot \exp(0.217 \cdot x_{therm}) \ [\mathrm{m}^{-2}] \tag{4.16}$$

The ice nucleation active surface site densities were found to be higher than predicted for deposition nucleation initiated by desert dust particles and clay minerals.

4.4.3 Summary

The ice nucleation efficiencies measured for the soil dusts are very similar among the four samples despite differences in the elemental composition, the clay content and the biological activity. The observed INAS densities are consistently higher than for desert dusts and clay minerals, both for immersion freezing and deposition nucleation mode.
The ice nucleation efficiencies can be expressed by INAS density functions

$$n_{s,imm} = \exp(-0.295 \cdot (T - 273.15) + 16.252) \ [\mathrm{m}^{-2}] \tag{4.17}$$

for immersion freezing occuring between 247 and 265 K, and for deposition nucleation by

$$n_{s,dep} = 1.93 \cdot 10^6 \cdot \exp(0.217 \cdot x_{therm}) \ [\mathrm{m}^{-2}] \tag{4.18}$$

with the thermodynamic variable x_{therm} varying within the interval $32 < x_{therm} < 50$.

Mongolian Soil was the sample with the highest number of microorganisms, but not the most ice-active soil dust. FTIR absorption spectroscopy indicated that for Mongolian Soil also the clay content was the highest among the three soil samples that were investigated in greater detail. German Soil which is characterized by the highest number of fungi and fungi fragments was slightly more ice-active below 251 K whereas at higher temperature the soil samples were similarly ice active. Exposing Argentinian soil to dry heat (383 K) led to a reduction in the number of viable organisms but did not deteriorate the ice nucleation efficiency of Argentinian Soil which is in contradiction to the findings of other studies.
In conclusion, the ice nucleation efficiency of soil dusts could not directly be related to the biological activity, clay content or the elemental composition. The increased ice nucleation efficiency at higher temperatures ($T > 254$ K) might be attributed to primary biological particles (auch as bacteria and fungi) which are more relevant at small supercoolings, whereas at lower temperatures the stable organic matter becomes more important. Also, differences in mineralogy might explain the increased ice nucleation efficiency when comparing soil dust from agricultural fields and mineral dust from desert areas.

The concentration of ice nuclei contributed by soil dusts can be very roughly estimated by assuming that approximately 1% of all dust particles are emitted from agricultural fields which is a conservative estimate compared to models suggesting contributions up to 25% (Ginoux et al., 2012). The average dust concentrations of particles available for heterogeneous freezing lie between 10 and 50000 l^{-1} according to model simulations (Hoose et al., 2010; Bangert et al., 2012). Under the assumption of a dust particle diameter d = 1.0 µm and by using eq. 4.17, the IN concentrations caused by soil dust might reach 3 l^{-1} at 255 K. For mineral dust particles emitted from desert areas (estimated as 99% of the global mineral dust concentration) the IN concentrations can be calculated analoguously by employing the parameterization proposed by Niemand et al. (2012)

for immersion freezing by desert dust particles. The parameterization by Niemand et al. (2012) predicts ice crystal concentrations up to 14 l^{-1} at 255 K. Even though these ice nuclei concentrations are very rough estimates it can be concluded that soil dust particles may contribute non-negligibly to the global ice nuclei population.

4.5 Ice nucleation properties of coated dust particles

Mineral dust particles are very ubiquitous in the atmosphere as dust is frequently lofted into the air from desert areas and arid regions. Gaseous species such as sulfates, nitrates and organics may adsorb to the surface of mineral dust particles because dust is transported over very large distances (Murphy and Thomson, 1997). Dust plumes from the Saharan desert were found to contain dust particles ($d > 1$ µm) which were almost all coated with sulfate layers with an average thickness of 60 nm (Kandler et al., 2007). Coatings are assumed to change the physico-chemical properties of mineral dust particles and are thus suspected to change processes through which mineral dust particles and clouds interact such as droplet activation and heterogeneous ice nucleation.

Emissions of secondary organic and sulfate aerosol particles

Organic aerosol mainly consists of water-soluble compounds with complex multifunctional compositions. Organic compounds are either emitted as particulate matter (primary organic aerosol - POA) or as particles formed from reaction products of oxidized organic species in the gas phase (secondary organic aerosol - SOA). Terpenes emitted from vegetated areas are assumed to be the major source of atmospheric SOA even though the exact chemical reaction pathways are not completely understood (Kanakidou et al., 2005). Aromatic compounds from anthropogenic sources were also identified as precursors for the formation of SOA (Odum et al., 1996). Estimates for the global production of SOA range from 12 to 70 Tg yr^{-1} (Kanakidou et al., 2005).

Sulfate aerosols nucleate from reaction products originating from the reaction of sulfur dioxide with other compounds and water vapor. One of the most relevant pathways for the formation of sulfates is the oxidization of SO_2 through reaction with OH radicals. Precursors for the formation of sulfate aerosols are emitted as by-products of combustion processes or by natural sources such as volcanoes and oceans with global SO_2 emissions being around 70 Tg S yr^{-1} (Huneeus et al., 2013).

Influence of secondary organics and sulfate coatings on the ice nucleation properties of mineral dusts and clay minerals

With sulfates and secondary organic compounds being abundant in the upper and lower troposphere, several laboratory studies investigated the influence of coatings with sulfuric acid or organics on the ice nucleation properties of mineral dusts, clay minerals and mineral dust surrogates. Some studies also investigated the freezing of acid or organic solutions with solid mineral dust inclusions as a substitute for coated mineral dust particles (see references in Tables 4.11 and 4.12).

Table 4.11: Overview of experiments investigating the effect of coatings with secondary organic compounds on the ice nucleation properties of mineral dusts, clay minerals and mineral dust surrogates

Study	Temperature range	Ice nucleation modes	Core material
Möhler et al. (2008a)	205 to 210 K	Dep.	ATD (dry, polydisp.)
Möhler et al. (2008a)	205 to 210 K	Dep.	Illite (dry, polydisp.)
Koehler et al. (2010)	208 to 253 K	Cond., dep.	ATD (dry, monodisp.)
Niemand (2012)	224 to 251 K	Imm., dep.	Asian Dust (dry, polydisp.)
Niemand (2012)	224 to 251 K	Imm., dep.	Saharan Dust (dry, polydisp.)
This work	240 to 264 K	Imm., dep.	Diatomite (dry, polydisp.)

Table 4.11 lists several laboratory studies that have investigated the influence of secondary organic compounds produced from α-pinene on the ice nucleation properties of mineral dusts.

A decreased deposition nucleation efficiency was reported from cloud chamber experiments with illite and ATD particles after treatment with secondary organic compounds (Möhler et al., 2008a). The uncoated dust particles almost activated completely at relative humidities between RH_{ice} = 105% and RH_{ice} = 120% whereas coating with SOA led to a reduction of the ice fractions to less than 20% for ATD and to less than 10% for illite. Also, these ice fractions were only reached at much higher relative humidities with up to RH_{ice} = 130% for ATD and RH_{ice} = 170% for illite. These findings are supported by deposition nucleation measurements of coated mineral dust particles (Asian Dust, Saharan Dust) for which the observed ice fractions were lower than for uncoated dust particles

(Niemand, 2012). Note that for immersion freezing, the impact of organic coating on the ice nucleation efficiency seems to be ambiguous (Niemand, 2012). Monodisperse sub-micron ATD particles with organic coatings were also investigated by Koehler et al. (2010). Deposition nucleation initiated by coated ATD particles at temperatures below 233 K occured only for relative humidities close to the homogeneous freezing threshold.

Table 4.12: Overview of experiments investigating the effect of coatings with sulfuric acid on the ice nucleation properties of mineral dusts, clay minerals and mineral dust surrogates

Study	Temperature range	Ice nucl. modes	Core material
Archuleta et al. (2005)	213 to 228 K	Imm., dep.	Aluminium oxide (susp., monodisp.)
Archuleta et al. (2005)	213 to 228 K	Imm., dep.	Aluminium silicate (susp., monodisp.)
Archuleta et al. (2005)	213 to 228 K	Imm., dep.	Iron oxide (susp., monodisp.)
Knopf and Koop (2006)	197 to 260 K	Imm., dep.	ATD (suspension)
Eastwood et al. (2009)	233 to 246 K	Cond., dep.	Kaolinite (suspension)
Cziczo et al. (2009)	228 to 253 K	Imm., dep.	ATD (dry, polydisp.)
Cziczo et al. (2009)	228 to 253 K	Imm., dep.	Illite (dry, polydisp.)
Chernoff and Bertram (2010)	234 to 247 K	Dep.	Clay minerals (susp., polydisp.)
Chernoff and Bertram (2010)	234 to 247 K	Dep.	Quartz (susp., polydisp.)
Sullivan et al. (2010b)	243 K, 248 K	Cond., dep.	ATD (dry, d=300 nm)
Niedermeier et al. (2011a)	233 to 245 K	Imm.	ATD (dry, d=300 nm)
Niemand et al., unpublished	239 to 254 K	Imm., dep.	ATD (dry, polydisp.)
This work	220 to 253 K	Imm., dep.	SD2 (dry, polydisp.)
This work	220 to 253 K	Imm., dep.	ATD (dry, polydisp.)

An overview of experimental studies investigating the effect of sulfuric acid coatings on the ice nucleation properties of mineral dusts is given in Table 4.12.

Archuleta et al. (2005) used a continuous flow diffusion chamber to conduct experiments with aluminum oxide, alumina silicates and iron oxide particles coated with sulfuric acid. The change in ice nucleation activity with the coating strongly depended on the core material with only alumina silicates showing a reduction of the ice nucleation efficiency in most cases. The influence of sulfuric acid coatings on atmospherically more relevant particles was investigated by Eastwood et al. (2009). Kaolinite particles coated with sulfuric acid required higher relative humidities (ΔRH_{ice} up to 30%) for ice activation and at higher temperatures ($\sim$ 245 K), deposition nucleation was replaced by condensation

freezing. Sullivan et al. (2010b) and Niedermeier et al. (2011a) exposed monodisperse ATD particles to hot sulfuric acid vapor with the temperature of the hot sulfuric acid reservoir chosen to be either 318, 348 or 353 K and then tested their ice nucleation efficiencies. Observed ice fractions in the immersion freezing mode were smaller for acid coated particles only at temperatures above 237 K (Niedermeier et al., 2011a). A decreased condensation nucleation efficiency was also observed by Sullivan et al. (2010b). Surface modifications caused by exposure to the hot sulfuric acid vapor also caused a decreased deposition nucleation efficiency (Sullivan et al., 2010b). Cziczo et al. (2009) investigated acid coated illite and ATD particles and found more pronounced effects for ATD than for illite. For deposition nucleation initiated by coated dust particles higher relative humidities were required (ΔRH_{ice} up to 30 %) whereas at higher temperatures and for especially thick coatings immersion freezing could be completely suppressed. The effect of acid coatings on the deposition nucleation onsets observed for clay minerals (kaolinite, illite, montmorillionite) and quartz was investigated within a study by Chernoff and Bertram (2010). The required relative humidities at which ice nucleation occured were shifted by ΔRH_{ice} up to 30% for illite and kaolinite, and by ΔRH_{ice} up to 20% for montmorillionite and quartz. The previously described studies are in contradiction to experiments by Knopf and Koop (2006) which found a high variability in the ice nucleation onsets measured for uncoated ATD particles and therefore no clear impact of acidic coatings on the ice nucleation properties of ATD.

Coating procedure in the AIDA cloud chamber

As indicated in Tables 4.11 and 4.12, this work presents results from AIDA cloud chamber experiments with mineral dust aerosols having been coated with either sulfuric acid or secondary organics in order to investigate the influence of these treatments on the ice nucleation properties[10].

- For the experiments with secondary organics coating, α-pinene was converted into secondary organic compounds by ozonolysis after having added dry-dispersed mineral dust (diatomite) to the AIDA cloud chamber (Saathoff et al., 2009). The

[10] All coating experiments were conducted in close cooperation with H. Saathoff

products of the chemical reaction between α-pinene and ozone were then allowed to condense onto the mineral dust particles.

- In contrast to other studies which either used dust suspensions containing sulfuric acid or relied on coating by letting hot sulfuric acid vapor condense onto the particles, coating for the ice nucleation experiments presented in this work was achieved by exposing dry-dispersed dust particles to an environment within the AIDA cloud chamber where H_2SO_4 had been produced by oxidization of SO_2. SO_2 was oxidized by reacting with OH radicals which were generated from mixing ozone and tetramethylethylene (2,3-dimethyl-2-butene) (Atkinson and Aschmann, 1993). Sulfuric acid produced from this chemical reaction was then allowed to condense onto the mineral dust particles. The coating thickness could be varied by changing the concentrations of ozone, tetramethylethylene and SO_2. This particular coating procedure was chosen in order to avoid destruction of ice nucleation active sites by digestion through hot sulfuric acid. The "cold" coating procedure also more strongly resembles processes that occur in the atmosphere.

The effect of secondary organics was analyzed for immersion freezing and deposition nucleation experiments conducted with fossil diatomite which is assumed to be a component of windblown Saharan dust. Furthermore, in this section the results for ice nucleation experiments with sulfuric acid coated ATD and Saharan Dust particles are presented.

Deriving the INAS density values for coated particles

For all experiments the ice crystal concentrations were measured with the two optical particle counters welas and welas2. Additionally, the size distribution of the aerosol particles within the cloud chamber was measured in order to be able to estimate the aerosol surface. The ice nucleation active surface site density as a measure for the ice nucleation efficiency of each aerosol type is given by

$$n_s = \frac{n_{ice}}{A_{aer}} \; [\mathrm{m}^{-2}] \tag{4.19}$$

with the ice crystal concentration n_{ice} [cm^{-3}] and the aerosol surface area A_{aer} [$\mu\mathrm{m}^2\ \mathrm{cm}^{-3}$]. The measurement uncertainties are given by $\Delta n_{ice}/n_{ice} \approx 25\%$ and $\Delta A_{aer}/A_{aer} \approx 25\%$ and amount to $\Delta n_s/n_s \approx 35\%$.

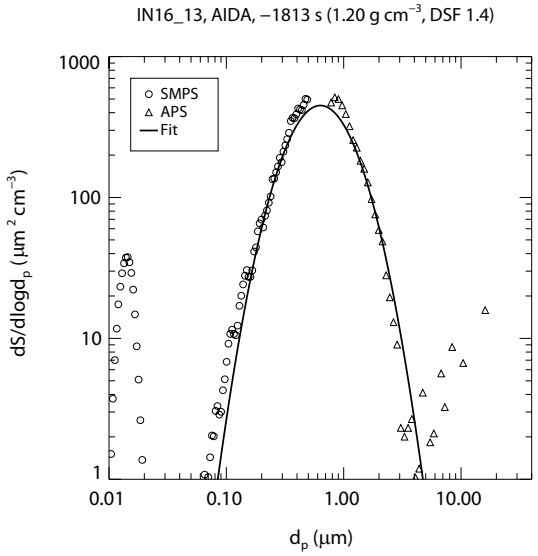

Figure 4.31: *Aerosol surface distribution for coated fossil diatom particles: the small particle size mode corresponds to particles nucleated from the organic phase whereas the larger mode represents the fossil diatom particles*

Figure 4.31 shows an examplary size distribution for SOA coated fossil diatom particles. A lognormal distribution is fitted to the measurements for calculating the total aerosol surface area from integrating the distribution. Figure 4.31 also shows that the size distribution is bi-modal: particles below 0.02 µm are most likely small nucleated organic particles whereas the mineral dust particles build the second mode at larger particle sizes. For calculating the INAS densities, only the dust mode is considered. The solution droplets are assumed not to participate in the freezing process because for most experiments, the relative humidities were too low for homogeneous ice nucleation.

4.5.1 Impact of SOA coating on the ice nucleation properties of diatoms

The effect of SOA coatings on the ice nucleation properties was investigated within a temperature range between 240 and 264 K (see Table 4.11). Ice nucleation active

surface site densities were derived both for immersion freezing and deposition nucleation experiments (Table 4.13).

Table 4.13: Overview of AIDA cloud chamber experiments with SOA coated diatom particles

Experiment	Coating thickness	Initial temp. [K]	Aerosol conc. [cm^{-3}]	Median diameter [µm]	Ice nucleation mode
IN16_07	5.7 nm	264	477	0.37	No ice
IN16_10	0.8 nm	253	539	0.32	Immersion freezing
IN16_13	0.4 nm	243	529	0.32	Deposition nucleation
IN16_15	6.4 nm	243	578	0.30	Deposition nucleation

Immersion freezing initiated by SOA coated diatom particles

Figure 4.32 shows ice nucleation active surface site (INAS) densities as derived from AIDA experiments with fossil diatoms and SOA coated diatomite particles. The INAS densities for fossil diatoms are extrapolated towards lower temperatures in order to be able to compare between the ice nucleation efficiencies of coated and uncoated fossil diatoms. Figure 4.32 also depicts the average INAS density for desert dusts as parameterized by Niemand et al. (2012). For coatings with secondary organics derived from α-pinene, the INAS density for one immersion freezing experiment is shown. The coating thickness as estimated from COSIMA calculations was approximately 1 nm assuming that the complete secondary organics yield was adsorbed to the surfaces of the diatom particles (Naumann, 2003)[11]. The ice nucleation efficiency of SOA coated diatoms was significantly lowered compared to uncoated diatoms. INAS densities were even lower than for desert dusts. For coatings thicker than 1 nm immersion freezing initiated by fossil diatoms was completely suppressed (see Table 4.13). This strong impact of SOA coating on the immersion freezing efficiency differs from recent findings regarding the INAS densities of SOA coated desert dust particles for which no significant change in ice nucleation efficiency was observed in comparison to the uncoated dust (Niemand, 2012).

[11] Estimates of the extent of the coating thickness for selected experiments with SOA and sulfuric acid were provided by K.-H. Naumann and H. Saathoff

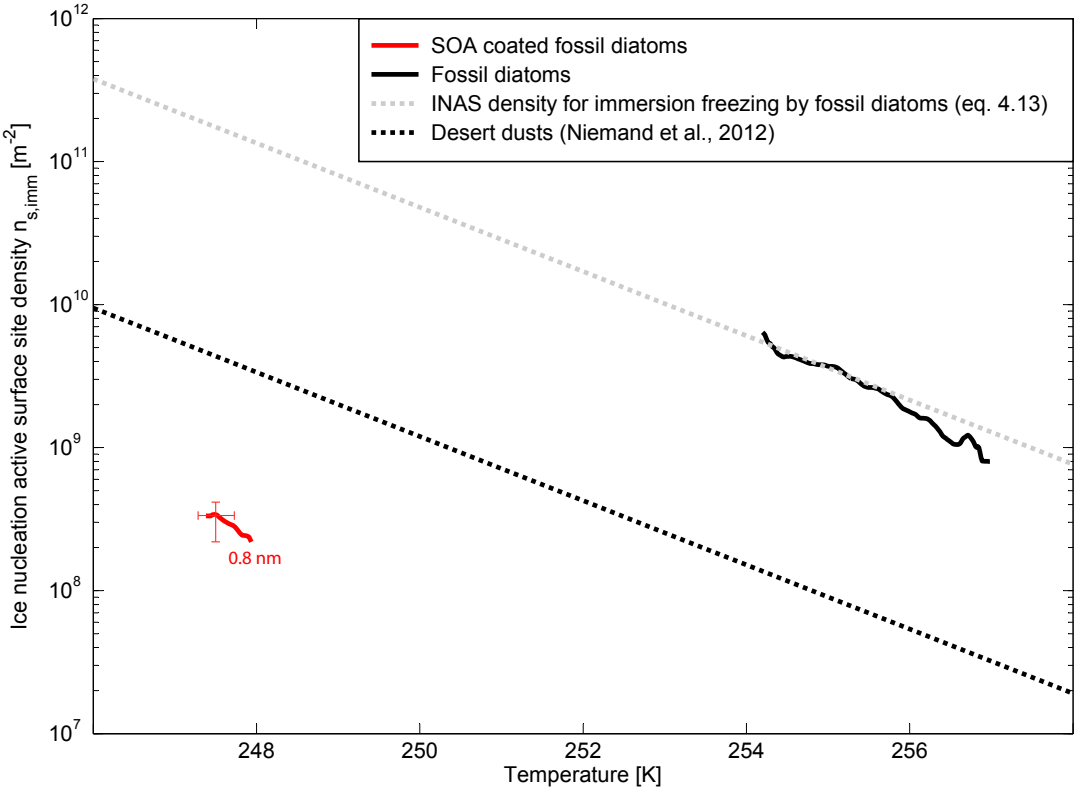

Figure 4.32: *Ice nucleation active surface site densities for immersion freezing initiated by fossil diatom particles with (–) and without secondary organics coating (–); for comparison the average INAS density for desert dusts is shown (- -)*

Deposition nucleation initiated by SOA coated diatom particles

INAS densities were also determined for deposition nucleation initiated by SOA coated fossil diatom particles. Figure 4.33 shows the ice nucleation active surface site densities for deposition nucleation initiated by fossil diatomite with and without SOA coating as a function of the thermodynamic variable $x_{therm}(T, S_{\mathrm{ice}})$ with T being the temperature and S_{ice} the relative humidity over ice. It can be concluded that the coating with secondary organics causes a shift of the ice nucleation onset (defined as $n_{s,dep} = 10^9$ m^{-2}) towards larger x_{therm} corresponding to higher relative humidities ($\Delta \mathrm{RH}_{\mathrm{ice}} \approx 15\%$). Increasing the coating thickness from 0.4 nm to 6.4 nm leads to a further shift of the ice nucleation onset by $\Delta x_{therm} \approx 2$. However, the INAS density values from the two experiments with different coating layer thickness are similar within the measurements uncertainties.

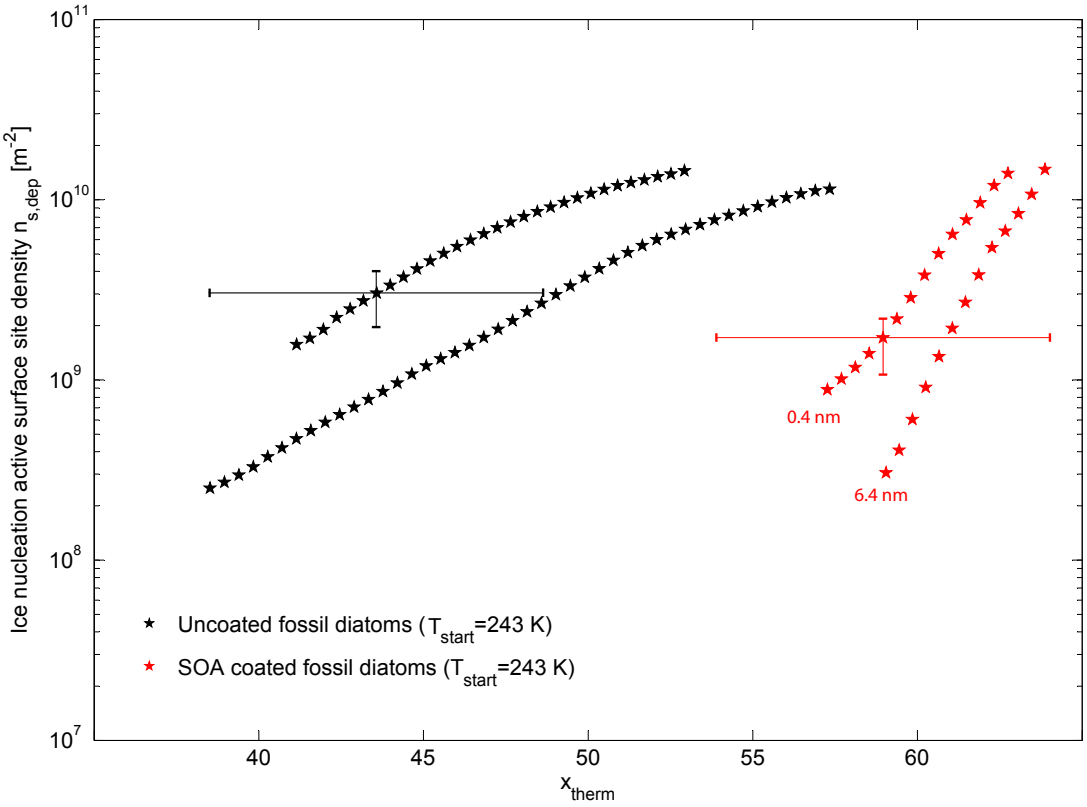

Figure 4.33: *Ice nucleation active surface site densities for deposition nucleation initiated by fossil diatom particles with secondary organics coating*

It should be noted that the average coating thickness is only a rough estimate. Additionally, because of the complex surface structure of the fossil diatom particles the aerosol surface area is supposedly underestimated by using the volume equivalent diameter of spherical particles. The surface structure of fossil diatoms might lead to incomplete coatings with only certain patches being covered by secondary organics. Additionally, the secondary organic compounds could be characterized by varying volatilities which would enhance the non-uniform coating effect.

4.5.2 Impact of "cold" coating with sulfuric acid on the ice nucleation properties of mineral dusts

Mineral dust particles with different mineralogical composition (Saharan Dust, Arizona Test Dust) were subjected to coatings with sulfuric acid. Different dust types were expected to react differently to the exposure to sulfuric acid vapor (see references in Table 4.12). Note that for the experiments in this work the sulfuric acid vapor was directly produced within the AIDA cloud chamber and therefore the coating took place at temperatures below 273 K.

Table 4.14: Overview of AIDA cloud chamber experiments with mineral dust particles exposed to OH radicals or with sulfuric acid coating; for experiments marked with an asterisk, the sulfuric acid coating was achieved by using hot sulfuric acid vapor (Niemand et al., unpublished)

Experiment	Aerosol (Coating thickness)	Initial temp. [K]	Aerosol conc. [cm^{-3}]	Median diameter [µm]	Ice nucleation mode
IN18_09	SD2 (medium)	250	481	0.30	Immersion freezing
IN15_28	ATD (thick)	253	891	0.24	Imm./Dep.
IN15_29	SD2 (thick)	253	477	0.42	Imm./Dep.
IN15_57	ATD (thick)	252	307	0.23	Imm./Dep.
IN15_62	ATD (thin)	253	577	0.26	Imm./Dep.
IN18_03	ATD (medium)	250	598	0.24	Imm./Dep.
IN18_02	ATD (OH radicals)	250	433	0.23	Imm./Dep.
IN18_07	ATD (thick)	241	524	0.24	Deposition nucleation
IN18_06	ATD (thin)	241	596	0.24	Deposition nucleation
IN18_08	ATD (medium)	241	800	0.26	Deposition nucleation
IN15_21	SD2 (thin)	243	381	0.40	Deposition nucleation
IN15_23	SD2 (thick)	243	341	0.39	Deposition nucleation
IN15_20	SD2 (medium)	243	441	0.43	Deposition nucleation
IN15_02	ATD (60 nm)	223	570	0.21	Deposition nucleation
IN15_08	ATD (3 nm)	223	447	0.22	Deposition nucleation
IN15_10	ATD (1 nm)	223	514	0.22	Deposition nucleation
IN15_14	SD2 (thin)	223	464	0.39	Deposition nucleation
IN15_18	SD2 (medium)	223	461	0.39	Deposition nucleation
IN18_04	ATD (OH radicals)	221	742	0.23	Deposition nucleation
IN08_26*	ATD(thick)	254	309	0.24/0.60	Immersion freezing
ACI02_25*	ATD(thin)	245	1333	0.20	Deposition nucleation
IN08_08*	ATD (thick)	241	185	0.20/0.52	Deposition nucleation

AIDA cloud chamber experiments investigating the impact of coatings with sulfuric acid on the ice nucleation properties of mineral dust particles are listed in Table 4.14. Note that for several experiments starting at approximately 250 K, immersion freezing and deposition nucleation initiated by coated dust particles were observed simultaneously. For these experiments, the contributions of the two ice nucleation modes could not be separated and therefore these experiments will be excluded from the following analyses. Note that at least for ATD in this temperature range generally deposition nucleation is preferred. However, the coating also changes the hygroscopic properties of the aerosol particles and presumably causes higher contributions by immersion/condensation freezing.

Immersion freezing initiated by sulfuric acid coated dust particles

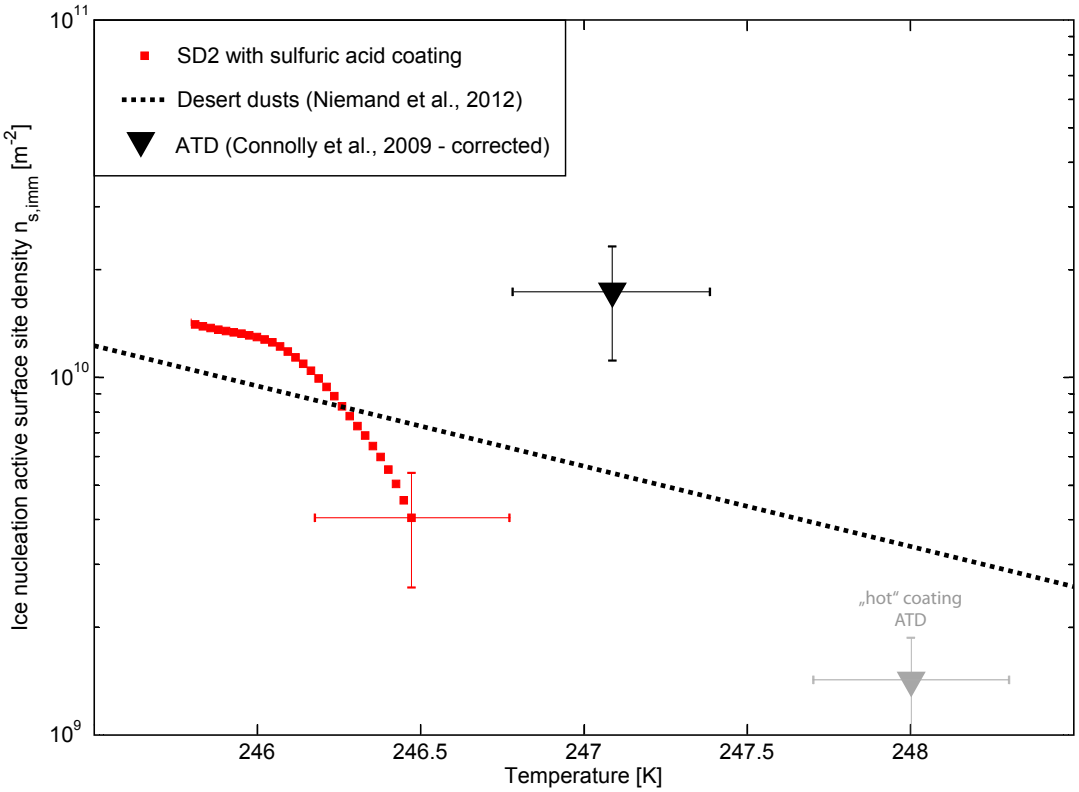

Figure 4.34: *Ice nucleation active surface site densities for immersion freezing by Saharan Dust (SD2) particles with sulfuric acid coating compared to the average INAS density observed for desert dusts; for comparison results for ATD particles with "hot" acid coating are shown*

Figure 4.34 shows the ice nucleation active surface site densities for immersion freezing initiated by Saharan Dust (SD2) particles treated with sulfuric acid. Additionally, the average INAS densities for immersion freezing of desert dusts are depicted (Niemand et al., 2012). For comparison, Fig. 4.34 also shows INAS densities for bare ATD particles (Connolly et al. (2009), corrected by a factor of 20 according to Niemand et al. (2012)) and ATD particles subjected to a treatment with hot sulfuric acid vapor (M. Niemand et al., unpublished data). For sulfuric acid coated Saharan Dust, the measured INAS density did not deviate largely from the average INAS density for uncoated desert dusts. However, with the ice nucleation efficiency of uncoated ATD particles being approximately one order of magnitude higher than for natural dusts, the treatment with hot sulfuric acid vapor resulted in a significant reduction of the observed ice nucleation efficiency. Thus, this observation can be taken as an indication that both coating methods might lead to diverging results concerning their influence on immersion freezing by mineral dust particles. However, the impact of the sulfuric acid coating was also observed to depend on the ambient temperature (Niedermeier et al., 2011a).

Deposition nucleation initiated by sulfuric acid coated dust particles

Experiments investigating the ice nucleation properties of sulfuric acid coated particles in deposition nucleation mode were conducted at the AIDA cloud chamber analogously to the immersion freezing experiments with acid coated dust particles.

Figure 4.35 shows the INAS densities observed for bare ATD particles and dust with varying coating thicknesses. The INAS densities are shown for two groups of expansion experiments starting either at T_{start} = 223 K (Fig. 4.35, left) or T_{start} = 241 K (Fig. 4.35, right). For T_{start} = 223 K only deposition nucleation was observed whereas at warmer temperatures T_{start} = 241 K, close to water saturation ice formation can be probably partly attributed to condensation freezing. Therefore, ice fractions observed for relative humidities shortly below water saturation are excluded from the analysis. For deposition nucleation at T_{start} = 223 K (Fig. 4.35, left), bare ATD particles already activate to ice crystals at very low supersaturations. For particles coated with sulfuric acid or subjected to a treatment with OH radicals, lower INAS densities are observed at considerably higher relative humidities over ice with ΔRH_{ice} up to 35%. For the measurements at higher

temperatures (T_{start} = 241 K), only INAS density values for coated particles are shown. The ice nucleation active surface site densities shown in Fig. 4.35 (left) were derived from experiments for which the SO_2 concentration (4 ppb, 20 ppb, 36 ppb) and thus the expected H_2SO_4 yield was varied. The observed INAS densities are consistently shifted towards higher relative humidities for thicker coatings.

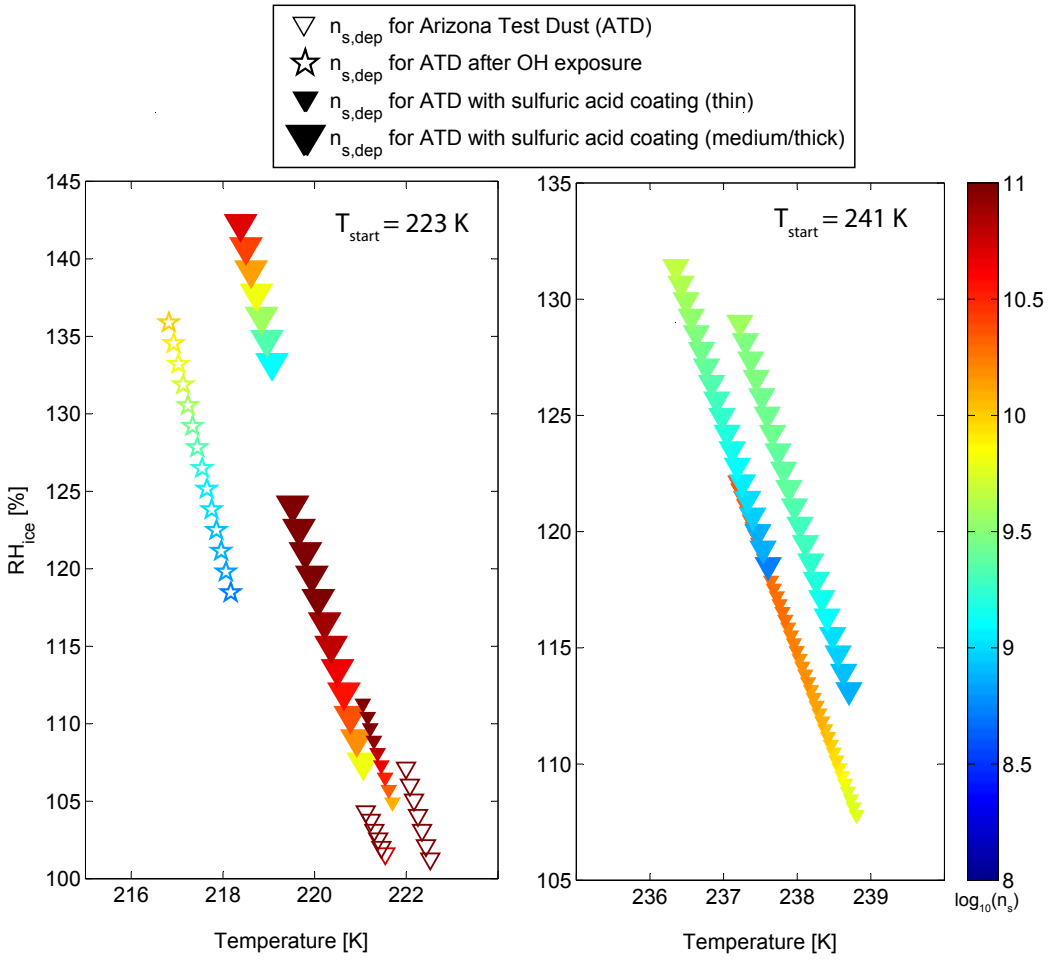

Figure 4.35: *Ice nucleation active surface site density values for deposition nucleation initiated by ATD particles with sulfuric acid coating for T_{start} = 223 K (left) and T_{start} = 241 K (right)*

Figure 4.36 shows a compilation of all INAS density values obtained for deposition nucleation experiments with sulfuric acid coated ATD particles and bare ATD particles. Additionally, INAS densities obtained for ice nucleation experiments with ATD particles having been exposed to hot sulfuric acid vapor are shown (M. Niemand, unpublished data). All ice nucleation active surface site densities are represented as a function of the thermodynamic variable x_{therm}.

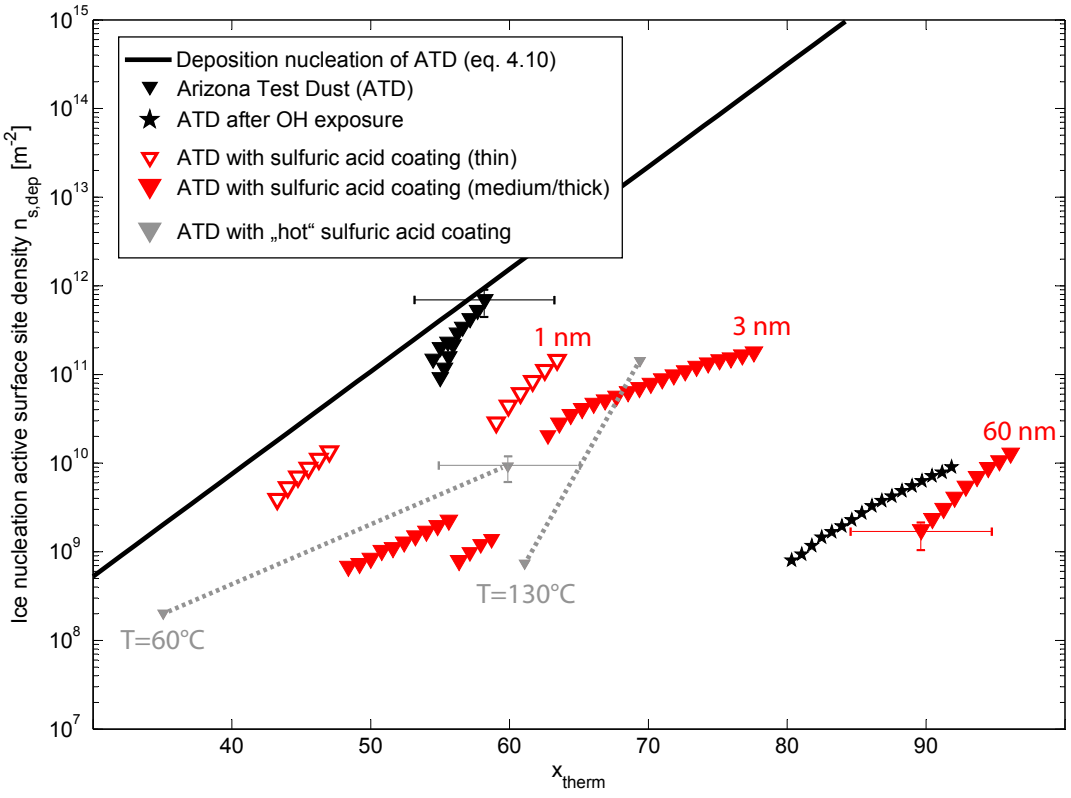

Figure 4.36: *Ice nucleation active surface site densities for deposition nucleation of ATD with sulfuric acid coating with varying coating layers; values obtained from experiments with "hot" sulfuric acid vapor are shown for comparison with the temperature of the sulfuric acid bath being indicated (M. Niemand, unpublished data)*

The coating causes a shift of the INAS densities towards larger values of x_{therm} for all experimental runs. For the experiments starting at 223 K, these shifts are correlated with the coating layer thickness with the thickest layer resulting in a shift $\Delta x_{therm} \approx 50$. The exposure to OH radicals without adding SO_2 also produces a significant deterioration of

the ice nucleation efficiency for deposition mode nucleation. This can be explained by the production of unknown chemical species which may be produced either from chemical reactions between contaminants in the AIDA cloud chamber or from heterogeneous reactions at the surface of the dust particles. Note, however, that for this specific experiment the expected OH radical yield was much higher than for the experiments with sulfuric acid production due to increased precursor concentrations (i.e. high TME and O_3 concentrations).

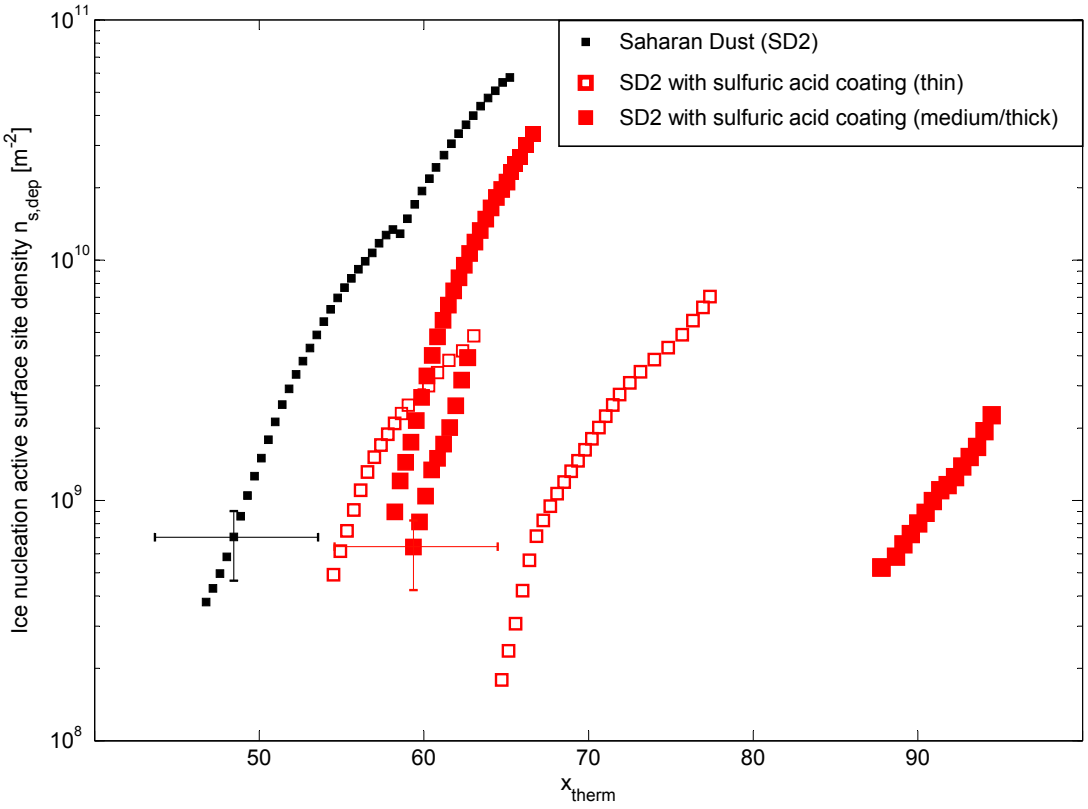

Figure 4.37: *Ice nucleation active surface site densities for deposition nucleation initiated by Saharan Dust particles with sulfuric acid coating; shown are also the INAS densities measured for uncoated Saharan Dust particles*

Figure 4.37 shows INAS density values obtained for deposition nucleation by bare and acid coated Saharan Dust (SD2) as a function of the thermodynamic variable x_{therm}. For Saharan Dust, the slope of the INAS densities is similar for all experiments. The INAS

density values at $x_{therm} \approx 55$ represent experiments which started at T_{start} = 232 K or T_{start} = 243 K, whereas the trajectories at higher x_{therm} values represent experiments at lower temperatures (T_{start} = 223 K). It can be observed from Fig. 4.37, that coating with sulfuric acid becomes especially relevant at temperatures below 223 K as the shift of the INAS densities for coated particles compared to the bare dust is most evident. For deposition nucleation at higher temperatures, the reduction of the ice nucleation efficiency does not depend on the coating thickness as there is no difference observed for thin and medium/thick coatings.

From the ice nucleation experiments with sulfuric acid coated mineral dust particles, it can be concluded that the reduction of ice nucleation efficiency is most relevant for a decreased ice nucleation efficiency in the deposition nucleation mode. For Saharan Dust, the deterioration in the ice nucleation efficiency also depends on the ambient temperature within the AIDA cloud chamber. The observed reduction of the ice nucleation efficiency is proportional to the coating layer thickness for deposition mode nucleation initiated by ATD but not for Saharan Dust. It should be noted, however, that the estimated sulfuric acid layers should only be interpreted as rough estimates because the estimation of the coating thickness assumes that the SO_2 injected into the cloud chamber is completely converted into sulfuric acid coatings. However, the chamber walls might act as a sink for sulfuric acid vapor and also some unknown chemical species might be produced from contaminants in the cloud chamber.

4.5.3 Summary

Dust particles may acquire diverse coatings during long-range atmospheric transport. Among the most abundant chemical species in the atmosphere are sulfates and secondary organics. Therefore, the influence of coatings with sulfuric acid or secondary organics produced from α-pinene on the ice nucleation efficiency of mineral dust particles was investigated.

- Coatings with secondary organics derived from the oxidization of α-pinene were tested with regard to their influence on the ice nucleation properties of fossil di-

atoms. Secondary organics caused a deterioration of the ice nucleation efficiency both for immersion freezing and deposition nucleation. The INAS densities observed for coated particles were shifted towards higher relative humidities with ΔRH_{ice} up to 20%. This shift compares well with an increased humidity threshold (ΔRH_{ice} up to 20%) observed for SOA coated ATD particles (Möhler et al., 2008a). The complete suppression of ice nucleation below the experimental detection limit was only observed for immersion freezing. For immersion freezing, the reduction of the ice nucleation efficiency seems to depend on the dust composition as a reduction of ice nucleation efficiency was not observed for desert dusts (Möhler et al., 2008a; Niemand, 2012). Note that the diatom particles have a very porous structure which might be advantageous to the uptake of volatile compounds in comparison to the surface of dust particles. Also, the impact of the SOA coating depending on the mineral dust species might be due to a variation of the water-surface interaction depending on the surface atoms involved.

- Sulfuric acid coating only had a weak influence on the immersion mode nucleation efficiency when the coating was produced by oxidization of SO_2. In contrast, there are indications that coatings with hot sulfuric acid vapor may lead to an irreversible destruction of ice nucleation active sites which then causes a reduction of the ice nucleation efficiency (Niedermeier et al. (2011a); M. Niemand et al., unpublished). However, modelling studies suggest that in the presence of sulfuric acid, highly ordered water layers may form which even accelerate the formation of stable ice clusters (Yang et al., 2011).

  For deposition mode nucleation, it was found that the INAS densities are distinctly lower when particles are treated with sulfuric acid. This is in agreement with several other studies (Cziczo et al., 2009; Sullivan et al., 2010b; Eastwood et al., 2009). The reduction of the deposition nucleation efficiency of coated mineral dust particles can be expressed as a shift of the INAS density function towards larger values of x_{therm}. This shift, however, was found to depend on the core mineral and the coating thickness. The deterioration of the ice nucleation efficiency was more pronounced for ATD than for Saharan Dust. Similarly, Cziczo et al. (2009) found that the shift towards higher relative humidities was larger for ATD than

for illite. It was observed that thick coatings could lead to shift of the dominant ice nucleation mode from deposition nucleation to condensation freezing due to an improved water uptake by the dust particles (data not shown).

The coating thickness for some of the presented experiments was estimated by assuming that the coating precursors (α-pinene or SO_2) would be completely converted into the actual coating agent (SOA or sulfuric acid). However, contaminations within the cloud chamber, condensation at the chamber walls and the formation of nucleated particulates might interfer with this conversion. The coating thickness could also be estimated from cloud condensation nuclei measurements but these results will be presented in other studies (C. Oehm, unpublished). Note, however, that the heterogeneity of coatings was not investigated in this work but may influence the efficiency of ice nucleation suppression. Also, it has to be considered that the coating thickness might vary among particles of different sizes. Thus, the presented results can only be interpreted as an average for all coated particles of the investigated aerosol population.

From the experimental results, it can be concluded that coatings cause a reduction of the ice nucleation efficiency in the deposition nucleation mode and for SOA coatings also for immersion freezing. Also, the change in dust particle hygroscopicity with various coatings and thus shifts from deposition nucleation to condensation freezing might be relevant under atmospheric conditions. Concerning atmospheric implications of coated particles, a modelling study investigating Arctic clouds suggests that mineral dust particles with sulfuric acid coating may have a significant influence on cloud microstructure and radiation over the Central Arctic (Girard et al., 2013).

4.6 First results from immersion freezing studies with a cold stage setup

The characteristics that an atmospheric particle must possess to initiate the formation of ice efficienctly are still under debate. Cracks, trenches and other surface irregularities are suspected to lower the energy barrier that must be overcome in order to form stable ice clusters (Roberts and Hallett, 1969). Molecular dynamics simulations investigating heterogeneous ice nucleation at surfaces with different properties suggest that there is a strong attractive interaction between surface atoms and water molecules within trenches of 10 – 100 nm width (Croteau et al., 2010). This interaction might aid the formation of stable ice clusters and thus it could accelerate the ice formation at "rugged" surfaces in comparison to smooth surfaces.

The cold stage setup was used to simulate immersion freezing under very controlled experimental conditions. Droplet freezing was investigated for several materials ranging from monocrystalline surfaces to structured silicon wafers ("artificial" ice nuclei). Also, suspensions containing feldspar particles were investigated with regard to their immersion freezing properties. For all experiments, measurements at different cooling rates from 0.2 K/min to 8 K/min were conducted in order to determine the freezing curves. The observed freezing curves were then analyzed by calculating the ice nucleation active surface site densities. For most experiments, the ice nucleation efficiency did not vary much for changing cooling rates. Therefore, the time dependence of the observed freezing processes is presumably small.

4.6.1 Ice nucleation at surfaces with "simple" structures[12]

Average ice nucleation surface site densities n_s with $n_s = f_{ice}/A$ were calculated from combining the measured freezing curves (f_{ice}) with estimates of the droplet-surface contact areas A which were derived from side-view images of water droplets placed onto the individual substrates. For the contact area A the measurement uncertainty is estimated to

[12] Measurements presented in this section were carried out by M. Haarig.

be at least $\Delta A/A \approx 30\%$. The uncertainty with regard to the detection of frozen droplets is mainly determined by the optical contrast between the water droplets and the individual substrates. The measurement uncertainty of the number fraction of frozen droplets f_{ice} can be as high as $\Delta f_{ice}/f_{ice} \approx 40\%$. Thus, the ice nucleation active surface site densities are associated with a maximum uncertainty $\Delta n_s/n_s \approx 50\%$. The measured INAS densities are averaged over several freeze-thaw cycles as described in Haarig (2013).

Figure 4.38 (taken from Haarig (2013)) shows average INAS densities observed for copper, muscovite and graphite. For comparison, INAS density values for mineral dust from desert areas (Niemand et al., 2012), soil dusts enriched in organic matter (this work), hematite (Hiranuma et al., 2013) and illite (Broadley et al., 2012) are additionally depicted in Fig. 4.38.

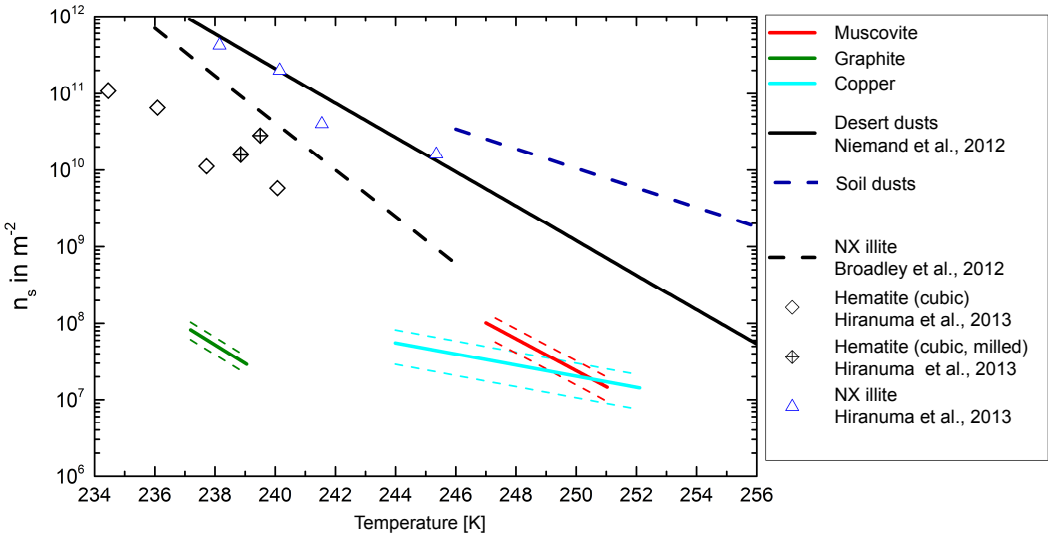

Figure 4.38: *Ice nucleation active surface site densities measured for copper, graphite and muscovite compared to values obtained for atmospherically relevant mineral dusts and clay minerals (taken from Haarig (2013))*

Ice nucleation for graphite is observed at temperatures near the homogeneous freezing regime, whereas copper and muscovite initiate the freezing of water droplets at around 251 K. The average roughness values as determined from Atomic Force Microscopy measurements vary considerably. Graphite ($R_a \approx 10$ nm) and muscovite ($R_a \approx 2$ nm) are much smoother than copper ($R_a \approx 800$ nm) (Haarig, 2013). Note that the average roughness

values can only be derived for a 400 μm^2 domain due to technical restrictions and thus may vary over the total substrate areas. However, muscovite and copper are similarly ice-active despite different roughness values which means that ice nucleation efficiency and roughness values are not strictly correlated for these two materials.

The observed INAS densities for graphite, copper and muscovite are much lower than INAS densities derived for aerosols with a more complex chemical composition and surface morphology such as desert dusts. Note that even commercially available mineral samples such as the NX illite sample contain contaminations with other mineral species such as quartz and cannot be considered as pure minerals. In contrast, hematite particles are regularly shaped iron oxide particles with only small deviations from the average cubic form. Hematite appears to be a less efficient ice nucleus than many natural dusts (Hiranuma et al., 2013) but still more efficient than graphite in the same temperature range. The ice nucleation efficiency of hematite can be enhanced by changing its surface morphology by intense physical treatment (milling) (Hiranuma et al., 2013). These observations can be taken as an indication that the surface morphology as well as the chemical composition at determine the ice nucleation characteristics of atmospheric aerosol particles.

4.6.2 Simulating immersion freezing at artificial ice nucleus structures

Within a previous study (Haarig, 2013) it was found that commercially available silicon wafers cleaned with acetone and purified water do not majorly influence the freezing properties of small water droplets (d = 90 µm). Water droplets placed onto silicon wafers froze close to the homogeneous freezing limit except a small droplet fraction that froze due to surface defects or contaminants on the silicon wafers. Therefore, silicon wafers were used to simulate the influence of morphology on the freezing properties of water droplets.
In cooperation with the "Karlsruhe Nano Micro Facility", structured silicon wafers were manufactured with trenches simulating the morphology of aerosol particles. The structures consist of trenches which are either 10 or 100 µm apart from each other. Each trench is 1 µm wide and 1 µm deep as indicated in the sketch in Fig. 4.39.

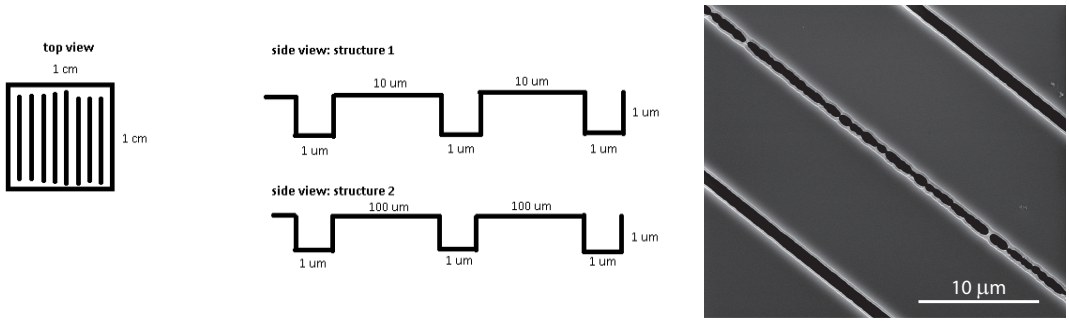

Figure 4.39: *Sketch of the structures applied to silicon wafers by dry etching - not to scale (left); ESEM image of silicon wafer with trenches (image: courtesy of A. Kiselev)*

The structures depicted in Fig. 4.39 were produced by dry etching. For dry etching, a polymer coating is applied to the silicon wafers and only destroyed where the reactive gas (SF_6) is supposed to etch away the first layers of silicon and silicon oxide at the surface of the silicon wafer. The gas reacts with the uncovered areas to create trenches with very vertical and smooth side walls. Later on, the polymer coating is removed again, leaving behind a silicon surface with the engineered structures. Figure 4.39 also shows an microscope image of the trenches etched into silicon wafers.

Silicon wafers with different geometries (i.e., distances of a = 10 µm or a = 100 µm between the trenches) were investigated with regard to their capability to initiate the freezing of water droplets. The silicon wafers were cleaned with acetone and purified water. An array consisting of small water droplets (d = 90 µm) was printed onto the structured wafers and freezing was investigated at different cooling rates. Note that to suppress evaporation, the droplets were covered with silicone oil which is assumed not to have an influence on the observed freezing behavior.

Results from repeated freeze-thaw cycles with two different wafers are shown in Fig. 4.40. Note that the freezing curve for water droplets on silicon wafers without trenches was taken from the study by Haarig (2013). The shaded area in Fig. 4.40 indicates the part of the freezing curve which might be impacted by heterogeneous freezing of surface irregularities or contaminants (e.g. residuals from the cleaning process). For the structured wafers, residuals from the etching process or incomplete etching might influence the observed freezing behaviour.

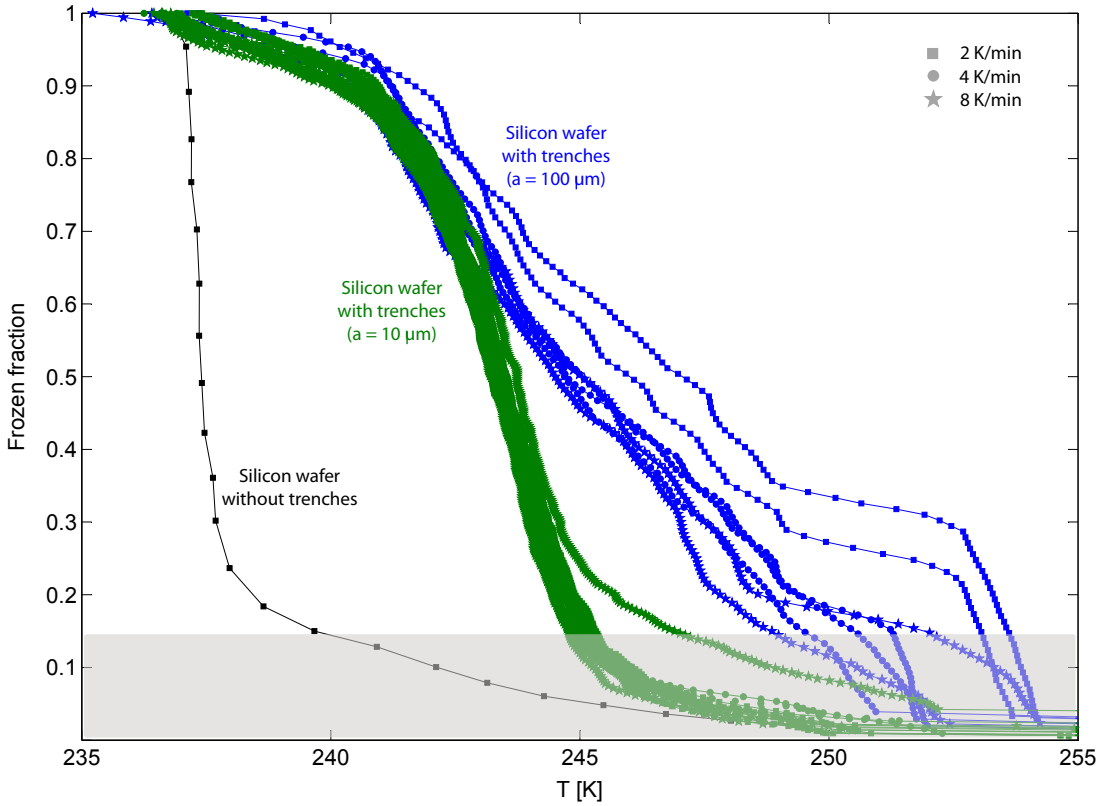

Figure 4.40: *Fraction of frozen droplets for structured silicon wafers with a = 10 µm (green symbols) and a = 100 µm (blue symbols) compared to the freezing curve observed for droplet freezing on pure silicon wafers; a is the distance between the trenches etched into the silicon wafer surface - grey shading indicates possible contributions by heterogeneous freezing caused by contaminants*

In comparison to the freezing of water droplets on pure silicon wafers, Fig. 4.40 shows that for both geometries the freezing curves are shifted towards higher temperatures. The median freezing temperatures for the droplets placed on a structured silicon surface are shifted to T_{10} = 243 K and T_{100} = 245 K. Freezing curves observed for the wafer with a smaller distance between the trenches are not strongly cooling rate dependent within the temperature uncertainty ΔT = 0.2 K. The measurement uncertainty of the ice fractions observed for freezing of water droplets on silicon was determined in the study by Haarig (2013) as $\Delta f_{ice}/f_{ice} \approx 20\%$. For the wafer with a larger distance between the trenches a tendency of freezing being shifted towards higher temperatures for low cooling rates is observed. This observation is in agreement with the notion that freezing should be time dependent due to the stochasticity of heterogeneous ice nucleation (Pruppacher and

Klett, 1997).

For the wafer with a smaller distance between the trenches, a single droplet will always be influenced by several trenches whereas for the wafers with larger distances, a single droplet will only be impacted by approximately one trench. The multiple droplet-trench interaction probably explains why the freezing curves observed for the wafer with a = 10 µm are much more similar to each other than the experimental runs investigating the wafer with a = 100 µm where the droplet-trench interaction might be more dependent on the local freezing conditions. Also, it cannot be excluded that the manufacturing process led to differences with regard to the quality of the etched structures.
However, the freezing curves observed for the two wafers cannot be explained so far. If the trenches directly facilitated the formation of ice clusters, a smaller distance between the trenches leading to more trenches influencing the individual droplets, would cause the freezing curve to be shifted towards warmer temperatures compared to the geometry with a = 100 µm. This hypothesis, however, is refuted by the observed freezing curves. Note, however, that for the wafers with a = 100 µm only about 100 droplets were investigated due to a larger interdroplet distance (reducing the number of droplets per sample) and a worse-than-average contrast between wafer and droplets was rendering the optical detection of droplets difficult.

4.6.3 Immersion freezing of feldspar suspensions

For relating the freezing behaviour of droplets placed on artificial surface structures to the ice nucleation efficiency of atmospheric aerosol particles, suspensions containing very small amounts of natural mineral dust particles were investigated. Feldspar particles were identified as very efficient ice nuclei initiating immersion freezing at 255 K (Atkinson et al., 2013).
Cold stage measurements were conducted with feldspar particles[13] by suspending 3 mg into 300 ml of nano-pure water (w = 0.001%). The feldspar suspension was filtered to remove particles larger than 200 nm. ESEM measurements investigating feldspar

[13]The feldspar sample was provided by M. Ebert (Technical University of Darmstadt).

suspension droplets with a larger amount of feldspar (w = 0.8%) found several thousand particles per droplet with many particles having a diameter around 200 nm (Hoffmann, unpublished).

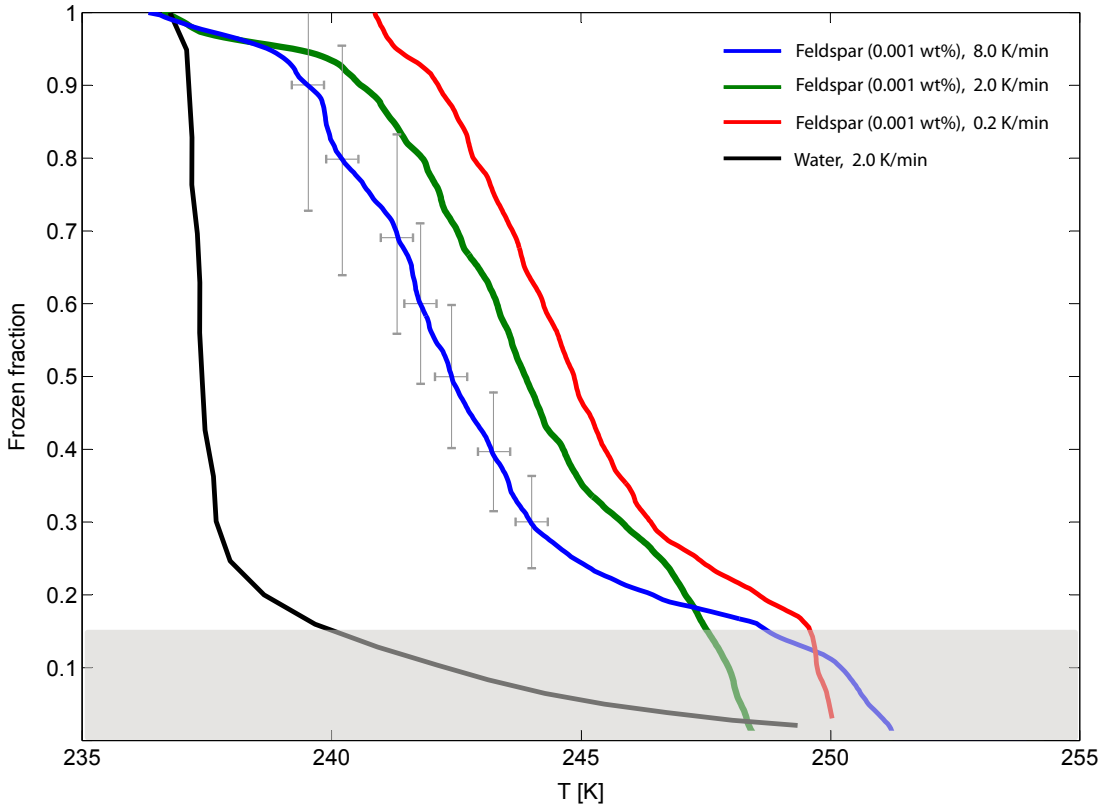

Figure 4.41: *Immersion freezing of feldspar suspension droplets compared to freezing of pure water droplets on silicon wafers - grey shading indicates possible contributions by heterogeneous freezing caused by contaminants*

Figure 4.41 shows the freezing curves obtained for droplets of feldspar suspensions. For comparison, the freezing curve obtained for pure water droplets on silicon is shown (taken from Haarig (2013)). The measurement uncertainties are assumed to be similar to the values obtained for freezing studies with water droplets on silicon with ΔT = 0.2 K and $\Delta f_{ice}/f_{ice} \approx 20\%$. In Fig. 4.41 ice fractions up to f_{ice} = 15% are shaded to indicate the possible contribution of contaminants to the observed droplet freezing at low ice fractions. From Fig. 4.41 it can be observed that the feldspar suspensions initiate immersion freezing at about 250 K. The ice fractions also depend on the cooling rate and thus slightly time

dependent. The median freezing temperature is shifted by approximately by ΔT = 2 K towards lower temperatures when the cooling rates is increased from 0.2 to 8.0 K/min. This finding agrees well with a study by Welti et al. (2012) investigating immersion freezing by size selected kaolinite particles for which a shift of ΔT = 1 K for an increase of the cooling rate by one order of magnitude was observed. The shift in the median temperature observed for feldspar suspensions is also in the range of temperature shifts observed for montmorillionite and kaolinite in a similar experimental setup with $\Delta T_{kao,mon}$ = 2.7 K over two orders of magnitude in cooling rates (Wright et al., 2013 (submitted)). Note, however, that for an exact quantification of the time dependence observed for immersion freezing initiated by feldspar particles more experimental runs would be needed.

4.6.4 Summary

To compare the ice nucleation efficiency observed for feldspar to results obtained for copper, graphite and muscovite as well as to the droplet freezing efficiency of the structured wafers, ice nucleation active surface site densities were calculated.

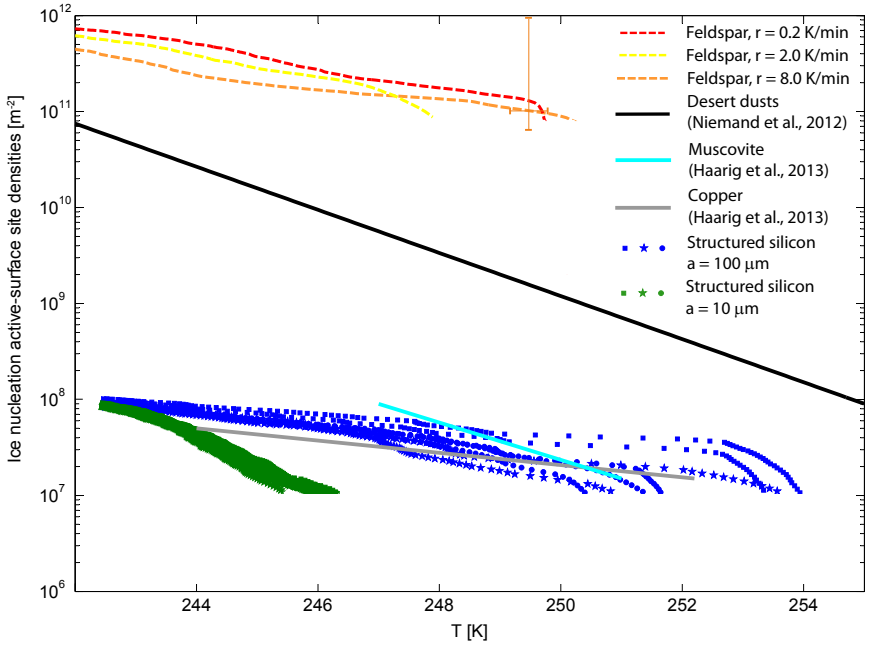

Figure 4.42: *Ice nucleation active surface site densities as derived from immersion freezing experiments carried out with the cold stage setup in comparison to desert dust INAS densities*

The INAS densities for the materials discussed in the previous sections are shown in Fig. 4.42. The INAS density values calculated for feldspar have to be treated as rough estimates because the aerosol surface area is not known. From ESEM measurements investigating the feldspar content of water droplets produced from a feldspar suspension with $w = 0.8$ % it can be concluded that each droplet contains $1 - 10$ particles with the largest particles' diameters being around 200 nm (N. Hoffmann, unpublished). Thus, the maximum surface area is estimated as $A_{aer} = 1.26$ µm^2 with a resulting INAS density of $n_s \approx 7 \cdot 10^{10}$ m^{-2} at 250 K. The ice nucleation properties of sodium-rich feldspar were also investigated by Atkinson et al. (2013) with INAS densities for feldspar of $n_s = 2 \cdot 10^9$ m^{-2} at 250 K. This INAS density value is by a factor 35 smaller than results from the cold stage measurements. However, caution has to be applied when comparing these INAS density values directly because the per-droplet aerosol surface of the feldspar particles investigated with the cold stage setup is not very well confined. Furthermore, Atkinson et al. (2013) used a different method (i.e. BET analysis) to determine the aerosol surface. It has been observed that these two methods (BET vs. geometric surface) might differ by at least one order of magnitude (see references in Murray et al. (2012)).
Nevertheless, feldspar particles appear to be much more ice-active than desert dusts for which the ice nucleation efficiency can be predicted by using the parameterization developed by Niemand et al. (2012).

For the structured wafers, the contact area between droplets and the silicon wafer is assumed to be the same as for the untreated silicon wafers with $A_{aer} = 8000$ µm^2. Applying trenches to silicon wafers causes a shift from homogeneous freezing to heterogeneous ice nucleation. However, the ice nucleation active surface site densities observed for structured wafers are still several orders of magnitude smaller than the values predicted for desert dusts. Similarly, materials such as copper or muscovite are much less ice-active than natural desert dusts.

Chapter 5

Summary and outlook

Dust particles may have a significant influence on global climate because they are abundant in the atmosphere and interact with clouds in manifold ways, e.g. by initiating the formation of ice crystals. Mineral dust particles and clay minerals have been identified as efficient ice nuclei over a wide range of temperature and humidity conditions (Murray et al., 2012).

AIDA cloud chamber experiments were used to investigate the ice nucleation properties of several atmospherically relevant mineral dusts such as fossil diatomite, volcanic ash and agricultural soil dusts. The influence of surface coatings with secondary organic compounds or sulfuric acid on the ice nucleation efficiency of mineral dust was also investigated.
Using cloud chamber experiments with Arizona Test Dust (ATD) as a basis, the time dependence of deposition mode nucleation was quantified and investigated under various atmospheric conditions (e.g. varying updraft velocities) by simulating the ascent of air parcels with the box model ACPIM.
Complementing the AIDA cloud chamber experiments, droplet freezing experiments were used to learn more about the freezing capabilities of monocrystalline surfaces, surfaces with prescribed morphologies ("artificial" ice nuclei) and feldspar suspensions.

From these experimental studies the following conclusions can be drawn:

- Deposition nucleation experiments with ATD were conducted at various cooling rates and aerosol number concentrations. The ice nucleation active surface site (INAS) density values were found to depend not only on the relative humidity over ice but also on the ambient temperature. Thus, between 220 and 253 K, for all experiments the INAS density values can be best described as a function of the thermodynamic variable x_{therm}. This variable x_{therm} is best approximated by a linear combination of temperature and relative humidity. This x_{therm} metric was then also applied to the deposition nucleation efficiencies of desert dusts and clay minerals in order to develop an INAS density parameterization for deposition nucleation. Classical nucleation theory was also used to represent the ice nucleation efficiency of ATD particles by a distribution of contact angles. However, it was found that the uncertainty with regard to the derived contact angle distribution parameters is very large because the contact angle distributions cannot always be fitted unambiguously which increases the range of possible parameter combinations.
  The AIDA cloud chamber experiments were also used to investigate the time dependence of deposition nucleation initiated by ATD particles. The time dependence was found to be very small and - according to model calculations - only relevant at low cooling rates.

- Fossil diatom particles which might contribute significantly to dust emissions from the Sahara desert are much more ice-active than desert dusts in the immersion freezing and the deposition nucleation mode.

- Volcanic ash from the Eyjafjallajökull eruption in 2010 mainly consists of alumina silicates like common desert dusts but it is, in comparison to desert dusts, slightly less ice-active with regard to initiating immersion freezing and deposition nucleation.

- Soil dusts containing large amounts of organic matter are very active ice nuclei, especially at temperatures above 250 K. The ice nucleation efficiency of soil dust from Argentina could not be reduced by extensive treatments with heat or irradiation which damage or destroy viable organism and protein structures. The observed ice nucleation efficiency was apparently neither connected to the biological activ-

ity nor the viability of the soil organisms. The increased ice nucleation efficiency compared to desert dusts might be caused by an enrichment in stabilized organic matter, e.g. organo-clay mineral complexes or mineral dust particles coated with organic substances.

- Coatings with secondary organic compounds, however, caused a reduction of the ice nucleation efficiency of fossil diatoms in both ice nucleation modes (immersion freezing and deposition nucleation). For immersion freezing even a total suppression of ice formation below the measurement sensitivity threshold was observed.

- For coatings with sulfuric acid, the immersion freezing efficiency was mostly not influenced whereas for deposition nucleation a reduction of the ice nucleation active surface site densities was observed for Saharan Dust and Arizona Test Dust. In contrast, using hot sulfuric acid for coating ATD particles significantly reduced the immersion freezing efficiency.

- Immersion freezing studies conducted with the cold stage setup revealed that materials such as muscovite, graphite and copper were very much less ice-active than desert dusts with more complex physico-chemical properties. Even muscovite which was assumed to be similar to atmospheric dust particles proved to be less ice-active. Freezing of water droplets on silicon wafers was shifted from homogeneous nucleation to immersion freezing when artificial morphologies (trenches) were applied to the silicon wafers. Nevertheless, the ice nucleation efficiency of the structured wafers expressed as ice nucleation active surface site densities was still lower than for natural dust particles. The cold stage was also used to investigate feldspar suspensions which were much more ice-active than desert dust particles.

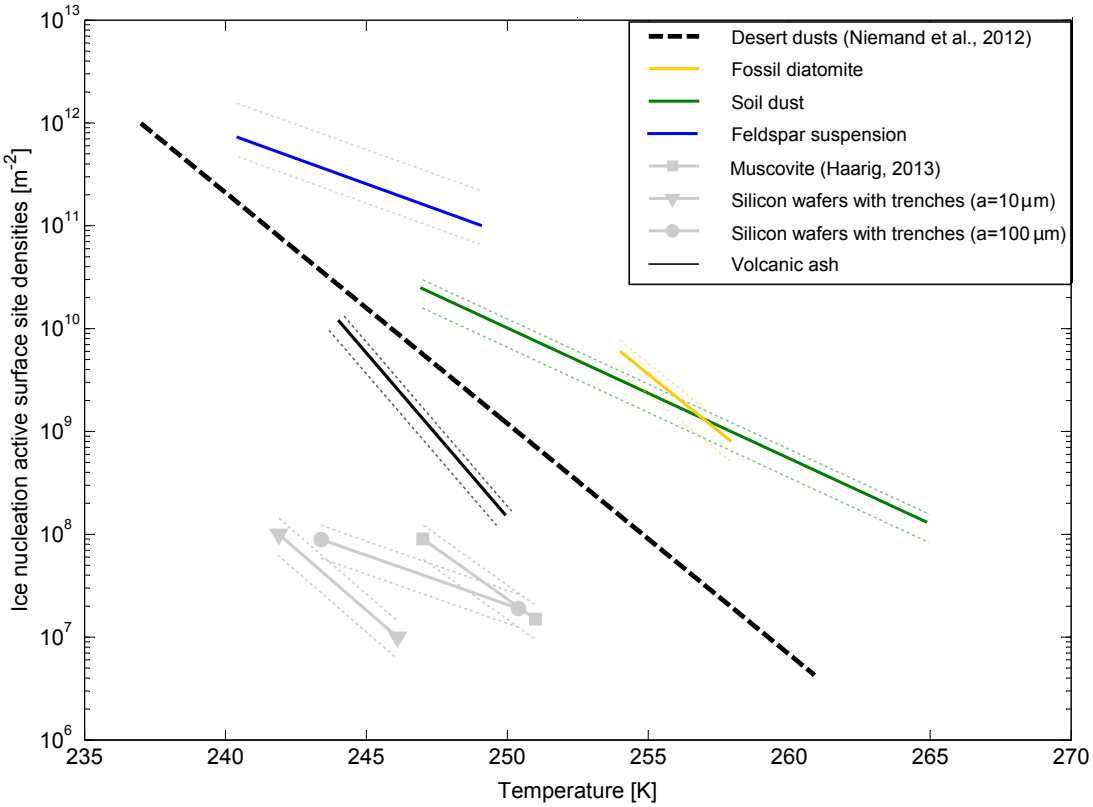

Figure 5.1: *Overview of ice nucleation active surface site densities obtained from immersion freezing experiments within this thesis project*

Figure 5.1 shows an overview of ice nucleation active surface site densities measured for different mineral dusts and mineral dust surrogates. For comparison, the INAS density for immersion freezing by desert dusts is also depicted (Niemand et al., 2012). Feldspar particles, fossil diatoms and soil dusts enriched in organic compounds were found to be significantly more ice-active than desert dusts. The fossil diatoms were similarly ice-active than the soil dust particles when comparing the INAS density values. Volcanic ash was only slightly less ice-active than desert dusts. First steps towards a better understanding of heterogeneous ice nucleation processes were made by investigating muscovite surfaces (Haarig, 2013) and silicon wafers with artificial morphologies. However, these materials were still much less ice-active than mineral dust particles even though the application of artificial morphologies at least caused a shift from homogeneous nucleation to immersion

freezing.

The ice nuclei concentration estimated for soil dust particles were of the same order of magnitude as the ice nuclei numbers derived from the atmospheric concentrations of desert dust. Thus, soil dust particles carrying micro-organism and organic matter may have at least a regional impact on atmospheric ice nucleation. Volcanic ash particles are emitted sporadically with very high particle concentrations. Thus, even though they are slightly less efficient than desert dusts, they might act as atmosperic ice nuclei like the particles from desert dusts and agricultural areas. The fossil diatomite particles are potentially very ice-active but have not been identified as very frequent ice nucleators in the atmosphere.

From the ice nucleation studies within this projects, several new research questions arise:

- The enhanced ice nucleation efficiency observed for soil dust particles is still not completely understood. The mineralogy as well as the stable organic compounds should be investigated further in order to gain a better understanding of the influence that these components have on the overall ice nucleation efficiency. Also, the impact of soil dust particles on ice nucleation in clouds could be estimated by using regional models such as COSMO-ART.

- Stable (i.e. heat resistant) organic compounds such as complex carbohydrates are suspected to contribute to the enhanced ice nucleation efficiencies of soil dusts. Solution droplets containing carbohydrates such as glucose, galactose or pectin could be easily investigated with the cold stage setup. Other soil components that could initiate the formation of ice are phytoliths which are mineralized plant residuals which can be extracted from leafs by using a household microwave. These phytoliths could be investigated either in the AIDA cloud chamber or with droplet freezing experiments.

- The huge difference between the ice nucleation capabilities of mineral dust surrogates such as muscovite or structured silicon wafers and natural aerosol particles also remains unexplained. Further cold stage experiments with more advanced

structures such as smaller trenches or small holes with different geometries may point towards possible explanations. Additionally, molecular dynamics simulations investigating the clustering of water molecules in the presence of different surface geometries could provide further insights into the microphysical processes relevant for heterogeneous ice nucleation.

- Deposition nucleation initiated by ATD particles could be investigated over a wider temperature range than presented in this study in order to better define the temperature and humidity dependent variable x_{therm}. Additionally, the deposition nucleation efficiency of atmospherically relevant particles such as wind-blown mineral dusts, soot or biological particles should be investigated over a wide range of thermodynamic conditions in order to quantify the temperature dependence of deposition nucleation for these aerosols. The temperature dependence could then be incorporated in aerosol dependent x_{therm} formulations.

Bibliography

R. Al-Naimi and C. P. R. Saunders. Measurements of natural deposition and condensation-freezing ice nuclei with a continuous flow chamber. *Atmospheric Environment (1967)*, 19(11):1871–1882, 1985. doi: 10.1016/0004-6981(85)90012-5.

B. A. Albrecht. Aerosols, cloud microphysics, and fractional cloudiness. *Science*, 245 (4923):1227–1230, 1989. doi: 10.1126/science.245.4923.1227.

P. A. Alpert, J. Y. Aller, and D. A. Knopf. Ice nucleation from aqueous NaCl droplets with and without marine diatoms. *Atmospheric Chemistry and Physics*, 11(12):5539–5555, 2011. doi: 10.5194/acp-11-5539-2011.

C. M. Archuleta, P. J. DeMott, and S. M. Kreidenweis. Ice nucleation by surrogates for atmospheric mineral dust and mineral dust/sulfate particles at cirrus temperatures. *Atmospheric Chemistry and Physics*, 5(10):2617–2634, 2005. doi: 10.5194/acp-5-2617-2005.

J. D. Atkinson, B. J. Murray, M. T. Woodhouse, T. F. Whale, K. J. Baustian, K. S. Carslaw, S. Dobbie, D. O'Sullivan, and T. L. Malkin. The importance of feldspar for ice nucleation by mineral dust in mixed-phase clouds. *Nature*, 498(7454):355–358, 2013. doi: 10.1038/nature12278.

R. Atkinson and S. M. Aschmann. Hydroxyl radical production from the gas-phase reactions of ozone with a series of alkenes under atmospheric conditions. *Environmental Science & Technology*, 27(7):1357–1363, 1993. doi: 10.1021/es00044a010.

M. Bangert, A. Nenes, B. Vogel, H. Vogel, D. Barahona, V. A. Karydis, P. Kumar, C. Kottmeier, and U. Blahak. Saharan dust event impacts on cloud formation and

radiation over Western Europe. *Atmospheric Chemistry and Physics*, 12(9):4045–4063, 2012. doi: 10.5194/acp-12-4045-2012.

D. Barahona. On the ice nucleation spectrum. *Atmospheric Chemistry and Physics*, 12 (8):3733–3752, 2012. doi: 10.5194/acp-12-3733-2012.

D. Barahona and A. Nenes. Parameterizing the competition between homogeneous and heterogeneous freezing in ice cloud formation - polydisperse ice nuclei. *Atmospheric Chemistry and Physics*, 9(16):5933–5948, 2009. doi: 10.5194/acp-9-5933-2009.

H. Bingemer, H. Klein, M. Ebert, W. Haunold, U. Bundke, T. Herrmann, K. Kandler, D. Müller-Ebert, S. Weinbruch, A. Judt, A. Wéber, B. Nillius, K. Ardon-Dryer, Z. Levin, and J. Curtius. Atmospheric ice nuclei in the Eyjafjallajökull volcanic ash plume. *Atmospheric Chemistry and Physics*, 12(2):857–867, 2012. doi: 10.5194/acp-12-857-2012.

R. M. Bowers, S. McLetchie, R. Knight, and N. Fierer. Spatial variability in airborne bacterial communities across land-use types and their relationship to the bacterial communities of potential source environments. *ISME Journal*, 5(4):601–612, 2011. doi: 10.1038/ismej.2010.167.

S. L. Broadley, B. J. Murray, R. J. Herbert, J. D. Atkinson, S. Dobbie, T. L. Malkin, E. Condliffe, and L. Neve. Immersion mode heterogeneous ice nucleation by an illite rich powder representative of atmospheric mineral dust. *Atmospheric Chemistry and Physics*, 12(1):287–307, 2012. doi: 10.5194/acp-12-287-2012.

F.-M. Bréon, D. Tanré, and S. Generoso. Aerosol Effect on Cloud Droplet Size Monitored from Satellite. *Science*, 295(5556):834–838, 2002. doi: 10.1126/science.1066434.

P. Capriel, T. Beck, H. Borchert, J. Gronholz, and G. Zachmann. Hydrophobicity of the organic matter in arable soils. *Soil Biology and Biochemistry*, 27(11):1453–1458, 1995. doi: 10.1016/0038-0717(95)00068-P.

J. Carrasco, A. Michaelides, M. Forster, S. Haq, R. Raval, and A. Hodgson. A one-dimensional ice structure built from pentagons. *Nature Materials*, 8(5):427–431, 2009. doi: 10.1038/nmat2403.

J.-P. Chen, A. Hazra, and Z. Levin. Parameterizing ice nucleation rates using contact angle and activation energy derived from laboratory data. *Atmospheric Chemistry and Physics*, 8(24):7431–7449, 2008. doi: 10.5194/acp-8-7431-2008.

C. Chenu and A. F. Plante. Clay-sized organo-mineral complexes in a cultivation chronosequence: revisiting the concept of the 'primary organo-mineral complex'. *European Journal of Soil Science*, 57(4):596–607, 2006. doi: 10.1111/j.1365-2389.2006.00834.x.

D. I. Chernoff and A. K. Bertram. Effects of sulfate coatings on the ice nucleation properties of a biological ice nucleus and several types of minerals. *Journal of Geophysical Research: Atmospheres*, 115(D20):D20205, 2010. doi: 10.1029/2010JD014254.

C. Chou, P. Formenti, M. Maille, P. Ausset, G. Helas, M. Harrison, and S. Osborne. Size distribution, shape, and composition of mineral dust aerosols collected during the African Monsoon Multidisciplinary Analysis Special Observation Period 0: Dust and Biomass-Burning Experiment field campaign in Niger, January 2006. *Journal of Geophysical Research: Atmospheres*, 113(D23):D00C10, 2008. doi: 10.1029/2008JD009897.

R. J. Cipriano and D. C. Blanchard. Bubble and aerosol spectra produced by a laboratory "breaking wave". *Journal of Geophysical Research: Oceans*, 86(C9):8085–8092, 1981. doi: 10.1029/JC086iC09p08085.

F. Conen, C. E. Morris, J. Leifeld, M. V. Yakutin, and C. Alewell. Biological residues define the ice nucleation properties of soil dust. *Atmospheric Chemistry and Physics*, 11(18):9643–9648, 2011. doi: 10.5194/acp-11-9643-2011.

P. J. Connolly, O. Möhler, P. R. Field, H. Saathoff, R. Burgess, T. Choularton, and M. Gallagher. Studies of heterogeneous freezing by three different desert dust samples. *Atmospheric Chemistry and Physics*, 9(8):2805–2824, 2009. doi: 10.5194/acp-9-2805-2009.

P. J. Connolly, C. Emersic, and P. R. Field. A laboratory investigation into the aggregation efficiency of small ice crystals. *Atmospheric Chemistry and Physics*, 12(4):2055–2076, 2012. doi: 10.5194/acp-12-2055-2012.

S. J. Cox, S. M. Kathmann, J. A. Purton, M. J. Gillan, and A. Michaelides. Non-hexagonal ice at hexagonal surfaces: the role of lattice mismatch. *Phys. Chem. Chem. Phys.*, 14 (22):7944–7949, 2012. doi: 10.1039/c2cp23438f.

S. J. Cox, Z. Raza, S. Kathmann, B. Slater, and A. Michaelides. The Microscopic Features of Heterogeneous Ice Nucleation May Affect the Macroscopic Morphology of Atmospheric Ice Crystals. *Faraday Discuss.*, 2013. doi: 10.1039/C3FD00059A.

T. Croteau, A. K. Bertram, and G. N. Patey. Observations of High-Density Ferroelectric Ordered Water in Kaolinite Trenches using Monte Carlo Simulations. *The Journal of Physical Chemistry A*, 114(32):8396–8405, 2010. doi: 10.1021/jp104643p.

J. A. Curry and V. I. Khvorostyanov. Assessment of some parameterizations of heterogeneous ice nucleation in cloud and climate models. *Atmospheric Chemistry and Physics*, 12(2):1151–1172, 2012. doi: 10.5194/acp-12-1151-2012.

D. J. Cziczo, K. D. Froyd, S. J. Gallavardin, O. Möhler, S. Benz, H. Saathoff, and D. M. Murphy. Deactivation of ice nuclei due to atmospherically relevant surface coatings. *Environmental Research Letters*, 4(4):044013, 2009. doi: 10.1088/1748-9326/4/4/044013.

G. de Leeuw, E. L. Andreas, M. D. Anguelova, C. W. Fairall, E. R. Lewis, C. O'Dowd, M. Schulz, and S. E. Schwartz. Production flux of sea spray aerosol. *Reviews of Geophysics*, 49(2):RG2001, 2011. doi: 10.1029/2010RG000349.

C. Dearden, P. J. Connolly, T. W. Choularton, and P. R. Field. Evaluating the effects of microphysical complexity in idealised simulations of trade wind cumulus using the Factorial Method. *Atmospheric Chemistry and Physics*, 11(6):2729–2746, 2011. doi: 10.5194/acp-11-2729-2011.

P. J. DeMott, D. J. Cziczo, A. J. Prenni, D. M. Murphy, S. M. Kreidenweis, D. S. Thomson, R. Borys, and D. C. Rogers. Measurements of the concentration and composition of nuclei for cirrus formation. *Proceedings of the National Academy of Sciences*, 100 (25):14655–14660, 2003. doi: 10.1073/pnas.2532677100.

P. J. DeMott, A. J. Prenni, X. Liu, S. M. Kreidenweis, M. D. Petters, C. H. Twohy, M. S. Richardson, T. Eidhammer, and D. C. Rogers. Predicting global atmospheric ice nuclei distributions and their impacts on climate. *Proceedings of the National Academy of Sciences*, 107(25):11217–11222, 2010. doi: 10.1073/pnas.0910818107.

V. R. Després, J. A. Huffman, S. M. Burrows, C. Hoose, A. S. Safatov, G. Buryak, J. Fröhlich-Nowoisky, W. Elbert, M. O. Andreae, U. Pöschl, and R. Jaenicke. Primary biological aerosol particles in the atmosphere: a review. *Tellus B*, 64:15598, 2012. doi: 10.3402/tellusb.v64i0.15598.

S. diNatale. Freezing of micrometer-sized water droplets on well-defined surfaces. Master's thesis, University of Heidelberg, 2012.

D. Duft and T. Leisner. Laboratory evidence for volume-dominated nucleation of ice in supercooled water microdroplets. *Atmospheric Chemistry and Physics*, 4(7):1997–2000, 2004. doi: 10.5194/acp-4-1997-2004.

A. J. Durant, R. A. Shaw, W. I. Rose, Y. Mi, and G. G. J. Ernst. Ice nucleation and overseeding of ice in volcanic clouds. *Journal of Geophysical Research: Atmospheres*, 113:D09206, 2008. doi: 10.1029/2007JD009064.

A. J. Durant, C. Bonadonna, and C. J. Horwell. Atmospheric and Environmental Impacts of Volcanic Particulates. *Elements*, 6(4):235–240, 2010. doi: 10.2113/gselements.6.4.235.

M. L. Eastwood, S. Cremel, M. Wheeler, B. J. Murray, E. Girard, and A. K. Bertram. Effects of sulfuric acid and ammonium sulfate coatings on the ice nucleation properties of kaolinite particles. *Geophys. Res. Lett.*, 36(2):L02811, 2009. doi: 10.1029/2008GL035997.

T. Eidhammer, P. J. DeMott, and S. M. Kreidenweis. A comparison of heterogeneous ice nucleation parameterizations using a parcel model framework. *Journal of Geophysical Research: Atmospheres*, 114(D6):D06202, 2009. doi: 10.1029/2008JD011095.

E.S. Eiríksdottir and H.A. Alfredsson. Leaching experiment on ash from Eyjafjallajökull. source: http://www.earthice.hi.is, 2010.

R. H. Ellerbrock, H. H. Gerke, J. Bachmann, and M.-O. Goebel. Composition of Organic Matter Fractions for Explaining Wettability of Three Forest Soils. *Soil Sci. Soc. Am. J.*, 69(1):57–66, 2005. doi: 10.2136/sssaj2005.0057.

S. Emeis, R. Forkel, W. Junkermann, K. Schäfer, H. Flentje, S. Gilge, W. Fricke, M. Wiegner, V. Freudenthaler, S. Groß, L. Ries, F. Meinhardt, W. Birmili, C. Münkel, F. Obleitner, and P. Suppan. Measurement and simulation of the 16/17 April 2010 Eyjafjallajökull volcanic ash layer dispersion in the northern Alpine region. *Atmospheric Chemistry and Physics*, 11(6):2689–2701, 2011. doi: 10.5194/acp-11-2689-2011.

D. W. Fahey, R. S. Gao, and O. Möhler. Summary of the AquaVIT Water Vapor Intercomparison: Static Experiments. *Source: https://aquavit.icg.kfa-juelich.de/WhitePaper*, 2009.

P. R. Field, O. Möhler, P. Connolly, M. Krämer, R. Cotton, A. J. Heymsfield, H. Saathoff, and M. Schnaiter. Some ice nucleation characteristics of Asian and Saharan desert dust. *Atmospheric Chemistry and Physics*, 6(1):2991–3006, 2006. doi: 10.5194/acp-6-2991-2006.

H. Flentje, H. Claude, T. Elste, S. Gilge, U. Köhler, C. Plass-Dülmer, W. Steinbrecht, W. Thomas, A. Werner, and W. Fricke. The Eyjafjallajökull eruption in April 2010 - detection of volcanic plume using in-situ measurements, ozone sondes and lidar-ceilometer profiles. *Atmospheric Chemistry and Physics*, 10(20):10085–10092, 2010. doi: 10.5194/acp-10-10085-2010.

A. N. Fletcher. Temperature Dependence of the Active Site Concentration of Ice Nucleants. *Journal of the Atmospheric Sciences*, 31(6):1718–1719, 1974. doi: 10.1175/1520-0469(1974)031<1718:TDOTAS>2.0.CO;2.

N. H. Fletcher. Active Sites and Ice Crystal Nucleation. *Journal of the Atmospheric Sciences*, 26(6):1266–1271, 1969. doi: 10.1175/1520-0469(1969)026<1266:ASAICN>2.0.CO;2.

P. Formenti, W. Elbert, W. Maenhaut, J. Haywood, and M. O. Andreae. Chemical composition of mineral dust aerosol during the Saharan Dust Experiment (SHADE)

airborne campaign in the Cape Verde region, September 2000. *Journal of Geophysical Research: Atmospheres*, 108(D18):8576, 2003. doi: 10.1029/2002JD002648.

A. P. Fornea, S. D. Brooks, J. B. Dooley, and A. Saha. Heterogeneous freezing of ice on atmospheric aerosols containing ash, soot, and soil. *Journal of Geophysical Research: Atmospheres*, 114:D13201, 2009. doi: 10.1029/2009JD011958.

P. Forster, V. Ramaswamy, P. Artaxo, T. Berntsen, R. Betts, D. W. Fahey, J. Haywood, J. Lean, D. C. Lowe, G. Myhre, J. Nganga, R. Prinn, G. Raga, M. Schulz, and R. Van Dorland. *Changes in Atmospheric Constituents and in Radiative Forcing. In: Climate Change 2007: The Physical Science Basis. Contribution of Working Group I to the Fourth Assessment Report of the Intergovernmental Panel on Climate Change*. Cambridge University Press, Cambridge, United Kingdom and New York, NY, USA, 2007.

R. Funk and H. I. Reuter. *Wind Erosion*, pages 563–582. John Wiley & Sons,, 2006. ISBN 9780470859209. doi: 10.1002/0470859202.ch41.

E. Garcia, T. C. J. Hill, A. J. Prenni, P. J. DeMott, G. D. Franc, and S. M. Kreidenweis. Biogenic ice nuclei in boundary layer air over two U.S. High Plains agricultural regions. *Journal of Geophysical Research: Atmospheres*, 117(D18):D18209, 2012. doi: 10.1029/2012JD018343.

A. Gendron-Badou, T. Coradin, J. Maquet, F. Fröhlich, and J. Livage. Spectroscopic characterization of biogenic silica. *Journal of Non-Crystalline Solids*, 316(2-3):331–337, 2003. doi: 10.1016/S0022-3093(02)01634-4.

P. Ginoux, J. M. Prospero, T. E. Gill, N. C. Hsu, and M. Zhao. Global-scale attribution of anthropogenic and natural dust sources and their emission rates based on MODIS Deep Blue aerosol products. *Reviews of Geophysics*, 50(3):RG3005, 2012. doi: 10.1029/2012RG000388.

E. Girard, G. Dueymes, P. Du, and A. K. Bertram. Assessment of the effects of acid-coated ice nuclei on the Arctic cloud microstructure, atmospheric dehydration, ra-

diation and temperature during winter. *International Journal of Climatology*, 33(3): 599–614, 2013. doi: 10.1002/joc.3454.

S. R. Gislason, T. Hassenkam, S. Nedel, N. Bovet, E. S. Eiriksdottir, H. A. Alfredsson, C. P. Hem, Z. I. Balogh, K. Dideriksen, N. Oskarsson, B. Sigfusson, G. Larsen, and S. L. S. Stipp. Characterization of Eyjafjallajökull volcanic ash particles and a protocol for rapid risk assessment. *Proceedings of the National Academy of Sciences*, 108(18): 7307–7312, 2011. doi: 10.1073/pnas.1015053108.

L. Gomes and D. A. Gillette. A comparison of characteristics of aerosol from dust storms in Central Asia with soil-derived dust from other regions. *Atmospheric Environment. Part A. General Topics*, 27(16):2539–2544, 1993. doi: 10.1016/0960-1686(93)90027-V.

J. A. González-Pérez, F. J. González-Vila, G. Almendros, and H. Knicker. The effect of fire on soil organic matter - a review. *Environment International*, 30(6):855–870, 2004. doi: 10.1016/j.envint.2004.02.003.

A. Grini, G. Myhre, J. K. Sundet, and I. S. A. Isaksen. Modeling the Annual Cycle of Sea Salt in the Global 3D Model Oslo CTM2: Concentrations, Fluxes, and Radiative Impact. *Journal of Climate*, 15(13):1717–1730, 2002. doi: 10.1175/1520-0442(2002)015<1717:MTACOS>2.0.CO;2.

M. T. Gudmundsson, R. Pedersen, K. Vogfjörd, B. Thorbjarnardóttir, S. Jakobsdóttir, and M. J. Roberts. Eruptions of Eyjafjallajökull Volcano, Iceland. *Eos Trans. AGU*, 91(21):190–191, 2010. doi: 10.1029/2010EO210002.

M. Haarig. Cold-Stage-Experimente zur heterogenen Eisnukleation im Immersionsmodus. Master's thesis, Karlsruhe Institute of Technology, 2013.

A. G. Hallar, G. Chirokova, I. McCubbin, T. H. Painter, C. Wiedinmyer, and C. Dodson. Atmospheric bioaerosols transported via dust storms in the western United States. *Geophysical Research Letters*, 38(17):L17801, 2011. doi: 10.1029/2011GL048166.

M. A. Harper and R. M. McKay. *The diatoms: applications for the environmental and earth sciences - Diatoms as markers of atmospheric transport*. Cambridge University Press, 2. ed. edition, 2010. ISBN 978-0-521-50996-1.

N. Hiranuma, N. Hoffmann, A. Kiselev, A. Dreyer, K. Zhang, G. Kulkarni, T. Koop, and O. Möhler. Influence of surface morphology on the immersion mode ice nucleation efficiency of hematite particles. *Atmospheric Chemistry and Physics Discussions*, 13 (9):23757–23780, 2013. doi: 10.5194/acpd-13-23757-2013.

P. V. Hobbs, C. M. Fullerton, and G. C. Bluhm. Ice Nucleus Storms in Hawaii. *Nature*, 230:90–91, 1971. doi: 10.1038/physci230090a0.

C. Hoose and O. Möhler. Heterogeneous ice nucleation on atmospheric aerosols: a review of results from laboratory experiments. *Atmospheric Chemistry and Physics*, 12(20): 9817–9854, 2012. doi: 10.5194/acp-12-9817-2012.

C. Hoose, J. E. Kristjánsson, J.-P. Chen, and A. Hazra. A Classical-Theory-Based Parameterization of Heterogeneous Ice Nucleation by Mineral Dust, Soot, and Biological Particles in a Global Climate Model. *Journal of the Atmospheric Sciences*, 67(8): 2483–2503, 2010. doi: 10.1175/2010JAS3425.1.

C. R. Hoyle, V. Pinti, A. Welti, B. Zobrist, C. Marcolli, B. Luo, Á. Höskuldsson, H. B. Mattsson, O. Stetzer, T. Thorsteinsson, G. Larsen, and T. Peter. Ice nucleation properties of volcanic ash from Eyjafjallajökull. *Atmospheric Chemistry and Physics*, 11(18):9911–9926, 2011. doi: 10.5194/acp-11-9911-2011.

N. Huneeus, M. Schulz, Y. Balkanski, J. Griesfeller, J. Prospero, S. Kinne, S. Bauer, O. Boucher, M. Chin, F. Dentener, T. Diehl, R. Easter, D. Fillmore, S. Ghan, P. Ginoux, A. Grini, L. Horowitz, D. Koch, M. C. Krol, W. Landing, X. Liu, N. Mahowald, R. Miller, J.-J. Morcrette, G. Myhre, J. Penner, J. Perlwitz, P. Stier, T. Takemura, and C. S. Zender. Global dust model intercomparison in AeroCom phase I. *Atmospheric Chemistry and Physics*, 11(15):7781–7816, 2011. doi: 10.5194/acp-11-7781-2011.

N. Huneeus, O. Boucher, and F. Chevallier. Atmospheric inversion of SO_2 and primary aerosol emissions for the year 2010. *Atmospheric Chemistry and Physics*, 13(13): 6555–6573, 2013. doi: 10.5194/acp-13-6555-2013.

K. Isono and Y. Ikebe. On the ice-nucleating ability of rock-forming minerals and soil particles. *Journ. Met. Soc. Japan*, 38(5):213–230, 1960.

K. Isono, M. Komabayasi, and A. Ono. The Nature and the Origin of Ice Nuclei in the Atmosphere. *Journal of the Meteorological Society of Japan. Ser. II*, 37:211–233, 1959a.

K. Isono, M. Komobayasi, and A. Ono. Volcanoes as a Source of Atmospheric Ice Nuclei. *Nature*, 183(4657):317 – 318, 1959b. doi: 10.1038/183317a0.

M. Kanakidou, J. H. Seinfeld, S. N. Pandis, I. Barnes, F. J. Dentener, M. C. Facchini, R. Van Dingenen, B. Ervens, A. Nenes, C. J. Nielsen, E. Swietlicki, J. P. Putaud, Y. Balkanski, S. Fuzzi, J. Horth, G. K. Moortgat, R. Winterhalter, C. E. L. Myhre, K. Tsigaridis, E. Vignati, E. G. Stephanou, and J. Wilson. Organic aerosol and global climate modelling: a review. *Atmospheric Chemistry and Physics*, 5(4):1053–1123, 2005. doi: 10.5194/acp-5-1053-2005.

K. Kandler, N. Benker, U. Bundke, E. Cuevas, M. Ebert, P. Knippertz, S. Rodríguez, L. Schütz, and S. Weinbruch. Chemical composition and complex refractive index of Saharan Mineral Dust at Izaña, Tenerife (Spain) derived by electron microscopy. *Atmospheric Environment*, 41(37):8058–8074, 2007. doi: 10.1016/j.atmosenv.2007.06.047.

C. A. Kellogg and D. W. Griffin. Aerobiology and the global transport of desert dust. *Trends in Ecology & Evolution*, 21(11):638–644, 2006. doi: 10.1016/j.tree.2006.07.004.

H. Klein, S. Nickovic, W. Haunold, U. Bundke, B. Nillius, M. Ebert, S. Weinbruch, L. Schuetz, Z. Levin, L. A. Barrie, and H. Bingemer. Saharan dust and ice nuclei over Central Europe. *Atmospheric Chemistry and Physics*, 10(21):10211–10221, 2010. doi: 10.5194/acp-10-10211-2010.

D. A. Knopf and T. Koop. Heterogeneous nucleation of ice on surrogates of mineral dust. *Journal of Geophysical Research: Atmospheres*, 111(D12):D12201, 2006. doi: 10.1029/2005JD006894.

D. A. Knopf, P. A. Alpert, B. Wang, and J. Y. Aller. Stimulation of ice nucleation by marine diatoms. *Nature Geoscience*, 4:88–90, 2011. doi: 10.1038/ngeo1037.

K. A. Koehler, S. M. Kreidenweis, P. J. DeMott, M. D. Petters, A. J. Prenni, and O. Möhler. Laboratory investigations of the impact of mineral dust aerosol on cold cloud formation. *Atmospheric Chemistry and Physics*, 10(23):11955–11968, 2010. doi: 10.5194/acp-10-11955-2010.

B. Kärcher and U. Lohmann. A parameterization of cirrus cloud formation: Heterogeneous freezing. *Journal of Geophysical Research: Atmospheres*, 108(D14):4402, 2003. doi: 10.1029/2002JD003220.

B. J. Krueger, V. H. Grassian, J. P. Cowin, and A. Laskin. Heterogeneous chemistry of individual mineral dust particles from different dust source regions: the importance of particle mineralogy. *Atmospheric Environment*, 38(36):6253 – 6261, 2004. doi: 10.1016/j.atmosenv.2004.07.010.

M. Kumai. Snow crystals and the identification of the nuclei in the Northern United States of America. *J. Meteor.*, 18(2):139–150, 1961. doi: 10.1175/1520-0469(1961)018<0139:SCATIO>2.0.CO;2.

C. Linke, O. Möhler, A. Veres, Á. Mohácsi, Z. Bozóki, G. Szabó, and M. Schnaiter. Optical properties and mineralogical composition of different Saharan mineral dust samples: a laboratory study. *Atmospheric Chemistry and Physics*, 6(11):3315–3323, 2006. doi: 10.5194/acp-6-3315-2006.

X. Liu, X. Shi, K. Zhang, E. J. Jensen, A. Gettelman, D. Barahona, A. Nenes, and P. Lawson. Sensitivity studies of dust ice nuclei effect on cirrus clouds with the Community Atmosphere Model CAM5. *Atmospheric Chemistry and Physics*, 12(24):12061–12079, 2012. doi: 10.5194/acp-12-12061-2012.

F. Lüönd, O. Stetzer, A. Welti, and U. Lohmann. Experimental study on the ice nucleation ability of size-selected kaolinite particles in the immersion mode. *Journal of Geophysical Research*, 115:D14201, 2010. doi: 10.1029/2009JD012959.

U. Lohmann and J. Feichter. Global indirect aerosol effects: a review. *Atmospheric Chemistry and Physics*, 5(3):715–737, 2005. doi: 10.5194/acp-5-715-2005.

N. Mahowald, D. S. Ward, S. Kloster, M. G. Flanner, C. L. Heald, N. G. Heavens, P. G. Hess, J.-F. Lamarque, and P. Y. Chuang. Aerosol Impacts on Climate and Biogeochemistry. *Annual Review of Environment and Resources*, 36(1):45–74, 2011. doi: 10.1146/annurev-environ-042009-094507.

C. Marcolli. Deposition nucleation viewed as homogeneous or immersion freezing in pores and cavities. *Atmospheric Chemistry and Physics Discussions*, 13(6):16367–16456, 2013. doi: 10.5194/acpd-13-16367-2013.

C. Marcolli, S. Gedamke, T. Peter, and B. Zobrist. Efficiency of immersion mode ice nucleation on surrogates of mineral dust. *Atmospheric Chemistry and Physics*, 7(19): 5081–5091, 2007. doi: 10.5194/acp-7-5081-2007.

B. J. Mason and J. Maybank. Ice-nucleating properties of some natural mineral dusts. *Quarterly Journal of the Royal Meteorological Society*, 84(361):235–241, 1958. doi: 10.1002/qj.49708436104.

T. A. Mather, D. M. Pyle, and C. Oppenheimer. Tropospheric volcanic aerosol. *Volcanism and the Earth's Atmosphere - Geophysical Monograph*, 139:189 – 212, 2003. doi: 10.1029/139GM12.

M. P. Meyers, P. J. DeMott, and W. R. Cotton. New Primary Ice-Nucleation Parameterizations in an Explicit Cloud Model. *Journal of Applied Meteorology*, 31(7):708–721, 1992. doi: 10.1175/1520-0450(1992)031<0708:NPINPI>2.0.CO;2.

O. Möhler, P. R. Field, P. Connolly, S. Benz, H. Saathoff, M. Schnaiter, R. Wagner, R. Cotton, M. Krämer, A. Mangold, and A. J. Heymsfield. Efficiency of the deposition mode ice nucleation on mineral dust particles. *Atmospheric Chemistry and Physics*, 6 (10):3007–3021, 2006. doi: 10.5194/acp-6-3007-2006.

O. Möhler, S. Benz, H. Saathoff, M. Schnaiter, R. Wagner, J. Schneider, S. Walter, V. Ebert, and S. Wagner. The effect of organic coating on the heterogeneous ice nucleation efficiency of mineral dust aerosols. *Environmental Research Letters*, 3(2): 025007, 2008a. doi: 10.1088/1748-9326/3/2/025007.

O. Möhler, D. G. Georgakopoulos, C. E. Morris, S. Benz, V. Ebert, S. Hunsmann, H. Saathoff, M. Schnaiter, and R. Wagner. Heterogeneous ice nucleation activity of bacteria: new laboratory experiments at simulated cloud conditions. *Biogeosciences*, 5 (5):1425–1435, 2008b. doi: 10.5194/bg-5-1425-2008.

R. T. Morrison and R. N. Boyd. *Lehrbuch der organischen Chemie*. Verlag Chemie, Weinheim, 3. edition, 1986. ISBN 3-527-26067-6.

S. C. Mossop. Some Factors Governing Ice Particle Multiplication in Cumulus Clouds. *Journal of the Atmospheric Sciences*, 35(10):2033–2037, 1978. doi: 10.1175/1520-0469(1978)035<2033:SFGIPM>2.0.CO;2.

D. M. Murphy and T. Koop. Review of the vapour pressures of ice and supercooled water for atmospheric applications. *Quarterly Journal of the Royal Meteorological Society*, 131(608):1539–1565, 2005. doi: 10.1256/qj.04.94.

D. M. Murphy and D. S. Thomson. Chemical composition of single aerosol particles at Idaho Hill: Negative ion measurements. *Journal of Geophysical Research: Atmospheres*, 102(D5):6353–6368, 1997. doi: 10.1029/96JD00859.

B. J. Murray, S. L. Broadley, T. W. Wilson, J. D. Atkinson, and R. H. Wills. Heterogeneous freezing of water droplets containing kaolinite particles. *Atmospheric Chemistry and Physics*, 11(9):4191–4207, 2011. doi: 10.5194/acp-11-4191-2011.

B. J. Murray, D. O'Sullivan, J. D. Atkinson, and M. E. Webb. Ice nucleation by particles immersed in supercooled cloud droplets. *Chem. Soc. Rev.*, 41(19):6519–6554, 2012. doi: 10.1039/C2CS35200A.

K.-H. Naumann. COSIMA - a computer program simulating the dynamics of fractal aerosols. *Journal of Aerosol Science*, 34(10):1371–1397, 2003. doi: 10.1016/S0021-8502(03)00367-7.

D. Niedermeier, S. Hartmann, R. A. Shaw, D. Covert, T. F. Mentel, J. Schneider, L. Poulain, P. Reitz, C. Spindler, T. Clauss, A. Kiselev, E. Hallbauer, H. Wex, K. Mildenberger, and F. Stratmann. Heterogeneous freezing of droplets with immersed

mineral dust particles - measurements and parameterization. *Atmospheric Chemistry and Physics*, 10(8):3601–3614, 2010. doi: 10.5194/acp-10-3601-2010.

D. Niedermeier, S. Hartmann, T. Clauss, H. Wex, A. Kiselev, R. C. Sullivan, P. J. DeMott, M. D. Petters, P. Reitz, J. Schneider, E. Mikhailov, B. Sierau, O. Stetzer, B. Reimann, U. Bundke, R. A. Shaw, A. Buchholz, T. F. Mentel, and F. Stratmann. Experimental study of the role of physicochemical surface processing on the IN ability of mineral dust particles. *Atmospheric Chemistry and Physics*, 11(21):11131–11144, 2011a. doi: 10.5194/acp-11-11131-2011.

D. Niedermeier, R. A. Shaw, S. Hartmann, H. Wex, T. Clauss, J. Voigtländer, and F. Stratmann. Heterogeneous ice nucleation: exploring the transition from stochastic to singular freezing behavior. *Atmospheric Chemistry and Physics*, 11(16):8767–8775, 2011b. doi: 10.5194/acp-11-8767-2011.

M. Niemand. *A Particle-Surface-Area-Based Formulation of Heterogeneous Ice Nucleation by Mineral Dust Aerosols*. PhD thesis, Karlsruhe Institute of Technology, 2012.

M. Niemand, O. Möhler, B. Vogel, H. Vogel, C. Hoose, P. Connolly, H. Klein, H. Bingemer, P. DeMott, J. Skrotzki, and T. Leisner. A Particle-Surface-Area-Based Parameterization of Immersion Freezing on Desert Dust Particles. *Journal of the Atmospheric Sciences*, 69(10):3077–3092, 2012. doi: 10.1175/JAS-D-11-0249.1.

D. R. Nutt and A. J. Stone. Ice Nucleation on a Model Hexagonal Surface. *Langmuir*, 20(20):8715–8720, 2004. doi: 10.1021/la048958l.

J. R. Odum, T. Hoffmann, F. Bowman, D. Collins, R. C. Flagan, and J. H. Seinfeld. Gas/Particle Partitioning and Secondary Organic Aerosol Yields. *Environmental Science & Technology*, 30(8):2580–2585, 1996. doi: 10.1021/es950943+.

D. O'Sullivan, B. J. Murray, T. L. Malkin, T. Whale, N. S. Umo, J. D. Atkinson, H. C. Price, K. J. Baustian, J. Browse, and M. E. Webb. Ice nucleation by soil dusts: relative importance of mineral dust and biogenic components. *Atmospheric Chemistry and Physics Discussions*, 13(8):20275–20317, 2013. doi: 10.5194/acpd-13-20275-2013.

A. Perfumo and R. Marchant. Global transport of thermophilic bacteria in atmospheric dust. *Environmental Microbiology Reports*, 2(2):333–339, 2010. doi: 10.1111/j.1758-2229.2010.00143.x.

V. T. J. Phillips, P. J. DeMott, and C. Andronache. An Empirical Parameterization of Heterogeneous Ice Nucleation for Multiple Chemical Species of Aerosol. *Journal of the Atmospheric Sciences*, 65:2757–2783, 2008. doi: 10.1175/2007JAS2546.1.

V. T. J. Phillips, P. J. DeMott, C. Andronache, K. A. Pratt, K. A. Prather, R. Subramanian, and C. Twohy. Improvements to an Empirical Parameterization of Heterogeneous Ice Nucleation and Its Comparison with Observations. *Journal of the Atmospheric Sciences*, 70(2):378–409, 2012. doi: 10.1175/JAS-D-12-080.1.

V. Pinti, C. Marcolli, B. Zobrist, C. R. Hoyle, and T. Peter. Ice nucleation efficiency of clay minerals in the immersion mode. *Atmospheric Chemistry and Physics*, 12(13): 5859–5878, 2012. doi: 10.5194/acp-12-5859-2012.

K. A. Pratt, P. J. DeMott, J. R. French, Z. Wang, D. L. Westphal, A. J. Heymsfield, C. H. Twohy, A. J. Prenni, and K. A. Prather. In situ detection of biological particles in cloud ice-crystals. *Nature Geoscience*, 2:398–401, 2009. doi: 10.1038/ngeo521.

H. R. Pruppacher and J. D. Klett. *Microphysics of Clouds and Precipitation*. Atmospheric and Oceanographic Sciences Library (18). Kluwer, 2. rev. and enl. edition, 1997. ISBN 0-7923-4211-9.

H. R. Pruppacher and R. Sänger. Mechanismus der Vereisung unterkühlter Wassertropfen durch disperse Keimsubstanzen. *Z. Angew. Math. Phys.*, 6(6):407–416, 1955. doi: 10.1007/BF01600534.

U. Pöschl. Atmospheric aerosols: Composition, transformation, climate and health effects. *Angewandte Chemie International Edition*, 44(46):7520–7540, 2005. doi: 10.1002/anie.200501122.

G. B. Raga, G. L. Kok, D. Baumgardner, A. Báez, and I. Rosas. Evidence for volcanic influence on Mexico City aerosols. *Geophys. Res. Lett.*, 26(8):1149–1152, 1999. doi: 10.1029/1999GL900154.

P. Roberts and J. Hallett. A laboratory study of the ice nucleating properties of some mineral particulates. *Quarterly Journal of the Royal Meteorological Society*, 95(403): 204–205, 1969. doi: 10.1002/qj.49709540317.

D. C. Rogers. *Field and Laboratory Studies of Ice Nucleation in Winter Orographic Clouds*. PhD thesis, University of Wyoming, 1982.

W. I. Rose and A. J. Durant. Fine ash content of explosive eruptions. *Journal of Volcanology and Geothermal Research*, 186(1-2):32 – 39, 2009. doi: 10.1016/j.jvolgeores.2009.01.010.

H. Saathoff, K.-H. Naumann, O. Möhler, Å. M. Jonsson, M. Hallquist, A. Kiendler-Scharr, T. F. Mentel, R. Tillmann, and U. Schurath. Temperature dependence of yields of secondary organic aerosols from the ozonolysis of α-pinene and limonene. *Atmospheric Chemistry and Physics*, 9(5):1551–1577, 2009. doi: 10.5194/acp-9-1551-2009.

H. Saathoff, S. Henin, K. Stelmaszczyk, M. Petrarca, R. Delagrange, Z. Hao, J. Lüder, O. Möhler, Y. Petit, P. Rohwetter, M. Schnaiter, J. Kasparian, T. Leisner, J.-P. Wolf, and L. Wöste. Laser filament-induced aerosol formation. *Atmospheric Chemistry and Physics*, 13(9):4593–4604, 2013. doi: 10.5194/acp-13-4593-2013.

K. Sassen and S. Benson. Ice nucleation in cirrus clouds: A model study of the homogeneous and heterogeneous modes. *Geophysical Research Letters*, 27(4):521–524, 2000. doi: 10.1029/1999GL010883.

K. Sassen and Z. Wang. The Clouds of the Middle Troposphere: Composition, Radiative Impact, and Global Distribution. *Surveys in Geophysics*, 33(3-4):677–691, 2012. doi: 10.1007/s10712-011-9163-x.

K. Sassen, P. J. DeMott, J. M. Prospero, and M. R. Poellot. Saharan dust storms and indirect aerosol effects on clouds: CRYSTAL-FACE results. *Geophysical Research Letters*, 30(12):1633, 2003. doi: 10.1029/2003GL017371.

V. J. Schaefer. The formation of ice crystals in the laboratory and the atmosphere. *Chemical Reviews*, 44(2):291–320, 1949. doi: 10.1021/cr60138a004.

R. C. Schnell and A.C. Delany. Airborne ice nuclei near an active volcano. *Nature*, 264: 535–536, 1976. doi: 10.1038/264535a0.

U. Schumann, B. Weinzierl, O. Reitebuch, H. Schlager, A. Minikin, C. Forster, R. Baumann, T. Sailer, K. Graf, H. Mannstein, C. Voigt, S. Rahm, R. Simmet, M. Scheibe, M. Lichtenstern, P. Stock, H. Rüba, D. Schäuble, A. Tafferner, M. Rautenhaus, T. Gerz, H. Ziereis, M. Krautstrunk, C. Mallaun, J.-F. Gayet, K. Lieke, K. Kandler, M. Ebert, S. Weinbruch, A. Stohl, J. Gasteiger, S. Groß, V. Freudenthaler, M. Wiegner, A. Ansmann, M. Tesche, H. Olafsson, and K. Sturm. Airborne observations of the Eyjafjalla volcano ash cloud over Europe during air space closure in April and May 2010. *Atmospheric Chemistry and Physics*, 11(5):2245–2279, 2011. doi: 10.5194/acp-11-2245-2011.

P. Seifert, A. Ansmann, S. Groß, V. Freudenthaler, B. Heinold, A. Hiebsch, I. Mattis, J. Schmidt, F. Schnell, M. Tesche, U. Wandinger, and M. Wiegner. Ice formation in ash-influenced clouds after the eruption of the Eyjafjallajökull volcano in April 2010. *Journal of Geophysical Research: Atmospheres*, 116:D00U04, 2011. doi: 10.1029/2011JD015702.

J. H. Seinfeld and S. N. Pandis. *Atmospheric chemistry and physics: from air pollution to climate change*. Wiley, 2. ed. edition, 2006. ISBN 0-471-72018-6.

L. Smoydzin, A. Teller, H. Tost, M. Fnais, and J. Lelieveld. Impact of mineral dust on cloud formation in a Saharan outflow region. *Atmospheric Chemistry and Physics*, 12 (23):11383–11393, 2012. doi: 10.5194/acp-12-11383-2012.

B. J. Soden, R. T. Wetherald, G. L. Stenchikov, and A. Robock. Global Cooling After the Eruption of Mount Pinatubo: A Test of Climate Feedback by Water Vapor. *Science*, 296(5568):727–730, 2002. doi: 10.1126/science.296.5568.727.

P. Spichtinger and D. J. Cziczo. Impact of heterogeneous ice nuclei on homogeneous freezing events in cirrus clouds. *Journal of Geophysical Research: Atmospheres*, 115 (D14):D14208, 2010. doi: 10.1029/2009JD012168.

P. Spichtinger and K. M. Gierens. Modelling of cirrus clouds - Part 2: Competition of different nucleation mechanisms. *Atmospheric Chemistry and Physics*, 9(7):2319–2334, 2009. doi: 10.5194/acp-9-2319-2009.

I. Steinke, O. Möhler, A. Kiselev, M. Niemand, H. Saathoff, M. Schnaiter, J. Skrotzki, C. Hoose, and T. Leisner. Ice nucleation properties of fine ash particles from the Eyjafjallajökull eruption in April 2010. *Atmospheric Chemistry and Physics*, 11(24): 12945–12958, 2011. doi: 10.5194/acp-11-12945-2011.

A. Stohl, A. J. Prata, S. Eckhardt, L. Clarisse, A. Durant, S. Henne, N. I. Kristiansen, A. Minikin, U. Schumann, P. Seibert, K. Stebel, H. E. Thomas, T. Thorsteinsson, K. Tørseth, and B. Weinzierl. Determination of time- and height-resolved volcanic ash emissions and their use for quantitative ash dispersion modeling: the 2010 Eyjafjallajökull eruption. *Atmospheric Chemistry and Physics*, 11(9):4333–4351, 2011. doi: 10.5194/acp-11-4333-2011.

R. C. Sullivan, L. Miñambres, P. J. DeMott, A. J. Prenni, C. M. Carrico, E. J. T. Levin, and S. M. Kreidenweis. Chemical processing does not always impair heterogeneous ice nucleation of mineral dust particles. *Geophys. Res. Lett.*, 37(24):L24805, 2010a. doi: 10.1029/2010GL045540.

R. C. Sullivan, M. D. Petters, P. J. DeMott, S. M. Kreidenweis, H. Wex, D. Niedermeier, S. Hartmann, T. Clauss, F. Stratmann, P. Reitz, J. Schneider, and B. Sierau. Irreversible loss of ice nucleation active sites in mineral dust particles caused by sulphuric acid condensation. *Atmospheric Chemistry and Physics*, 10(23):11471–11487, 2010b. doi: 10.5194/acp-10-11471-2010.

I. Tegen and K. Schepanski. The global distribution of mineral dust. *IOP Conference Series: Earth and Environmental Science*, 7(1):012001, 2009. doi: 10.1088/1755-1307/7/1/012001.

I. Tegen, M. Werner, S. P. Harrison, and K. E. Kohfeld. Relative importance of climate and land use in determining present and future global soil dust emission. *Geophysical Research Letters*, 31(5):L05105, 2004. doi: 10.1029/2003GL019216.

M. C. Todd, R. Washington, J.V. Martins, O. Dubovik, G. Lizcano, S. M'Bainayel, and S. Engelstaedter. Mineral dust emission from the Bodélé depression, northern Chad, during BoDEx 2005. *Journal of Geophysical Research: Atmospheres*, 112(D6): D06207, 2007. doi: 10.1029/2006JD007170.

I. Toepfer, J. Favet, A. Schulte, M. Schmölling, W. Butte, E. W. Triplett, W. J. Broughton, and A. A. Gorbushina. Pathogens as potential hitchhikers on intercontinental dust. *Aerobiologia*, 28(2):221–231, 2012. doi: 10.1007/s10453-011-9230-2.

D. O. Topping, G. B. McFiggans, and H. Coe. A curved multi-component aerosol hygroscopicity model framework: Part 1 - Inorganic compounds. *Atmospheric Chemistry and Physics*, 5(5):1205–1222, 2005. doi: 10.5194/acp-5-1205-2005.

K. Tsigaridis, D. Koch, and S. Menon. Uncertainties and importance of sea spray composition on aerosol direct and indirect effects. *Journal of Geophysical Research: Atmospheres*, 118(1):220–235, 2013. doi: 10.1029/2012JD018165.

G. Vali. Quantitative Evaluation of Experimental Results on the Heterogeneous Freezing Nucleation of Supercooled Liquids. *Journal of the Atmospheric Sciences*, 28(3):402–409, 1971. doi: 10.1175/1520-0469(1971)028<0402:QEOERA>2.0.CO;2.

G. Vali. Nucleation terminology. *Bull. Am. Meteorol. Soc.*, 66:1426–1427, 1985.

G. Vali. Repeatability and randomness in heterogeneous freezing nucleation. *Atmospheric Chemistry and Physics*, 8(16):5017–5031, 2008. doi: 10.5194/acp-8-5017-2008.

G. Vali and E. J. Stansbury. Time-dependent characteristics of the heterogeneous nucleation of ice. *Canadian Journal of Physics*, 44(3):477–502, 1965. doi: 10.1139/p66-044.

A. Vlasenko, S. Sjögren, E. Weingartner, H. W. Gäggeler, and M. Ammann. Generation of Submicron Arizona Test Dust Aerosol: Chemical and Hygroscopic Properties. *Aerosol Science and Technology*, 39(5):452–460, 2005. doi: 10.1080/027868290959870.

R. Wagner, C. Linke, K.-H. Naumann, M. Schnaiter, M. Vragel, M. Gangl, and H. Horvath. A review of optical measurements at the aerosol and cloud chamber AIDA. *Jour-*

nal of Quantitative Spectroscopy and Radiative Transfer, 110(11):930 – 949, 2009. doi: 10.1016/j.jqsrt.2009.01.026.

A. Warren, A. Chappell, M. C. Todd, C. Bristow, N. Drake, S. Engelstaedter, V. Martins, S. M'Bainayel, and R. Washington. Dust-raising in the dustiest place on earth. *Geomorphology*, 92(1-2):25 – 37, 2007. doi: 10.1016/j.geomorph.2007.02.007.

A. Welti, F. Lüönd, O. Stetzer, and U. Lohmann. Influence of particle size on the ice nucleating ability of mineral dusts. *Atmospheric Chemistry and Physics*, 9(18):6705–6715, 2009. doi: 10.5194/acp-9-6705-2009.

A. Welti, F. Lüönd, Z. A. Kanji, O. Stetzer, and U. Lohmann. Time dependence of immersion freezing: an experimental study on size selected kaolinite particles. *Atmospheric Chemistry and Physics*, 12(20):9893–9907, 2012. doi: 10.5194/acp-12-9893-2012.

C. D. Westbrook. The fall speeds of sub-100 µm ice crystals. *Quarterly Journal of the Royal Meteorological Society*, 134(634):1243–1251, 2008. doi: 10.1002/qj.290.

M. J. Wheeler and A. K. Bertram. Deposition nucleation on mineral dust particles: a case against classical nucleation theory with the assumption of a single contact angle. *Atmospheric Chemistry and Physics*, 12(2):1189–1201, 2012. doi: 10.5194/acp-12-1189-2012.

T. P. Wright, M. D. Petters, J. D. Hader, T. Morton, and A. L. Holde. Minimal cooling-rate dependence of ice nuclei activity in the immersion mode. *Journal of Geophysical Research*, 2013 (submitted).

Z. Yang, A. K. Bertram, and K. C. Chou. Why Do Sulfuric Acid Coatings Influence the Ice Nucleation Properties of Mineral Dust Particles in the Atmosphere? *The Journal of Physical Chemistry Letters*, 2(11):1232–1236, 2011. doi: 10.1021/jz2003342.

Y. Yun and J. E. Penner. Global model comparison of heterogeneous ice nucleation parameterizations in mixed phase clouds. *Journal of Geophysical Research: Atmospheres*, 117(D7):D07203, 2012. doi: 10.1029/2011JD016506.

D. Zhang, Z. Wang, A. Heymsfield, J. Fan, D. Liu, and M. Zhao. Quantifying the impact of dust on heterogeneous ice generation in midlevel supercooled stratiform clouds. *Geophysical Research Letters*, 39:L18805, 2012. doi: 10.1029/2012GL052831.

Danksagung

An dieser Stelle möchte ich ein großes Dankeschön an alle richten, die mich während meiner Doktorarbeit unterstützt und begleitet haben.

Als erstes möchte ich mich bei Prof. Dr. Thomas Leisner dafür bedanken, dass er mir die Gelegenheit gegeben hat, meine Doktorarbeit am Institut für Meteorologie und Klimaforschung in Karlsruhe durchzuführen. Während dieser Zeit hatte ich die Möglichkeit, viel zu lernen und auch eigene Ideen umzusetzen. Für die Unterstützung an dieser Stelle ein Dankeschön, und auch für die Begutachtung und Bewertung meiner Doktorarbeit. Vielen Dank auch an Prof. Ulrich Platt, der sich bereit erklärt hat, als Zweitgutachter zu fungieren.

Meine Zeit während der Doktorarbeit wäre bestimmt auch nicht so spannend und lehrreich gewesen ohne meine Betreuerin Prof. Dr. Corinna Hoose, die mir stets dabei geholfen hat, meine Projekte im Laufe der Zeit weiter zu entwickeln. An dieser Stelle auch ein großes Dankeschön für die Unterstützung und die Bereitschaft Ideen offen zu diskutieren, kritisch zu hinterfragen und damit immer wieder neue Anstöße zu geben. Danke auch für das Korrekturlesen der Paperentwürfe und meiner Doktorarbeit.

Ein großer Teil dieser Doktorarbeit ist aus Experimenten an der AIDA-Wolkenkammer entstanden, bei denen ich sehr viel von Dr. Ottmar Möhler lernen konnte, der mich besonders am Anfang meiner Doktorarbeit intensiv unterstützt hat. Ein großes Dankeschön für die Einführung in das Experimentieren mit der AIDA-Wolkenkammer und die Unterstützung bei der Planung von Experimenten sowie das Korrekturlesen meiner Paperentwürfe und der Doktorarbeit.

An den AIDA-Experimenten waren außerdem noch Dr. Martin Schnaiter, Dr. Harald Saathoff, Dr. Kristina Höhler und Dr. Naruki Hiranuma beteiligt, die mich mit der Messinstrumentierung an der AIDA vertraut gemacht oder mich bei den Messkampagnen unterstützt haben. Vielen Dank für die produktive Zeit, das bereitwillige Beantworten von Fragen und immer wieder neue Ideen. Bei den Experimenten an der AIDA konnte ich mich außerdem immer auf die technische Mannschaft verlassen (manchmal auch noch

spätabends). Für diesen Einsatz und die große Hilfsbereitschaft geht ein Dankeschön an Georg Scheurig, Tomasz Chudy, Olga Dombrowski, Rainer Buschbacher, Elisabeth Kranz, Steffen Vogt und Meinrad Koyro. Vielen Dank auch an Susanne Bolz für die Hilfe bei organisatorischen Angelegenheiten.

Auch beim Aufbau des Cold Stage-Experimentes haben mich mehrere Menschen tatkräftig unterstützt und das Projekt damit möglich gemacht. Am Aufbau waren Thibault Hieron, Sandro DiNatale und Moritz Haarig maßgeblich beteiligt. Vielen Dank dafür, dass sich das Experiment über die letzten Monate so gut entwickelt und auch die ersten Daten produziert hat. Die ersten Schritte mit dem Cold Stage-Experiment wären ohne die Unterstützung und das technische Wissen der Paulfallengruppe wesentlich schwieriger gewesen - für die kleinen und großen Hilfestellungen beim Umgang mit der "Spritze" und der Labview-Programmierung geht insbesondere ein Dankeschön an Dr. Denis Duft und Thomas Pander. Vielen Dank auch an Dr. Alexei Kiselev und Nadine Hoffmann für die ESEM-Bilder und fruchtbare Diskussionen.

Vielen Dank auch an die anderen Kollegen des Instituts, die für eine gute Atmosphäre gesorgt haben und von denen ich während meiner Doktorarbeit viel lernen konnte. Danke auch an Matthias Hummel, Marco Paukert und Romy Ulrich für die gemeinsame Zeit im "Container" und interessante (und produktive) Diskussionen.

Vielen Dank auch für die ergiebigen Kooperationen mit Kollegen außerhalb des Institutes, besonders an das Institut für Mikrostrukturtechnologie (KIT, Karlsruhe), das Institut für Funktionelle Grenzflächen (KIT, Karlsruhe) und das Leibniz-Zentrum für Agrarlandschaftsforschung (Müncheberg).

Vielen Dank auch an meine Familie und die Freunde in und außerhalb von Karlsruhe, die mich bei dem Projekt "Doktorarbeit" unterstützt haben und die dafür gesorgt haben, dass diese Zeit etwas Besonderes war.